Stony Brook University

OFFICIAL COPY

The official electronic file of this thesis or dissertation is maintained by the University Libraries on behalf of The Graduate School at Stony Brook University.

© All Rights Reserved by Author.

A Multimodal Approach to Materials Design for Next Generation Energy Storage Systems

A Dissertation Presented

by

Alyson Abraham

to

The Graduate School

in Partial Fulfillment of the

Requirements

for the Degree of

Doctor of Philosophy

in

Chemistry

Stony Brook University

May 2020

Stony Brook University

The Graduate School

Alyson Abraham

We, the dissertation committee for the above candidate for the

Doctor of Philosophy degree, hereby recommend

acceptance of this dissertation.

Dr. Esther S. Takeuchi – Dissertation co-Advisor
Distinguished Professor, Department of Chemistry, Department of Materials Science and Chemical Engineering

Dr. Kenneth J. Takeuchi - Dissertation co-Advisor
Distinguished Teaching Professor, Department of Chemistry

Dr. Amy C. Marschilok - Dissertation co-Advisor
Associate Professor Department of Chemistry, Research Professor Department of Materials Science and Chemical Engineering

Dr. Andreas Mayr - Chairperson of Defense
Professor, Department of Chemistry

Dr. Sanjaya Senanayake– Committee Member
Chemist, Brookhaven National Laboratory

Dr. Lisa Szczepura- Outside Committee Member
Professor, Department of Chemistry, Illinois State University

This dissertation is accepted by the Graduate School

Eric Wertheimer

Dean of the Graduate School

Abstract of the Dissertation

A Multimodal Approach to Materials Design for Next Generation Energy Storage Systems

by

Alyson Abraham

Doctor of Philosophy

in

Chemistry

Stony Brook University

2020

While batteries of various chemistries have been responsible for powering everything from small electronics to cars to medical devices, the need for energy storage continues to increase. This increase is in both volume and in scale, as energy storage systems are increasingly being evaluated for inclusion into both larger and broader applications. An important factor to consider with batteries is the end application, as each chemistry and battery system has specific benefits as well as limitations. This necessitates development of a wide range of battery chemistries as well as substantive improvements to these chemistries and their integration on the material, electrode, and systems level. Herein, this work will present on a multi-scale level, different energy storage studies can that are geared to address the demands and needs of varying applications. To highlight the diversity and uniqueness of the required breadth of approaches, several systems are presented in combination with different characterization techniques and analysis relevant to the system. Highlights include proof of concept and development of a self - forming, rechargeable solid state battery, materials development for Lithium Sulfur (Li-S) batteries, electrochemical and characterization techniques to elucidate materials properties, and utilizing theoretical calculations to compliment experimental observations.

Table of Contents

List of Figures

List of Tables

Acknowledgments

The research included herein represents the culmination of years of work (2015-2020), conducted in part of a wide reaching group effort in leading the future of research in energy storage. I would like to acknowledge first and foremost, the unwavering support and mentorship by my advisors, Dr. Esther S. Takeuchi, Dr. Kenneth J. Takeuchi, and Dr. Amy C. Marschilok, for which this would have not been possible without their support and guidance. Under their advisement, I have been able to execute on a "new model" of graduate student education, where collaboration and simultaneous investigations can be executed. This leads both to an expanded skill set, and increased productivity, and is in line with the working model that is emphasized in addressing pressing, time sensitive problems. I would like to acknowledge the support of my Committee chair, Dr. Andreas Mayr, and committee member Dr. Sanjaya Senenayake for their ongoing support and challenging questions over the time of my PhD. Additionally, I would like to acknowledge the commitment of Dr. Lisa Szczepura from Illinois State University for taking the time to being part of my committee.

This research was conducted in a highly collaborative environment, both within the research group, and as part of a multi-institutional collaborative effort, under the Center for Mesoscale Transport Properties (m2m and m2m/t) Energy Frontier Research Center. I would like to thank Dr. Ping Liu (Brookhaven National Laboratory) and Haoyue Guo for collaboration on the DFT work included herein.

This work consisted of combined efforts from multiple group members, including graduate students, post doctoral researchers and affiliated scientists. I would specifically like to thank Dr. David Bock and Dr. Lei Wang (Brookhaven National Laboratory), for their insights and feedback, and to Lisa Housel, Calvin Quilty, Dr. Chavis Stackhouse, Diana Lutz, and Killian Tallman for their collaborative efforts.

I would like to acknowledge the Department of Energy Offices that have funded the following research, including, DOE Office of Science- Basic Energy Sciences (DOE BES), the Office of Energy Efficiency & Renewable Energy (EERE) Advanced Battery Materials Research

program, and Office of Electricity (OE). Additionally, I am grateful for the support provided (2017-2018) under the Graduate Assistance in Areas of National Need Fellowship (GAANN).

Work included in the full literature reports discussed herein includes a significant amount of data collected from U. S. Department of Energy, Office of Science user facilities, including the Center for Functional Nanomaterials (CFN), and the National Synchrotron Light Source II (NSLS II) both located at Brookhaven National Laboratory. Brookhaven National Laboratory has also supported the research discussed herein utilizing scanning vibrating probe (SVP) and scanning electrochemical microscopy (SECM). I would also like to acknowledge the Advanced Energy and Research Technology Center (AERTC) for access to the ThINC facility.

The text of this dissertation is adapted with permission from materials in the publications listed below. The co-authors listed in the publications below, Dr. Esther S. Takeuchi, Dr. Kenneth J. Takeuchi, Dr. Amy C. Marschilok, directed and supervised the research that forms the basis for this dissertation.

Chapter I

Section 1.3

Copyright © (2019) Cambridge University Press. Stackhouse, C., A., Abraham, A., Takeuchi, K. J., Takeuchi, E. S., Marschilok, A. C., Progress and Outlook on Few Component Composite Solid State Electrolytes, *MRS Advances*, 4(49), 2635-2640. Reproduced with permission.

Section 1.4

Reprinted (adapted) with permission from: Wang, L., Abraham, A., Lutz, D. M., Quilty, C. D., Takeuchi, E. S., Takeuchi, K. J., Marschilok, A. C., Toward Environmentally Friendly Lithium Sulfur Batteries: Probing the role of Electrode Design in MoS_2-Containing Li-S Batteries with a Green Electrolyte, *ACS Sustainable Chemistry & Engineering,* 2019, 7(5) 5209-5222.

Copyright © (2019) American Chemical Society.

Chapter II

Republished with permission of IOP Publishing, Ltd.., from: Communication- Demonstration and Electrochemistry of a Self-Forming, Solid State Rechargeable $LiI(HPN)_2$ Based Li/I_2 Battery, Abraham, A., Huang, J., Smith, P. S., Marschilock, A. C., Takeuchi, K. J., Takeuchi, E. S., *J. Electrochem. Soc.,*165(10), A2115-A2118. Copyright © 2018; permission conveyed through Copyright Clearance Center, Inc.

Copyright (2019) © Cambridge University Press. Abraham, A., Dunkin, M. R., Huang, J., Zhang, B., Takeuchi, K. J., Takeuchi, E. S., Marschilok, A. C., Interface effects on self-forming, rechargeable Li/I_2-based solid state batteries *MRS Communications,*9(2) 657-662. Reproduced with permission.

Chapter III

Copyright (2019) © Wiley. Used with permission from: Abraham, A., Wang, L., Quilty, C. D., Lutz, D. M., McCarthy, A. H., Tang, C. R., Dunkin, M. R., Housel, L. M., Takeuchi, E. S., Marschilok, A. C., Takeuchi, K. J., Defect Control in the Synthesis of 2 D MoS_2 Nanosheets: Polysulfide Trapping in Composite Sulfur Cathodes for Li-S Batteries, *ChemSusChem***,** 12, DOI: 10.1002/cssc.201903028.

The following is adapted from the following open access article distributed under the terms of the Creative Commons Attribution 4.0 License, permitting the unrestricted used of the work in any medium, provided citation:
Electrodeposition of MoS_x: Tunable Fabrication of Sulfur Equivalent Electrodes for High Capacity or High Power, Wu, Q., Abraham, A., Wang, L., Tong, X., Takeuchi, E. S., Takeuchi, K. J., Marschilok, A. C., *J. Electrochem. Soc.,* 2020, 167, 050513.

Chapter IV

The following is adapted from the following ACS AuthorChoice License, which permits copying and redistribution of the article or any adaptations for non-commercial purposes:

Abraham, A., Housel, L. M., Lininger, C. N., Bock, D. C., Jou, J., Wang, F., West, A. C., Marschilok, A. C., Takeuchi, K. J., Takeuchi, E. S., Investigating the Complex Chemistry of Functional Energy Storage Systems: The Need for an Integrative, Multiscale (Molecular to Mesoscale) Perspective, *ACS Cent. Sci*, 2016, 2(6), 380-387. DOI: 10.1021/acscentsci.6b00100 Copyright © 2016 American Chemical Society.

Reprinted (adapted) with permission from:

Deliberate Modification of Fe_3O_4 Anode Surface Chemistry: Impact on Electrochemistry, Wang, L., Housel, L. M., Bock, D. C., Abraham, A., Dunkin, M. R., McCarthy, A. H., Wu, Q., Kiss, A., Thieme, J., Takeuchi, E. S., Marschilok, A. C., Takeuchi, K. J., *ACS Appl. Mater. Interfaces*, 2019, *11*, 19920-19932. Copyright © 2019, American Chemical Society.

Section 4.3

The following is adapted from the following open access article distributed under the terms of the Creative Commons Attribution 4.0 License, permitting the unrestricted used of the work in any medium, provided citation:

© 2019. Wang, L., Wu, Q., Abraham, A., West, P. J., Housel, L. M., Singh, G., Sadique, N., Quilty, C. D., Wu, D., Takeuchi, E. S., Marschilok, A. C., Takeuchi, K. J., Silver Containing α-MnO_2 Nanorods: Electrochemistry in Rechargeable Aqueous Zn-MnO_2 Batteries, *J. Electrochem. Soc.*, 166 (15) A3575-A3584. DOI: 10.1149/2.0101915jes

Section 4.4:

Reprinted (adapted) with permission from:

Investigation of Conductivity and Ionic Transport of VO_2(M) and VO_2(R) via Electrochemical Study, Housel, L., M., Quilty, C. D., Abraham, A., Tang, C. R., McCarthy, A. H., Renderos, G. D., Liu, P., Takeuchi, E. S., Marschilok, A. C., Takeuchi, K. J., *Chem. Mater.,* 2018, 30, 217535-7544. Copyright © 2018, American Chemical Society.

Publications

[1] Electrodeposition of MoS_x: Tunable Fabrication of Sulfur Equivalent Electrodes for High Capacity of High Power, Wu, Q., Abraham, A., Wang, L., Tong, X., Takeuchi, E. S., Takeuchi, K. J., Marschilok, A. C., *J. Electrochem. Soc.,* **2020**, 167, 050513.

[2] Defect control in synthesis of 2D MoS_2 Nanosheets: Favorable Impact on Polysulfide Trapping in composite sulfur cathodes for Lithium-Sulfur Batteries, Abraham, A., Wang, L., Quilty, C. Q., Lutz, D. M., McCarthy, A. H., Marschilok, A. C., Takeuchi, K. J., *Chem. Sus. Chem.,* **2019,** DOI: 10.1002/cssc.201903028.

[3] Silver-containing α-MnO_2 nanorods: Electrochemistry in rechargeable aqueous $ZnMnO_2$ batteries, Wang, L., Wu, Q., **Abraham, A.,** Housel, L. M., West, P., Singh, G., Sadique, N., Takeuchi, K.J., Marschilok, A. C., Takeuchi, E. S., , *J. Electrochem Soc.,* **2019,** 166, 15. A3575-A3584.

[4] Ex Situ and Operando XRD and XAS Analysis of MoS_2: A Lithiation Study of Bulk and Nanosheet Materials, Quilty, C. D., Lisa, L., M., Bock, D. C., Dunkin, M. R., Wang, L., Lutz, D. M., **Abraham, A.,** Bruck, A. M., Takeuchi, E. S., Takeuchi, K. J., Marschilok, A. C., *ACS Appl. Energy Mater.,* **2019**, 2, 7635-7646.

[5] Deliberate modification of surface chemistry Fe_3O_4 anode surface chemistry, Wang, L., Housel, L. M., Bock, D. C., **Abraham, A.,** Dunkin, M. R., McCarthy, A. H., Thieme, J., Takeuchi, E. S., Marschilok, A. C., Takeuchi, K. J., *ACS Appl. Mater. Interfaces,* **2019**, 11, 19920-19932.

[6] Interface effects on self-forming rechargeable Li/I_2-based solid state batteries, **Abraham, A.,** Dunkin, M. R., Huang, J., Zhang, B., Takeuchi, K. J., Takeuchi, E. S., Marschilok, A. C., MRS Communications, **2019**, 9, 657.

[7] High capacity vanadium oxide electrodes: effective recycling through thermal treatment, Huang, J., Housel, L. M., Wang, L., Bruck, A. M., Quilty, C. D., **Abraham, A.,** Lutz, D. M., Tang, C. R., Kiss, A., Thieme, J., Takeuchi, K. J., Takeuchi, E. S., Marschilok, A. C., *Sustain. Energ. Fuels*, **2019**, DOI: 10.1039/c9se00188c.

[8] Toward Environmentally Friendly Lithium Sulfur Batteries: Probing the Role of Electrode Design in MoS_2-Containing Li-S Batteries with a Green Electrolyte, Wang, L., **Abraham, A.,** Lutz, D.M., Quilty, C.D., Takeuchi, E.S., Takeuchi, K.J., Marschilok, A.C., *ACS Sus. Chem. Eng.,* **2019**, 7, 5209-5222.

[9] Progress and outlook on few component composite solid state electrolytes, Stackhouse, C. A., **Abraham, A.,** Takeuchi, K. J., Takeuchi, E. S., *MRS Adv*., **2019**, DOI: 10.1557/adv.2019.264

[10] Communication- Demonstration and Electrochemistry of a Self-Forming, Solid State Rechargeable LiI(HPN)$_2$ Based Li/I$_2$ Battery, **Abraham, A.,** Huang, J., Smith, P. S., Marschilok, A. C., Takeuchi, K. J., Takeuchi, E. S., J. Electrochem. Soc., **2018**, 165(10), A2115.

[11] Investigation of Conductivity and Ionic Transport of VO_2(M) and VO_2(R) via Electrochemical Study, Housel, L.M., Quilty, C.D., **Abraham, A.,** Tang, C.R., McCarthy, A.H., Renderos, G.D., Liu, P., Takeuchi, E.S., Marschilok, A.C., Takeuchi, K.J., *Chem. Mater.,* **2018**, 30, 7535-7544.

[12] Surface electrolyte interphase control on magnetite, Fe_3O_4: Impact on Electrochemistry, Housel, L.H., **Abraham, A**., Renderos, G. D., Takeuchi, K. J., Takeuchi, E. S., Marschilok, A. C., **2018**, *MRS Adv*., DOI: 10.1557/adv.2018.294

[13] Capacity Retention for (De)lithiation of Silver Containing α-MnO_2: Impact of Structural Distortion and Transition Metal Dissolution, Huang, J., Housel, L.M., Quilty, C.D., Brady, A.B., Smith, P.F., **Abraham, A.,** Dunkin, M.R., Lutz, D.M., Zhang, B., Takeuchi, E.S., Marschilok, A.C., Takeuchi, K.J., *J. Electrochem. Soc*, **2018,** 165, 11, A2849-A2858.

[14] Investigation of α-MnO_2 Tunnelled Structures as Model Cation Hosts for Energy Storage, Housel, L. M., Wang, L., **Abraham, A.,** Huang, J., Renderos, G. D., Quilty, C. D., Brady, A. B., Marschilok, A. C., Takeuchi, K. J., Takeuchi, E. S., *Acc. Chem. Res.,* **2018**, 51, 575.

[15] Investigating the Complex Chemistry of Functional Energy Storage Systems: The Need for an Integrative, Multiscale (Molecular to Mesoscale) Perspective, **Abraham, A**., Housel, L. M., Lininger, C. N., Bock, D. C., Jou, J., Wang, F., West, A. C., Marschilok, A. C., Takeuchi, K. J., Takeuchi, E. S., *ACS Cent. Sci,* **2016**, 2, 3

Chapter I

Introduction

1.0 Overview

Electrochemical Energy Storage (EES) has become a highly researched topic within the recent years. While batteries of various chemistries have been responsible for powering everything from small electronics to cars[1] to medical devices,[2, 3] the need for energy storage continues to increase. This increase is in both volume and in scale, as energy storage systems are increasingly being evaluated for inclusion into grid applications.[4] An important factor to consider with batteries is the end application. For example, each chemistry and battery system has specific benefits as well as limitations. This necessitates development of a wide range of battery chemistries as well as substantive improvements to these chemistries and their integration on the material, electrode, and systems level.

With an increase in demand for progressive technologies, demand for electric vehicles and alternative modes of energy generation and energy storage are becoming increasingly popular. An example of this follows a 2020 report that describes a technology and market comparison for plug-in electric vehicles in China and the United States.[5] Since 2014, the United States and China have been the two largest plug-in electric vehicle (PEV) market, as reported by the International Energy Agency.[6] There are two types of PEVs, full battery electric vehicles (BEVs, classed within the PEV subcategory) and plug-in electric vehicles (PHEVs) both utilize battery storage, where the PHEVs also have an internal combustion engine.[7] An interesting observation has been the reporting of the type of battery cathode type used over time, where different cathode chemistries have dominated dependent on country of use (US or China), as well as end application (BEV or PHEV). As of 2017, lithium nickel manganese cobalt oxide (NMC) chemistry has been the dominant cathode chemistry except for U.S. sold BEVs, which has been lithium nickel manganese aluminum oxide (NCA).[5] While it has been noted that these chemistries have provided additional benefits to previously used materials, such as lithium iron phosphate (LFP) and lithium cobalt oxide, (LCO), the next generation of cathode chemistry is needed. Reports suggest that lithium sulfur (Li-S) is the closest next generation to feasibility and implementation, however, notable challenges still need to be overcome.[5]

Based on the model of cost reduction and tight timetables, industry technology developers and manufacturers gear towards an optimization approach, where a system is adjusted and tweaked for improvements. This approach can be limiting to moving forward with next generation systems, as they often employ new materials, new architectures and new challenges. These challenges are multi-faceted and include overall cell safety, material toxicity, and sourcing of materials. Due to the complexity of the multiple components that comprise a battery, these types of approaches can have disastrous consequences, exemplified by the recall of all Samsung Galaxy Note 7 devices due to fires.[8] Additionally, subsequent mandates by the Federal Aviation Administration (FAA) in 2019 increased restrictions on lithium-ion powered devices in storage of commercial flights due to the high risk of thermal runway and fire.[9]

To approach such a complex and growing demand for safe and viable energy storage, there needs to be multiple solutions that can be incorporated into current and future EES development. Herein, this work will present on a multi-scale level, different energy storage studies can that are geared to address the demands and needs of varying applications. To highlight the diversity and uniqueness of the required breadth of approaches, several systems are presented in combination with different characterization techniques and analysis relevant to the system. This wholistic approach shows how an array of methodologies is needed to evaluate energy storage systems, and that investigation must occur from a materials level to a bulk electrode/working system level to understand a system in a way that can facilitate designed improvements without sacrificing potential safety.

Herein, the following examples will be discussed and summarized from previously published work. Contributions to each project are listed in the beginning of each section as well as in acknowledgements:

Chapter II: Self forming, rechargeable solid state battery. This will show proof of concept of a self-forming battery based on the lithium iodide (Li/I_2) couple with inclusion of 3-hydroxypropionitrile (HPN) additive, which eliminates the need for flammable organic electrolytes. Additionally, the role of the interface on cycling efficiency is discussed.

Chapter III: Materials design for lithium sulfur (Li-S) batteries, including development of novel electrodes by incorporation of tuned MoS_2 nanosheets, and electrodeposition of a sulfur-rich high capacity electrode.

Chapter IV: Incorporates physical and electrochemical measurements to correlate physical properties to electrochemical behavior in metal oxides and aqueous zinc chemistries. This will cover wettability and impedance mapping of surface treated magnetite, the role of silver in silver Hollandite ($Ag_xMn_8O_{16}$) in a zinc based aqueous electrolyte and temperature dependent phase transition of vanadium dioxide (VO_2).

Chapter V: Demonstrates role of theoretical methods to explain synthetic observations. Surfaces of Potassium Hollandite (KMn_8O_{16}) are evaluated and compared for their relative stability including partial and full tunnel structures.

1.1 Role of Funding Agencies

With such a critical portion of energy storage advances funded by government based sources, it is important to understand the role and interplay of various funding agencies that actively support energy storage research and large scale user facilities. While there are many sources of funding on multiple scales, ranging from individual PI grants to center based funding, this section will specifically address Department of Energy funding initiatives that are major sources of funding linked to the research discussed herein, including DOE Office of Science-Basic Energy Sciences (DOE BES), the Office of Energy Efficiency & Renewable Energy (EERE), and Office of Electricity (OE).

The Department of Energy Basic Energy Sciences (BES) implemented an Energy Frontier Research Center Program in 2009, whose aim was to bring together multi-disciplinary and multi institutional teams with the capability to tackle large problems that typically lie outside of the scope of a single investigator to advance energy technologies.[10] This effort focused on enabling these scientist led centers, where the center Director could operate and execute a wider mission based on a unified science theme and initiatives. Since 2009, DOE BES has funded 82 EFRCs in 40 states. In the 2018-2022 funding cycle, 46 EFRCs in 36 states were funded on the

scale of $~4M per year per center, including ~ 670 Senior Investigators, ~ 1500 students, postdoctoral fellows and technical staff and ~ 115 institutions.

The Office of Energy Efficiency and Renewable Energy (EERE) has strategic goals that have demonstrated a direct impact on the economy by employing a diverse portfolio of projects that are directed at impacting the future for energy, to develop clean energy technology and services both more available and reliable with lower costs.[11] EERE considers five core questions in developing its programs including whether the problem is high-impact, if EERE funding will make a large difference relative to existing funding from other sources, openness to new ideas to problems solving, how will EERE funding result in an enduring economic impact to the United states, and why this investment from the government is a necessity, instead of leaving funding purely to private industry. These questions frame the context for development of EERE funding. EERE has outlined an Innovation Model, consisting of three phases including Applied Research (Phase 1), Development and Demonstration (Phase 2) and Focus on Market Barriers (Phase 3). Along this path are decision paths that give EERE flexibility to end the investment, which can occur if the technology is considered less competitive, or after industry adopts the technology. EERE has identified seven strategic goals in which its programs are based. These goals and the plan is described in more detail in the full report for 2016-2020.[11] These include sustainable transportation, renewable power generation, energy efficiency, energy manufacturing, grid modernization, federal sustainability, and high-performing culture.

Within EERE, the Vehicle Technologies Office (VTO) provides support for research in early-stage R&D to facilitate the identification of new battery chemistries or new cell technologies. The goals of the VTO R&E are to reduce the cost of electric vehicle batteries to less than $100/kWh, increase range to 300 miles, and decrease charge time to less than 15 minutes by 2028. The projected cost target goal is based on achieving near parity with Internal Combustion Engine (ICE) vehicles. The levelized cost of a 300 mile BEV (at $0.28/mile), would then be comparable to ICE vehicles (at $0.27/mile). The ultimate goal for BEV battery is $80/kWh, which would bring the 300 mile cost down to $0.26/mile.[12] The Advanced Materials Research & Development area addresses fundamental issues regarding materials and electrochemistry in two categories: Next-generation lithium-ion battery technologies and beyond lithium battery technologies. VTO recognizes that cost reduction and electrochemical

improvements stem from materials levels improvements, and have invested heavily in these areas. The work discussed here (**Chapters II and III**) came from work supported through these programs. Part of the work reported in **Chapter III** (Materials Approaches for Lithium Sulfur Batteries) was funded in part by a seedling project, under Battery500, a Consortium effort consisting of four National Laboratories (PNNL, INL, BNL, and SLAC) and university partners whose goal is to develop a commercially viable Li battery with a specific energy target of 500 Wh/kg and the ability to undergo 1000 charge-discharge cycles.

The combination of combining funding on the materials and electrode level with an eye towards commercially viable scalable systems, enables research that has demonstrated benchmarked improvements both in cell development and cost reduction. This leads the way towards future work and collaboration between government, university and industry partnerships. From a larger, scalable perspective, the DOE Office of Electricity (OE) is directed by a mission of energy security and resilience on the grid scale. OE has identified four priorities that guide its mission and funding efforts including: (1) Development of a North American Energy Resiliency Model (NAERM) in concert with national laboratories and stakeholders, (2) Megawatt grid storage capable of energy management for bulk and distributed energy systems, (3) Pursuing sensing technology to develop predictive models for electricity, and (4) Transmission requirements including policy related issues. As one of the main four pillars of the OE, energy storage on a larger scale has been attracting more interest into development of scalable systems, outside of Li-ion batteries. These systems and chemistries include flow batteries, rechargeable Zn-MnO_2 batteries and Sodium based batteries. In collaboration with Sandia National Laboratories, the DOE OE maintains an ongoing list of grid-scale projects currently in commission worldwide.[13]

1.2 Basic operation of an electrochemical cell

While the medium may vary, electrochemical energy storage works by the transfer of charge (electrons) in combination of the movement of ions. Typically, in a lithium ion battery, there are multiple components that are required to enable charge transfer, ion diffusion, and prevent short circuits within the cell. A typical Li-ion battery contains a graphite based anode, where lithium ions can insert and (de)insert during cycling. On the opposite end of the cell, the cathode, which can be comprised of a variety of materials, such as transition metal oxides, can accommodate lithium intercalation, as shown in **Figure 1.1**.

The cathode is typically made into a composite and fabricated onto a current collector as a slurry. These composites often contain a conductive additive (such as carbon or carbon nanotubes) as well as a binding agent (such as polyvinylidene fluoride, (PVDF)) to ensure the electrical and mechanical stability of the electrode. A separator is housed between the anode and cathode components. The role of the separator is to allow ion mobility but to prevent electron mobility, since if electrons could freely move from anode to cathode, this would cause an internal short. In addition, an appropriate electrolyte must be selected based on compatibility, desired voltage range, and consideration of safety and environmental impact. Selection of the

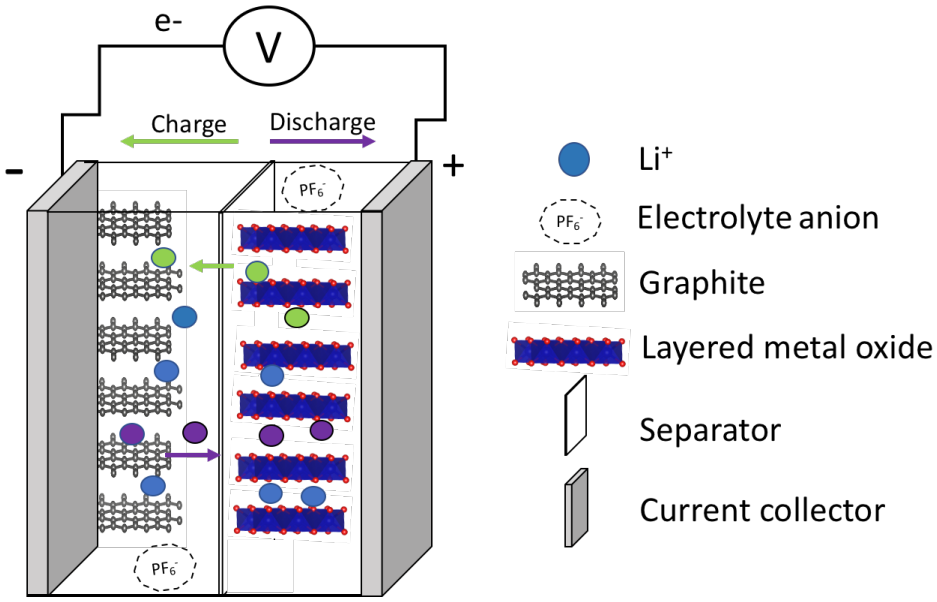

Figure 1.1. Schematic of an Li-ion full cell, showing a graphite anode, layered metal oxide cathode, separators, current collectors and free ions.

current collectors also critical in maintaining electrical contact with the active material, and allowing continuous cycling without considering side reactions. Other considerations, include the thickness of each component as well as the relative stack pressure, which can be a contributing factor to capacity retention over long term cycling.[14]

The following sections will provide a brief overview and background on the main topics herein.

1.3 Few Component Solid State Electrolytes

The following is adapted from the following publication:

Copyright © (2019) Cambridge University Press. Stackhouse, C., A., Abraham, A., Takeuchi, K. J., Takeuchi, E. S., Marschilok, A. C., Progress and Outlook on Few Component Composite Solid State Electrolytes, Stackhouse, C. *MRS Advances*, 4(49), 2635-2640. Reproduced with permission.

While traditional lithium ion battery (LIB) systems have been an attractive candidate to address the growing demand for energy storage needs, traditional LIBs have limitations including safety issues that stem from growth of lithium dendrite formation and the presence of flammable, reactive organic electrolytes.[15] In addition to improving safety conditions in a wide range of operating conditions, new manufacturing processes and facilities will need to be developed to address changing energy storage needs. Solid state systems, which include a solid state electrolyte instead of a liquid based electrolyte have been touted as an possible future alternative to lithium ion batteries, due to their reportedly higher thermal stability, lack of flammable liquid electrolyte, large electrochemical stability widow, and possible increased resistance to physical forces such as shock and vibration. Amongst a variety of solid electrolyte systems tested, including garnet solid state electrolytes,[16] sodium super ionic conductors (NASICON) electrolytes, and lithium phosphorous oxynitride (LiPON) electrolytes, the polymer electrolytes have exhibited the greatest amount degree of tractability and interfacial compatibility in addition to maintaining the inherent safety benefits of solid state electrolytes.[17]

There have been many reviews and reports to date that have reported extensively on the more widespread solid electrolyte systems listed above, including solid state batteries for

lithium[18-21], sodium[22, 23] magnesium[24, 25], Li-sulfur[26-28] and zinc[29] systems. A lesser reported area includes lithium iodide (LiI) based solid state electrolytes. The lithium iodide battery, based on the Li/I_2 couple is a primary battery that has been widely employed in implantable cardiac pacemakers.[30, 31] During discharge, Li^+ interacts with elemental I_2 to form an LiI layer. As discharge progresses, this layer becomes increasingly thicker, which leads to increasing cell resistance. This presents a unique opportunity for a rechargeable solid state battery, as the Li/I_2 chemistry naturally lends itself to forming its own "separator" upon discharge, however, the ability to recharge the cell as well as generate composites that enable higher ionic conductivity are limiting factors.

Previous work on lithium iodide containing solid electrolytes can generally be grouped into two categories: lithium solid-state composite electrolytes and self-forming or electrolytically formed batteries. Inherently, lithium iodide has low ionic conductivity (~ 10^{-8} S/cm), and the use of halide complexes has been reported to increase the conductivity.[32] Lithium solid state composite electrolytes (LiSCEs) are a variant of solid polymer electrolytes that are defined by the combination of nanoparticles and solid-state addition compounds based on the reactions of lithium iodide with small organic molecules.[33] This has included the introduction of other compounds, such as calcium iodide (CaI) with LiI which led to increases in ionic conductivity by the introduction of defect sites.[34] Much work focused on improving lithium ion conduction, where notable improvements were observed when a series of lithium halide compounds were tested, which was attributed to reorganization in the crystal structure.[35]

In later work, the compound 3-hydroxypropionitrile (HPN) was used as an organic additive to generate a series of composite electrolytes with LiI that incorporated both a hydroxy and a cyano group capable of coordination, giving this compound interesting properties, including coordinating with lithium, yielding a mobile I^- anion. [36, 37] Depending on the ratio of LiI : HPN (molar ratio), there was a wide range of observed ionic conductivities that did not have a linear dependence on increasing or decreasing the conductivity. For example, a maximum conductivity of 6.97 x 10^{-3} S/cm was observed with an LiI:HPN ratio of 1:15. There was a large notable decrease in conductivity observed when moving from the 1:4 to 1:2 ratio (LiI:HPN), from 3.1 x 10^{-3} S/cm to 2.36 x 10^{-6} S/cm, respectively. Instead of continuing to decrease on the relative reduction of HPN, there was a second maximum in ionic conductivity (1.1 x 10^{-4} S/cm)

as the ratio approached 2:1 (LiI:HPN). This type of behavior followed previously reported "polymer in salt" behavior.[38] One consideration of note, is the preference for the stoichiometric ($LiI(HPN)_2$) compound is due to the workability of the composite electrolytes. While other ratios of LiI:HPN have demonstrated higher ionic conductivity, they can be liquidus at room temperature, and may not be practical in applications in solid state electrolytes that include even mild heating.

Growing interest to improve battery technology to solid state electrolytes has necessitated the development of alternatives that can generate electrolytes with reduced manufacturing costs as well as development of electrolytes that can adapt to a wide range of environmental and operational conditions. The self-forming battery or electrolytically formed battery generates its own components (anode, cathode, separator), during a charge step, but until undergoing a charge step, the battery itself does not exist, and only exists as a single component solid electrolyte.[39-43] Upon application of a voltage to oxidize the composite, lithium is reduced to lithium metal and forms on the anode side. The corresponding oxidation product induces the formation of a polyiodide species at the positive electrode. The development and demonstration of a solid state $LiI(HPN)_2$ containing self-forming battery will be discussed in detail in **Chapter II**. Previous reports on electrolytically formed batteries, using the Li/I_2 couple have incorporated PVP and a lithium iodide hydrate. The development of the forming of separate electrode components was tracked by AC impedance spectroscopy, where Nyquist plots correlated depressed semicircles to correspond to ionic conduction of the electrolyte, ionic conduction of the solid electrolyte interface and charge transfer process within the cathode. However, incorporating a lithium hydrate noted an increase in impedance due to the formation of an insulating lithium hydrate layer. [40] The work discussed in **Chapter II** incorporates a HPN based compound, $LiI(HPN)_2$ that is combined with LiI (where LiI is the dominant compound) to form composite electrolytes. Self-forming, rechargeability, and decrease in AC impedance after charge and continued cycling has been observed. Additionally, the role of the interface was investigated to address the role of stainless steel, lithium, and gold interfaces in an operating electrochemical cell with the self-forming solid state electrolyte.

1.4 Lithium Sulfur Batteries

Reprinted (adapted) with permission from :

Wang, L., Abraham, A., Lutz, D. M., Quilty, C. D., Takeuchi, E. S., Takeuchi, K. J., Marschilok, A. C., Toward Environmentally Friendly Lithium Sulfur Batteries: Probing the role of Electrode Design in MoS_2-Containing Li-S Batteries with a Green Electrolyte, *ACS Sustainable Chemistry & Engineering,* **2019**, 7(5) 5209-5222.

Copyright © **(**2019) American Chemical Society.

Rechargeable lithium sulfur (Li-S) batteries have garnered significant interest due to both the high theoretical capacity of the sulfur cathode upon full conversion (1672 mAh/g) and the theoretical gravimetric energy density of 2800 Wh kg^{-1}.[44, 45] Additionally, sulfur is a highly abundant, nontoxic element that has a reasonable operating voltage (1.5 to 2.5V vs. Li/Li^+), thus making it both a sustainable and cost effective material for the future of high energy density batteries.[46] Despite its advantages, continued development and subsequent commercialization of the Li-S battery have been hindered by issues including the complexity of polysulfide dissolution, where parasitic reactions during the (dis)charge process can reduce the usable capacity, and also reduce the cycle life of the battery.[47-50] Additionally, sulfur inherently has a low electrical conductivity (5×10^{-20} S/cm), which provides additional challenges in feasibility and cell design.[51] Improvements to electrical conductivity often include incorporating some form of conductive matrix, which can be in the form of carbon, conductive polymer, or metal. Carbon nanotubes have been a choice additive in enhancing the electrical conductivity of sulfur, and various carbonaceous materials have also been included.[52-55]

To address the issue of polysulfide dissolution, a strategy such as "trapping" of the mobile polysulfide species by additives that have a demonstrated affinity towards the transitory polysulfide species has been explored.[56, 57] The approach of generating trapping materials, a wide variety of additives have previously been including into Li-S cells, including carbon sources, such as carbon nanospheres[58, 59] Ketjenblack,[60] carbonized eggshell membrane,[61] graphene sheets,[62] graphene coated cotton-carbon[63, 64] and carbon interlayers.[65] Additionally, other additives such as metal carbides,[66] 2D conductive MXene nanosheets,[67] and metal chalcogenides[68-70] have also been included.

In incorporating trapping agents, different design strategies have been employed, which can be demonstrated by recent reports of MoS_2 incorporation into Li-S cells. For example, MoS_2 has been investigated as an additive to sulfur cathodes[46, 71, 72] as well as in coating form on separators.[73, 74] The increasing incorporation of MoS_2 as a polysulfide trapping agent extends on previous work that showed enhanced binding affinity for lithium polysulfide species to MoS_2. For example, ab initio density function theory (DFT) studies indicated higher binding energies for lithium polysulfide species: Li_2S_8, Li_2S_6, Li_2S_4, Li_2S_2 and Li_2S species on the MoS_2 surface with reported binding energies of 0.10, 0.22, 0.32, 0.65 and 0.87 eV for Li_2S_8, Li_2S_6, Li_2S_4, Li_2S_2 and Li_2S, respectively.[75] The enhanced binding of the MoS_2 substrate originate from the interaction of Li atoms in the Li_2S_n with MoS_2.[76, 77] In addition, simulations further confirmed selectivity of Li_2S_n binding to MoS_2, with an increased affinity for binding to edge sites relative to planar surfaces (referred to as "terrace sites"). The comparison of edge site to terrace site affinities was described by DFT calculated binding energy, where the binding energy showed lower binding energy of the Li_2S_n to the MoS_2 terrace site (~0.87 eV) relative to the Mo- and S-edge sites (which had binding energies of 4.48 and 2.70 eV, respectively). This could potentially be attributed to the lower coordination environment that exists on predominantly on the edge sites, compared to terrace sites. The MoS_2 terrace site had a higher binding energy when compared to graphene (0.29 eV), which further indicated that there was preferential binding to MoS_2 other materials.[78] Therefore, generating MoS_2 with greater edge site availability (such as nanosheets) could potentially increase its ability to trap polysulfides.

Previous studies have generated MoS_2 nanosheets by heating Mo and S precursors in a reactor, where employing the use of a microwave reactor[79] has shown a reduction in time from 18h to 2h compared to hydrothermal preparations.[80] The work discussed herein, will discuss tuning of Mo:S ratio (and concentration) to develop MoS_2 nanosheets that both have different morphological and physical properties, as well as varying impact on electrochemical cycling when including in electrochemical cells. In addition to Mo:S ratio tuning and concentration, a separate discussion will address the synthesis method (hydrothermal, solvothermal, and microwave) and its resultant impact on morphology and subsequent electrochemistry. Additionally, the inclusion of an electrodeposited MoS_2 by either an "anodic" or "cathodic" deposition conditions, generates a sulfur rich MoS_x electrode that exhibits different

electrochemical properties based on the deposition conditions. **Chapter III** will provide a multi-faceted approach to addressing the role of MoS_2 based materials in lithium sulfur batteries.

1.5 Material properties and electrochemical response

Tuning of materials and evaluating their electrochemical response has been an area of interest in various fields, ranging from sensor technologies,[81] to materials for energy storage.[1] Depending on the system of interest, different approaches to characterization and electrochemical analysis may be required including techniques that address different material scales, as well as differentiating surface from bulk analysis. Utilizing these types of complementary techniques can provide insight both into bulk and localized properties of a material, and/or system to be interrogated. This is critical, as to be able to appropriately diagnose and improve energy storage materials, the physical properties, transport behavior, and bulk system electrochemistry must be studied in a synergetic fashion relating structure to function. Following are examples of employing techniques to correlate observed trends to physical or electrochemical material properties. First, the approach of using a multiscale investigation model is presented. Magnetite, Fe_3O_4 is presented as a model system, where the approach of a multi-scale model to understanding materials and working systems is described in **Chapter IV**, Section 4.1. Section 4.2 continues with magnetite, and describes employing electrode scale surface techniques to compare properties of surface treatments, which can be correlated to electrochemical properties. Section 4.3 expands on surface techniques, this time introducing a different system, where the mechanism of the (dis)charge is reported, and the role of silver is evaluated. Section 4.4 briefly describes a polymorphic metal oxide, VO_2 that undergoes a phase transition from monoclinic to rutile structure at 68°C, and discusses the impact of this phase transition on resultant electrochemistry. These examples highlight a variety of approaches in varied systems that correlate physical properties to subsequent electrochemistry.

1.6 Density Functional Theory

Density Functional Theory, (DFT) is a widely used theoretical approach for calculating the ground state energy of a system.[82] DFT provides the total energy of a system by relating the ground state energy to the electron density, ρ resulting in the following equation, where, and in Kohn-Sham formalism, the total energy, E, is given by:[83]

$$-\nabla^2 + V_H[\rho(\boldsymbol{r})] + V_N(\boldsymbol{r}) + V_{XC}[\rho(\boldsymbol{r})])\psi_i(r) = E_{i\psi i}(\boldsymbol{r}) \qquad \textit{Equation 1-1}$$

Where $-\nabla^2$ represents the electron kinetic energy, V_H is the Hartree term which represents the electrostatic energy of an electron moving in a mean electrostatic field due to the presence of other electrons, V_N represents the energy due to the nuclei, and V_{XC} is the exchange-correlation energy.[84]

Theoretical calculations of materials can provide insight into identifying target materials with particular properties that can then subsequently be tested in the laboratory. Additionally, Density Functional Theory (DFT), can offer insight into repeated experimental observations that may be challenging to explain by purely chemical means. By comparing the calculated energy of a range of structures, trends can be observed in regards to thermodynamic stability, which can in turn offer insight and make predictions into the predominant pathway in developing a particular synthetic material. **Chapter V** will specifically addresses the role of surfaces in potassium hollandite (KMn_8O_{16}). DFT was conducted on various terminations of the surface planes (0 0 1), (1 0 0), (1 1 0) of KMn_8O_{16} surfaces to provide insight into relative energy changes in the major surfaces to evaluate comparisons of cleavage energy and primary phase dominance. The role of incorporating full and partial structures was also evaluated.

Chapter II

Demonstration and Interface Effects in the Self-Forming Solid State, Rechargeable Li/I_2 Based Battery

Reproduced with permissions from the following publications:

Republished with permission of IOP Publishing, Ltd.., from: Communication- Demonstration and Electrochemistry of a Self-Forming, Solid State Rechargeable LiI$(HPN)_2$ Based Li/I_2 Battery, Abraham, A., Huang, J., Smith, P. S., Marschilock, A. C., Takeuchi, K. J., Takeuchi, E. S., *J. Electrochem. Soc.,*165(10), A2115-A2118. Copyright © 2018; permission conveyed through Copyright Clearance Center, Inc.

Copyright (2019) © Cambridge University Press. Abraham, A., Dunkin, M. R., Huang, J., Zhang, B., Takeuchi, K. J., Takeuchi, E. S., Marschilok, A. C., Interface effects on self-forming, rechargeable Li/I_2-based solid state batteries *MRS Communications,* **2019**, 9, 2, 657-662. Reproduced with permission.

Personal contributions: Development of composite solid electrolytes for proof of concept demonstration, including identification of electrolyte candidates for down-selection for final composite testing. Development of measurement protocol for solid electrolyte AC impedance measurements, development of multiple cell configurations and adjustments to testing conditions. Development and optimization of interface modification, and adjustments to testing protocols for cells. Responsible for collecting data to meet project targets, reporting requirements and contributions to quarterly reports, annual reports and manuscript preparations.

Acknowledgement of collaboration:

Dr. Jianping Huang- Co-development of composite solid electrolytes, material synthesis and characterization, initial electrochemical testing and charging protocols, initial development of cell constructions *(J. Electrochem. Soc.,* **2018**, 165(10), A2115; *MRS Commun.,* **2019**, 9, 657). Contributed to **Figures 2.5, 2.6A-B** included herein.

Dr. Paul F. Smith – Preparation of solid composite electrolytes and electrochemical testing *(J. Electrochem. Soc.,* **2018**, 165(10), A2115).

Mikaela Dunkin – Solid electrolyte, coin cell preparation. Characterization and analysis by X-ray diffraction of solid state electrolytes (*MRS Commun.,* **2019**, 9, 657).

Dr. Bingjie Zhang – Characterization of composite solid electrolytes by SEM and SEM-EDS *(MRS Commun.,* **2019**, 9, 657).

2.0 Introduction

Lithium based battery systems are attractive due to their high energy densities, however, safety issues resulting from the organic electrolyte and dendritic Li formation are major concerns.[85] Solid state batteries have been identified as an emerging possibility for high density and safe electrochemical energy storage solutions. Much progress has been made to understand the role of ionic conductivity, composition and structure of solid electrolytes for Li- and Na-based inorganic ion conductors.[15] Solid state electrolytes provide an opportunity to replace the flammable liquid electrolyte that has been widely utilized in most systems.[86-90] Despite advances in conductivity which had previously been prohibitive in solid state batteries, the lithium/solid state electrolyte interface can lead to compromised cell performance. For example, $Li_{9.54}Si_{1.74}P_{1.44}S_{11.7}Cl_{0.3}$ exhibited high ionic conductivity (0.025 S/cm), but had poor electrochemical stability in a lithium battery.[91] $LiCoO_2/Li_{9.54}Si_{1.74}P_{1.44}S_{11.7}Cl_{0.3}$/Li delivered a low initial Coulombic efficiency (39%) attributed to interfacial side reactions.[91] Thus, it is critical to consider multiple variable in development of solid state electrolytes, including reasonable ionic conductivity, electrochemical stability versus Li metal, and reduced interfacial resistance.

Self-forming batteries can be envisioned where the anode and cathode are formed upon charge from a single solid electrolyte. The Li/I_2 couple is an attractive target due to its high energy density (1536 Wh/L, 560 Wh/kg) and opportunity to self-heal. Notably, the primary Li/I_2 battery has been a successful technology as the power source for pacemakers.[2, 3] Previous reports of self-forming solid state batteries have been limited where Li/I_2 based batteries have used either $LiI{\cdot}H_2O$/poly(vinyl-pyrrolidone) (PVP),[39, 41, 92] anhydrous LiI/PVP composite[39, 41] or a metal to alloy with lithium.[39] The LiI electrolyte has been proven to form Li/I_2 cells upon charging was initially demonstrated using a $LiI{\cdot}H_2O$/(PVP) composite.[40] $LiI{\cdot}H_2O$ was initially proposed as an alternative electrolyte because of its higher ionic conductivity ($\sim 2\times10^{-5}$ S/cm) relative to LiI

(~10^{-8} S/cm).[93] However, the charged LiI·H_2O cell showed increased impedance leading to high overpotential due to solid-electrolyte interphase (SEI) layer formation over time.[40] A follow up report evaluated two strategies in addressing the solid electrolyte interface including the use of an alloying current collector such as In, Al and Ga. [39] Separately, the authors reported visualization of the dendritic growth of lithium plating on an interdigitated cell design. [41]

To translate the Li/I_2 system into a viable secondary battery, a different additive, lithium iodide-(3-hydroxyproprionitrile)$_2$ (LiI(HPN)$_2$)[37, 94] has been proposed. LiI(HPN)$_2$ is described as an anion conducting compound, where I^- is the mobile anion,[95] as proposed by *ab initio* density functional total energy calculations which showed I^- hopping to have a significantly lower activation energy (0.73 eV) than Li^+ (8.39 eV).[96] Examples of the inclusion of LiI(HPN)$_2$ into a secondary battery system include a secondary Li/I_2 battery formed by depositing a thin solid LiI(HPN)$_2$ layer onto lithium, followed by exposure to I_2 vapor, yielding an I_2-LiI(HPN)$_2$ compound as the cathode. This exhibited effective electrochemical cycling under 20 μA/cm^2, and discharge plateaus at ~2.7 V.[94] Additionally, A Li/LiI(HPN)$_2$/I_2 based thin film battery utilizing LiI and LiI(HPN)$_2$ powders with a lithium foil anode exhibited improved energy density (~250 Wh/kg) and higher charge-discharge capability (250 μA/cm^2 at 70^o C).[97] Studies into this system have been relatively limited, and often initially include lithium metal with LiI(HPN)$_2$.

In addition to the chemistry of solid state battery operation, the system is further complicated by the presence of the interface, which has been a major challenge in further development of solid state electrolytes. The interface refers to the junction between the solid electrolyte and other active materials (in a traditional multi-component solid state assembly), as well as to the current collector interface with the active materials. A major challenge facing further development of solid state electrolytes is addressing interfacial issues that can occur between the solid electrolyte and the active materials. Several strategies have been adapted to reduce interfacial resistance, mostly for garnet based solid electrolytes, including replacing the Li^+ blocking lithium layer with the introduction of a Li^+ conducting Li_3N layer [98], deposition of a 20 nm germanium layer to decrease garnet/Li-metal interfacial resistance by alloying [90], the use of a liquid phase processed Li_2SiO_3 buffer layer between a garnet and NMC interface [99], and the use of atomic layer deposition (ALD) to deposit an ultrathin Al_2O_3 coating on garnet solid

electrolytes which demonstrated a decrease in interfacial area specific resistance from 1,710 Ω/cm^2 to 1 Ω/cm^2.[100]

An alternative concept to a multi-component solid state battery consists of a different solid state cell design concept, where the solid electrolyte initially exists as a single composite and is formed into separate anode, cathode and separator components upon charge. The battery is activated on the first charge forming the negative and positive active materials in-situ. The benefits of a solid electrolyte which form an anode, separator and cathode upon charge include fewer cell components during processing and reduced risk of self-discharge before formation of the active battery, thus providing the ability to store the solid electrolyte for extended periods of time.

Herein, the demonstration of a rechargeable fully self-forming solid state lithium battery with the inclusion of $LiI(HPN)_2$ is described. By starting with a single composite solid state electrolyte (containing LiI and $LiI(HPN)_2$), upon charge, the composite was able to separate into anode, cathode and separator, as shown in the schematic in **Figure 2.1**. After initial efforts in development of a solid state electrolyte with improved ionic conductivity, the effect of charging on impedance of the cell was investigated, and proof of concept was demonstrated by stable open circuit potential and cyclability of constructed cells. Additionally, characterization of the solid electrolyte obtained before and after charge supported observations seen in the electrochemistry. (Details of the characterization methods can be found in the full literature reports.[42, 101]) Subsequent studies addressed the role of the interface both before, during and after cycling. **Section 2.2** describes initial interface studies, where initially both interfaces (positive and negative) utilized metal (stainless steel, lithium, gold) substrates**.**

In the composite solid electrolytes, only the lithium iodide is treated as electroactive material, noting the following reactions upon charge and discharge:

Charge: $Li^+ + e^- \rightleftharpoons Li$ (anode) *Equation 2-1*

$I^- \rightleftharpoons \frac{1}{2} I_2 + e^-$ (cathode) *Equation 2-2*

$LiI \rightleftharpoons (1-2n)LiI + 2nLi + nI_2$ (Full cell) *Equation 2-3*

Discharge: $\frac{1}{2} I_2 + Li \rightleftharpoons LiI$ *Equation 2-4*

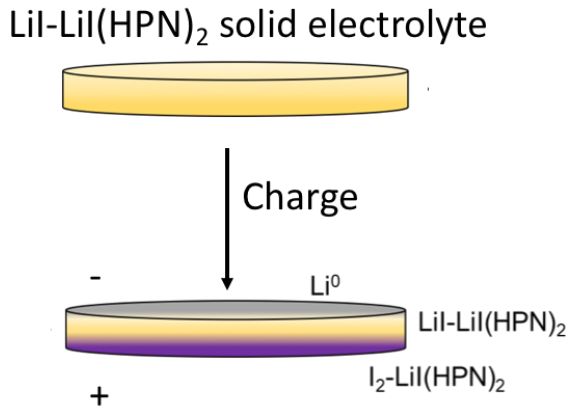

Figure 2.1. Schematic of self-forming solid state electrolyte, where positive (+), negative (-) and separator components form upon charging.

Following demonstration of a fully self-forming solid state Li battery, where the lithium anode and iodine cathode are both generated *in-situ* upon initial charge, the role of the solid electrolyte current collector interface is investigated with a LiI-LiI(HPN)$_2$ solid electrolyte. Characterization after activation was conducted using x-ray diffraction of both the positive and negative interfaces of the solid electrolyte. Increases in Coulombic efficiency of ~ 2X after multiple cycles were observed by incorporating thin Li metal to the negative electrode side of the solid electrolyte interface. This self-forming Li/I$_2$ battery system is appealing for systems requiring high energy density and safe function with low power requirements, including applications in implantable medical devices, power sources for long life sensors, as well as backup power for electronics.

2.1 Experimental

Synthesis and formation of composite solid state electrolytes

Lithium iodide-(3-hydroxypropionitrile)$_2$, (LiI(HPN)$_2$ (formula - LiI($C_3H_5NO)_2$) was prepared following a previous report[37] where molar ratios of LiI and 3-hydroxypropionitrile(HPN) (1:2) were combined by heating. The solid product was characterized by x-ray diffraction. For tests of ionic conductivity, composite solid electrolytes were generated from synthesized LiI(HPN)$_2$ and with LiI to form x% LiI/ y% LiI(HPN)$_2$, where $100 \geq x \geq 70$, and $30 \geq y \geq 0$ (x, and y represent mass percentages). Ionic conductivity was obtained by measuring Electrochemical Impedance Spectroscopy (EIS) over a temperature range of 28-42°C at 1 MHz - 1 Hz, modeled using Zview Software. Coin cells were fabricated using only the composite electrolyte. Coin type cells were constructed using the composite solid electrolytes (either 86% LiI /14% LiI(HPN)$_2$ or 80% LiI /20% LiI(HPN)$_2$ (by mass)) with a diameter of 10mm and an average thickness of 0.4 mm. For capacity calculations for electrochemical testing, only the capacity contribution of the LiI (not the LiI(HPN)$_2$ additive) was considered as the active material.

Interface studies

Cells were fabricated using either stainless steel (ss) or gold (Au) current collectors. For cells with an additional Li interface, thin lithium metal (~ 70 μm) was used between the solid electrolyte and the current collector on the negative electrode side. Thin Li foil was punched using a hollow punch and attached to a stainless-steel current collector. A wire bristled brush was used to remove any residual oxide layer as well as ensure even contact between the current collector-Li and the Li-solid electrolyte interfaces. The lithium was stacked with the solid electrolyte prior to crimping the cell. Cells were crimped for 30 seconds to ensure even crimping. Electrochemical Impedance Spectroscopy (EIS) was obtained in a frequency range of 1MHz to 1Hz at 30°C. Galvanostatic Cycling with Potentiostatic Limitation (GCPL) for charge and discharge cycles was collected using constant current normalized per surface area of the electrode. All cell testing was performed using a BioLogic VSP. All materials handling and processing was performed within a dry room (dewpoint -40°C) and cell assembly was done within an argon filled inert atmosphere glovebox maintained at < 5ppm O_2 and < 0.5 ppm H_2O.

2.2 Results and Discussion

2.2.1 Composite solid electrolyte development

A series of solid electrolytes was measured with EIS as a function of temperature,[102] An equivalent circuit model was used (**Figure 2.2, inset**), including a resistor (R1), capacitor (C1), and two Constant Phase Elements (CPE1, CPE2) to represent bulk resistance, capacitance, and ion movement, respectively.[103] Electrolyte resistivity, $\rho=RS/l$ and conductivity, $\sigma = l/RS$ were determined using measured resistance, R, contact area, S, and thickness, l, of the electrolyte. **Figure 2.2** shows a representative temperature series of EIS measurements measurement of the 80% LiI/20% $LiI(HPN)_2$ (80/20) solid electrolyte, with the circuit model used for fitting in the inset. There is a notable decrease in impedance observed with increasing temperature, even with a low upper end of the temperature range (42°C). From the initial data, the obtained R1 value is obtained by fitting, and then utilized to determine the conductivity of multiple compositions of solid electrolyte, ranging from a pristine LiI solid composite, to LiI + $LiI(HPN)_2$ composite electrolytes, including $LiI(HPN)_2$ additive amounts ranging from 5% to 30%.

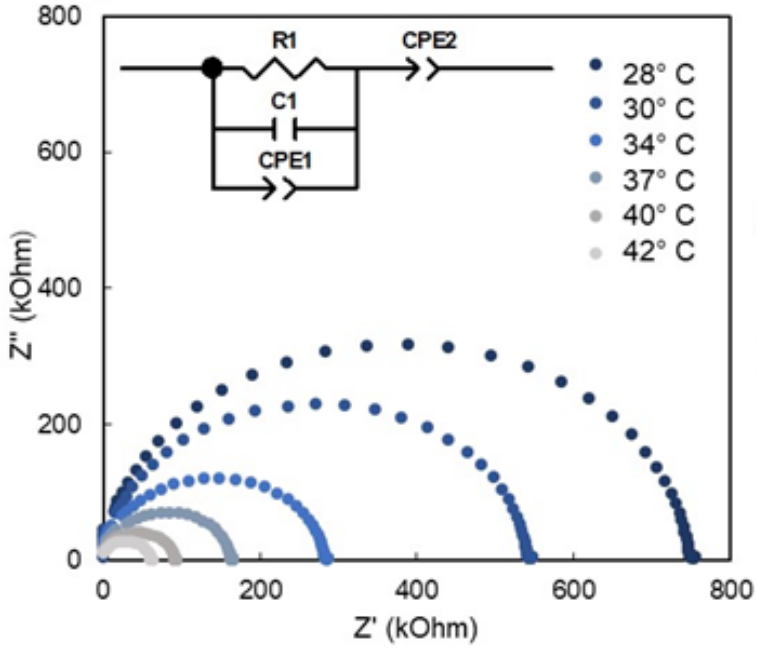

Figure 2.2: Representative ACI data from 80% LiI/20% LiI(HPN)2, with equivalent circuit model (inset) used for analysis.

Arrhenius plots of specific conductivity versus the inverse of temperature conductivity, visualizing the order of magnitude (y-axis), and note the type of relationship over a temperature range for a system of interest. This approach has previously been shown using solid LiI based electrolytes.[102, 104] **Figure 2.3** shows plots of log [σ(S cm^{-1})] versus 1/temperature (10^3 T^{-1} (K)) for the four composite solid electrolytes: 95% LiI-5% $LiI(HPN)_2$, 90% LiI-10% $LiI(HPN)_2$, 80% LiI-20% $LiI(HPN)_2$, 70% LiI-30% $LiI(HPN)_2$, and pristine (100%) LiI. Resultant conductivity at 30° C for 80/20 was 1.7 x 10^{-7} S/cm, similar to the 70/30 electrolyte (1.9 x 10^{-7} S/cm), and higher than both the 90/10, and 95/5 electrolytes, 6.6 x 10^{-8} S/cm, and 4.3 x 10^{-8} S/cm, respectively. The 80% LiI/20% $LiI(HPN)_2$ (80/20) was selected for further study as this composition allowed for retention of significant active material (LiI) in the solid electrolyte, while improving conductivity approximately an order of magnitude over that of pristine LiI (3.2 x 10^{-8} S/cm, reported at 25°C).[102]

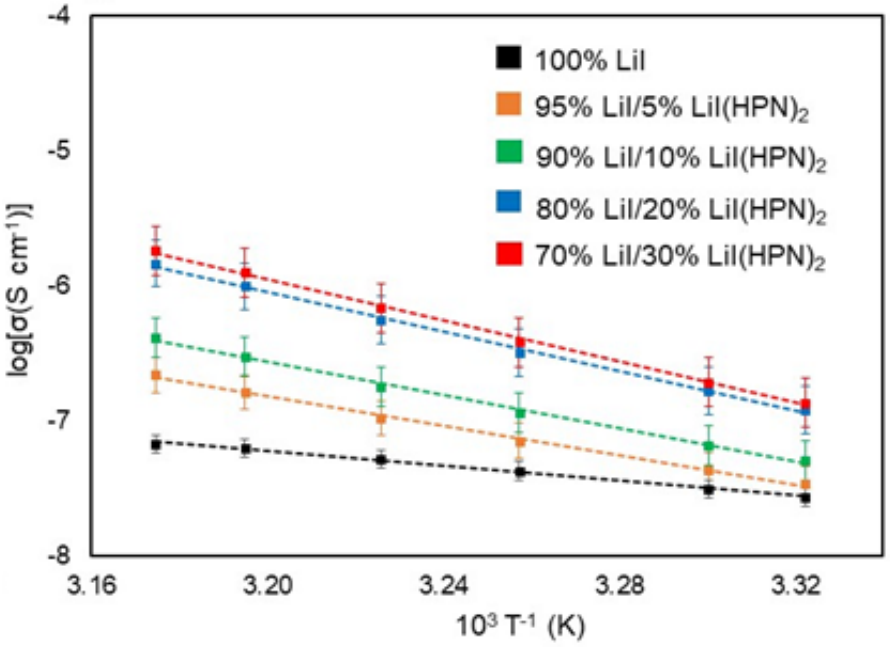

Figure 2.3. Conductivity of LiI and $LiI/LiI(HPN)_2$ solid electrolytes.

Activation energy (E_a) (Equation 2-5) was determined where σ is the conductivity (S/cm), K_B is the Boltzmann constant (eV/K), and T is the temperature (K).[103]

$$\sigma = \sigma_0 e^{-Ea/K_B T} \qquad \textit{Equation 2-5}$$

$$ln\sigma = ln\sigma_0 - E_a/K_B T \qquad \textit{Equation 2-6}$$

The E_a of the composite electrolytes increased slightly with decreasing LiI content with 95/5, 90/10, 80/20, and 70/30 having E_a of 1.1, 1.2, 1.5, and 1.5eV, respectively.

XRD was used to characterize the synthesized $LiI(HPN)_2$ and the 80% LiI/20% $LiI(HPN)_2$. All the peaks of the synthesized sample were assigned to $LiI(HPN)_2$ with a monoclinic structure, whose structure is shown in **Figure 2.4** generated from reference.[95] When LiI was mixed with $LiI(HPN)_2$, (80/20), new peaks (29.6°, 42.5°, and 50.4°) attributed to LiI (ICSD #27983) were also observable.[97]

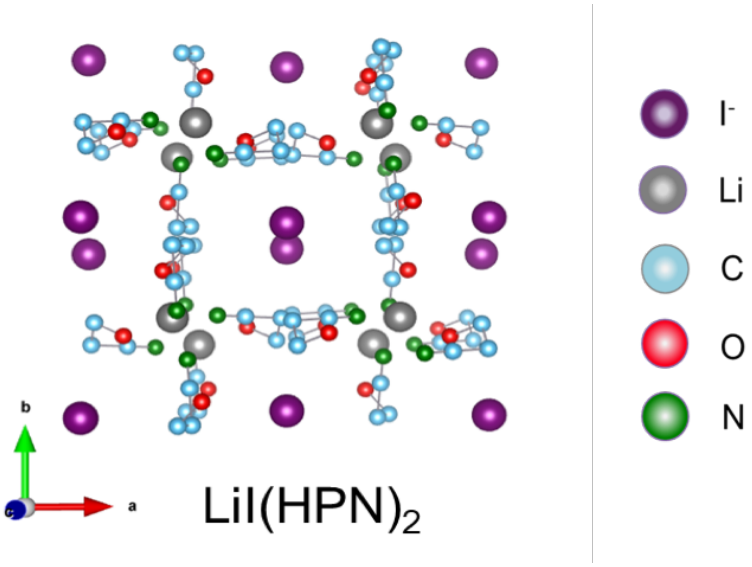

Figure 2.4. Crystal structure of $LiI(HPN)_2$, with chemical formula $LiI(C_3H_5NO)_2$

To evaluate the relative homogeneity and particle aggregate shape of the composite solid electrolyte, SEM data were collected to observe the surface homogeneity of the pristine 80 LiI - 20 $LiI(HPN)_2$ solid electrolyte, It was observed that the morphology of the composite with uniformly distributed $LiI(HPN)_2$ rods and 5-6 micron aggregates of LiI particles, where the inclusion of energy dispersive spectroscopy helped to identify the LiI fron $LiI(HPN)_2$ $LiI(C_3H_5NO)_2$. Energy Dispersive Spectroscopy (EDS) was used to identify the carbon in $LiI(HPN)_2$, chemical formula $LiI(C_3H_5NO)_2$, and differentiate from the more iodine rich LiI. It

was found that the carbon provided the framework for the rod structure of $LiI(HPN)_2$, while the iodine, primarily as LiI, formed the particle-structure. Thus, SEM characterization demonstrated the formation of an integrated composite LiI-$LiI(HPN)_2$ solid electrolyte. XRD characterization of the charged solid electrolyte was obtained on both anode and cathode sides of the solid electrolyte, where the negative side of the pellet faced the x-ray. There was not an observed difference in intensity between the diffraction pattern of the anode and cathode sides, attributed to penetration of the x-rays through the solid electrolyte during both measurements. X-ray diffraction showing formation of the I_2-$LiI(HPN)_2$ complex upon charge can be found in the full report.[101]

2.2.2 Demonstration of cell formation upon charging

Before charging the cells showed a resistance of 200-300 kΩ. The cell was charged to 5% capacity using a step-wise approach (5, 10, and 20 μA/cm^2), as shown in **Figure 2.5.** The inclusion of setting up step-wise charging program allowed the cell to charge continuously, as the resistance reduced upon charging. If too large of a current was initially applied, large overpotential would prevent the cell from charging.

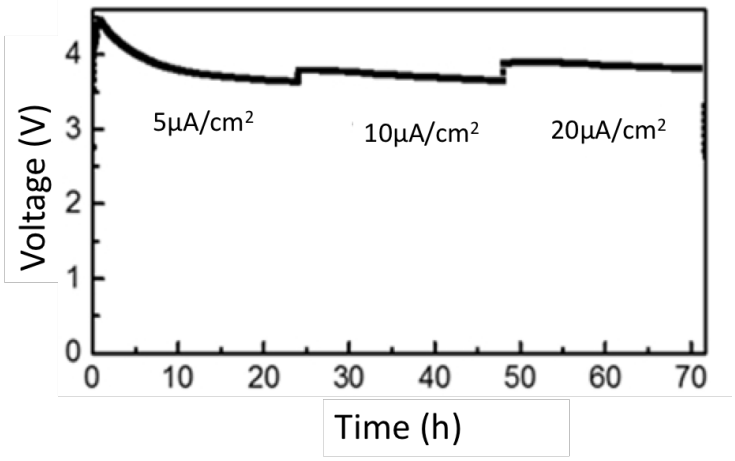

Figure 2.5. Example of step-wise charging with increasing current density over time.

Electrochemically, upon charging by the step-wise approach noted above, the cells maintained a stable OCV between 2.7-2.8V, corresponding to the Li/I_2 couple. An interesting trend was observed upon charging of the solid electrolytes even to small percentage (~0.5%) of their theoretical capacity, where a notable decrease in resistance upon charging was observed. To further examine the impact of charging on cell resistance, a study was conducted tracking the resistance as a function of percent charge of the solid electrolyte. Upon charging to 0.5% of theoretical capacity, a large (~ 5x) resistance drop was observed, and the resistance remained low at ~30-40 kΩ with minor changes upon additional charging. Formation of the Li/I_2 couple was verified by a 2.7 V OCV.[94] Since <10% of the electrolyte was utilized under charge, a decrease in the electrolyte thickness cannot account for the significant decrease in cell resistance. Thus, the significant decrease in impedance can be attributed to decreased interfacial resistance upon formation of Li at the anode and I_2 at the cathode.

Galvanostatic cycling was performed to test the feasibility as a secondary cell. Cells were charged to capacities of 5%, (0.66 mAh) by the stepwise procedure, **Figure 2.5**. Discharge was then performed at 10 μA/cm^2 to 0 V, followed by charge at 10 μA/cm^2 to 1.4% charge, followed by 20μA/cm^2 for 3.6% charge. Stable discharge capacities >0.15 mAh/g were maintained over 5 cycles. In comparison to the as-prepared cell impedance (~200 kΩ) a significant decrease in impedance was observed upon charge (17 kΩ), followed by an increase upon discharge (115 kΩ). The impedance trend remained consistent over the five cycles, with lower impedance (~20 kΩ) at the end of each charge step, and higher impedance (~100 kΩ) at the end of each discharge step.

2.2.3 Comparison of variation in metal current collector interfaces

Comparison of stainless steel-stainless steel and stainless steel-Li interfaces

After demonstrating self-forming feasibility, and observed reduction in impedance upon charging, the current collector-solid electrolyte interface was evaluated. Coin cells were constructed with 86 LiI - 14 $LiI(HPN)_2$ solid electrolytes where cells either contained a stainless steel current collector at the negative and positive interfaces, or the addition of a thin (~ 70 micron) layer of Li foil at the negative interface. Before charging, EIS was obtained, and the cell without Li foil had an impedance value that was > 2X that of the Li foil containing cell (1.8 MΩ

cm^{-1} for the ss-ss only cell compared to 0.85 MΩ cm^{-1} for the Li containing cell). Initially the cells are activated by a charge step, where they were charged at constant current (10 μA/cm^2) to 5% state of charge (SOC). As noted by the arrow in Figure 3B, upon charging there is a notable difference in overpotential observed between the cell constructs with and without the added Li foil. The Li foil containing cell showed a charge potential of around 3.3 V, with a fairly horizontal plateau. In comparison, the cell containing the same solid electrolyte, but without any external Li foil had a larger overpotential reaching ~ 4 V, before reaching a similar voltage under charge as the cell with Li foil after ~ 0.70% charge. Thus, with charge of ~ 0.70%, the overpotential of the two cell designs was the same with or without the incorporation of lithium foil.

Comparison of stainless steel-stainless with gold-gold and lithium-gold interfaces

A new set of cells containing the 80 LiI - 20 $LiI(HPN)_2$ were fabricated with either stainless-stainless (ss-ss) (anode-cathode), gold-gold or Li-gold interfaces. AC Impedance was obtained before charge (**Figure 2.6A**), and after charging to 5% capacity (0.63 mAh) (**Figure 2.6A,** post-charge denoted by arrow). Before charging, cells both with and without Li foil had an impedance in the kΩ range, and a typical variation in pre-charge impedance with ss-ss interfaces ranged from 200-300 kΩ before charge. Cells were tested by step-wise charging, where they were charged at 5 μA/cm^2, 10 μA/cm^2, 20 μA/cm^2 then discharged at 10 μA/cm^2 to 0.1V for a total of five charge-discharge cycles, as shown in **Figure 2.6C**.

The resistance (in kΩ) was shown as a function of charge or discharge with respect to the cycle number (**Figure 2.6B**). The resistance shown in **Figure 2.6B** was determined from AC Impedance measurement, where the resistance value was obtained from the low frequency x-axis intercept of the Nyquist plots. All three cell configurations showed a reduction in resistance upon the first charge, with a gradual increase of resistance upon subsequent discharge cycles. An interesting trend was observed regarding the charge and discharge resistances reported beginning with the first charge cycle **(Figure 2.6D).** Upon initial charge, the cell containing stainless steel current collectors had a near 6-fold reduction in resistance, compared to an ~ 6.5-fold reduction for the cell that contained a lithium foil and single gold interface (Li + Au), and a ~ 7.5-fold reduction for the cell construction with two gold interfaces (Au + Au). Upon discharge, all three cell designs returned to much lower resistance compared to their initial

resistance values, yet higher than the values when charged. Over the course of the following four charge-discharge cycles, the post charge resistance returned near to the original value for each of the three cell constructions (with Cycle 5 being within 10-17% of the original (Cycle 1) charge values. However, the cells varied much more noticeably between cycle 1 and cycle 5 on their reported discharge resistances (within 15-29% of the original (Cycle 1 discharge value). Interestingly, amongst the tested cells, the cells with the lithium and gold interfaces had the highest Coulombic efficiency even though the resistance on discharge was the highest among the group (**Figure 2.6D).** These results imply that there is some loss of active lithium in the cell charge process leading to inefficiency that is offset by inclusion of supplemental lithium metal in the cell design.

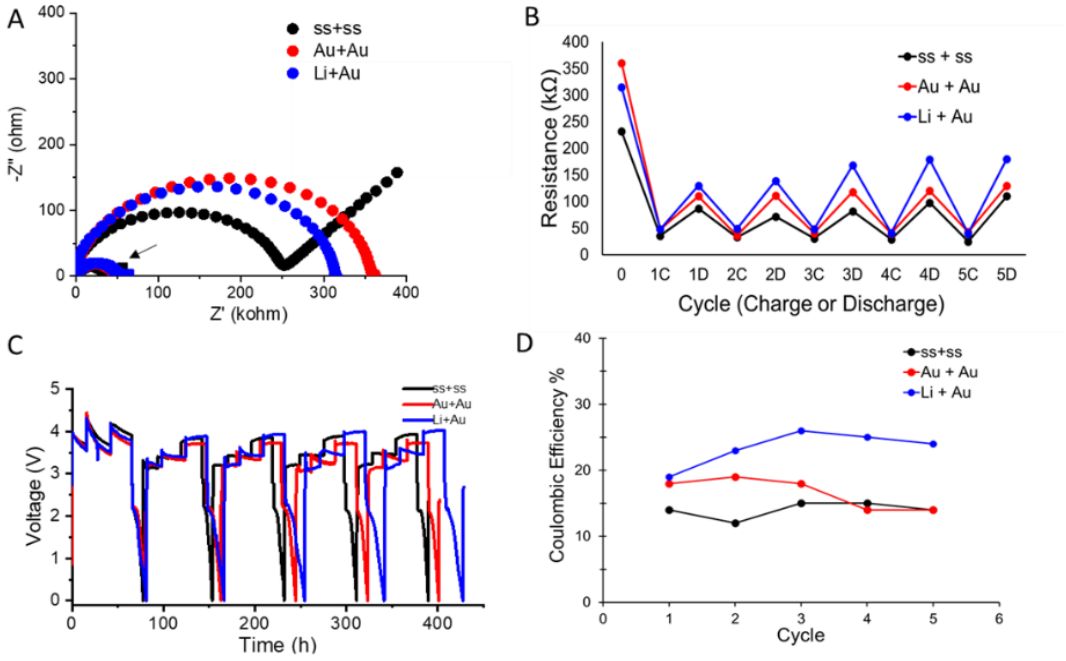

Figure 2.6. (A) Pre-charge AC impedance after 5% charge (arrow). (B) Comparison of resistance as a function of charge or discharge cycle. (C) Voltage versus time curves of step-wise charging of cells for five charge-discharge cycles. (D) Comparison of Coulombic efficiency for each cycle.

2.3 Conclusions

Demonstrated feasibility of a self-forming rechargeable LiI/I_2 cell using LiI/LiI$(HPN)_2$ electrolyte has been reported. *In situ* formation of a Li/I_2 electrochemical cell has been verified by OCV stability at 2.7 V, and formation of I_2 at the cathode was verified by XRD. A significant reduction in impedance is observed after the first charge cycle. Effective discharge-charge cycling of the cell was also demonstrated. The effects of the interface were explored in a variety of solid electrolyte-current collector interface using either stainless steel, gold or Li metal. The addition of Li metal improved the Coulombic efficiency of the HPN containing LiI solid electrolytes. The addition of Li metal to the anode interface contributed to a reduced overpotential observed during the initial charge step. The addition of an additional Li source increased the Coulombic efficiency by nearly a factor of two compared to the cells without external Li foil, in spite of higher observed resistance after discharge. The results imply that there is some loss of active lithium over repeated charge/discharge cycles. These results indicate the importance of the lithium source and the solid-electrolyte interface, showing promise for the future development of high energy density solid state self-forming self-healing batteries.

Acknowledgements

This work was supported by the U. S. Department of Energy Office of Energy Efficiency and Renewable Energy under the Advanced Battery Materials Research program, award DE-EE0007785. Alyson Abraham and Mikaela Dunkin acknowledge support from the Graduate Assistance in Areas of National Need Fellowship. Bingjie Zhang thanks David Bock for helpful suggestions regarding SEM sample preparation. Esther Takeuchi acknowledges the generous support of William and Jane Knapp as the Jane Knapp Chair of Energy and the Environment.

Chapter III

Materials Approaches for Lithium Sulfur (Li-S) Batteries

Overview

This chapter will describe synthetic and fabrication strategies to generate sulfur based cathodes including MoS_2, either by direct synthetic methods (**Section 3.1**) or by electrodeposition (**Section 3.2**). Synthesis methods will explore the role of controlling "defects" in one step synthesis of tailored MoS_x nanosheets, where the nanosheets vary by layer thickness and sulfur content. The tuning of precursor ratios shows a notable difference in generated nanosheets, which in turn has demonstrated differences in subsequent cell electrochemistry, where the nanosheet type has been shown to have different behavior depending on the testing condition (rate capability or extended cycling). In **Section 3.2**, electrodeposition of a sulfur rich MoS_x is reported by two methods, noted as anodic or cathodic deposition depending on the deposition voltage. Without changing other conditions, the deposition voltage demonstrated an impact on the resultant conductivity of the observed deposition product.

3.1 Defect Control in the synthesis of 2D MoS_2 for composite electrodes in Lithium-Sulfur Batteries

Copyright (2019) © Wiley. Used with permission from :

Abraham, A., Wang, L., Quilty, C. D., Lutz, D. M., McCarthy, A. H., Tang, C. R., Dunkin, M. R., Housel, L. M., Takeuchi, E. S., Marschilok, A. C., Takeuchi, K. J., Defect Control in the Synthesis of 2 D MoS_2 Nanosheets: Polysulfide Trapping in Composite Sulfur Cathodes for Li-S Batteries, *ChemSusChem***,** 12, DOI: 10.1002/cssc.201903028.

Acknowledgement of contributions

Personal contribution: Execution and organization of multi-faceted approach for generation of varied MoS_x nanosheets, contributor to original whitepaper, proposal, manuscript draft and project reporting requirements. Planning and instruction of other group members on synthesis plans, scale up methods, and organization of characterization efforts.

Acknowledgement of collaboration:

Dr. Lei Wang- Data collection and analysis of electron microscopy (TEM, HR-TEM, SEM) of nanosheet samples, development and execution of Raman data collection and analysis, analysis of AC impedance, contributions to proposal and manuscript draft. Contribution to figures on cell cycling.

Calvin D. Quilty- Synthesis development and execution, structural characterization , XRD method to determine layer thickness and interlayer spacing, XPS data collection and analysis, ICP-OES data collection and analysis, contributions to manuscript draft.

Diana M. Lutz- Nanosheet synthesis, BET measurements and summary, collection of XPS data.

Allison H. McCarthy- Coin cell construction, electrochemical testing and summaries. Contribution to figures on cell cycling.

Christopher R. Tang – Coin cell construction and electrochemical testing. Contribution to figures on cell cycling.

Mikaela R. Dunkin – Four-point probe measurements and data analysis.

Lisa M. Housel – Collection of ICP-OES data, contributions to initial white paper and proposal.

3.1.1 Introduction

An important consideration in the continued development of next-generation rechargeable power sources is the availability of the active material components that make up the majority of the battery.[105] As demands for portable power sources increase, there is increasing importance placed on addressing the fundamental challenges that limit development and commercialization of beyond Li-ion chemistries. Alternatives to lithium ion can provide high theoretical capacity (i.e. by inclusion of a Li metal anode instead of an intercalation anode). Lithium Sulfur (Li-S) has been a leading candidate in feasible alternatives to lithium ion chemistry, in part due to its high theoretical capacity and the natural abundance of sulfur.[106] One critical roadblock to Li-S battery development is polysulfide (PS) dissolution that occurs within

the cell. This is when soluble PS species shuttle back and forth between the cathode and anode. This has two main effects, where active material is lost from the cathode, and subsequent shuttling reactions that may inhibit the cell to fully charge.[107-109] Many strategies have been employed to inhibit this shutting, which have included designing the architecture of the cathode,[110] the use of gel-based sulfur cathodes,[111, 112] polymer coatings,[113] an all solid state cell design,[107] and the incorporations of other metal sulfides, including FeS_2,[114] CuS,[115] and TiS_2.[116, 117]

Molybdenum disulfide, MoS_2, is one of the leading 2D materials that is incorporated into a variety of applications[72, 118,119-131] This is due to its wide range of interesting physical and electronic properties, including high conductivity, high surface area, and a high amount of active sites. There has also been a recent utilization of MoS_2 in Li-S batteries, where MoS_2 is used to reduce the effect of the transitory PS species during electrochemical cycling.[132] Strategies for MoS_2 incorporation to address PS species in electrochemical cells can be categorized into three areas: protection from PS species by augmenting the separator, treatment of the Li-metal anode, and trapping PS species by inclusion in a composite cathode. This includes the use of MoS_2 as a coating on the separator[76, 133-137] as a protective layer on the Li metal anode[138, 139] and inclusion in a composite cathode with a carbon support, such as graphene nanosheets[126] carbon cloth,[140] or reduced graphene oxide. [141-144] Additionally, nitrogen-doped supports, such as carbon nanotubes (CNTs)[145], mesoporous carbon spheres[140] reduced graphene oxide[146] and porous carbon[72] have also been used.

Other reports in the literature have combined the MoS_2 directly with the electrode slurry, without prior growth of the MoS_2 on a carbon support. Previously, MoS_2 was included in a sulfur-based cast electrode and demonstrated superior rate capability compared to other sulfur-based cells without the MoS_2 additive.[147] The MoS_2 additive used was from a commercially obtained source, and contained micrometer sized aggregates. While this demonstrated the benefit of the addition of MoS_2 to a sulfur composite cathode in terms of rate capability and capacity retention, the morphology and physical properties of the MoS_2 additive were not modified or controlled. A separate study using a similar method of incorporation of commercially available MoS_2 or TiS_2 to electrode slurries also had a similar outcome where there were notable improvements during electrochemical cycling, including increased Sulfur

utilization and Coulombic efficiency.[148] These prior reports showed significant improvements by the incorporation of micron-scale commercially available MoS_2. The work discussed herein compliments previous studies by looking at the effects on capacity retention and rate capability with a systematic study of synthesized nanomaterials with controlled defect structures.

In addition to previously reported experimental results, Density Functional Theory (DFT) has suggested that nano MoS_2 may have additional benefits by additional exposure of binding sites that would preferentially bind PS at designated "edge sites."[149] Density functional theory (DFT) calculations and ab initio molecular dynamic simulations have also demonstrated the propensity for the (111) and (110) facets in MoS_2 to form covalent bonds with S atoms in longer-chain PS (Li_2S_8) in the presence of 1,2-dimethoxyethane (DME). The covalent bonds formed with the PS were reported to cause the dissociation into shorter-chain PS species, which could then be adsorbed.[150] Recently, a first-principles study of defective MoS_{2-x} explained mechanistically the contribution of defective MoS_{2-x} to improvements in rate capability and cycling of Li–S batteries. Sulfur-deficient MoS_{2-x} materials were reported to enhance charge densities of the other sulfur atoms on the MoS_{2-x} (001) facet, which led to increased interactions between the product and monomer molecules during discharge, including successive lithiation steps from longer-chain to shorter-chain PS.[52]

Herein, the controlled synthesis and characterization of hydrothermally prepared 2D MoS_2 nanosheets is reported. The synthesized nanosheets vary in their number of layers, hierarchical morphology, lateral size, and defect content. Complimentary characterization techniques were utilized in tandem to determine the structure, composition, and morphology of the synthesized nanosheets, which can be found in more detail in the full published work.[151] Following nanosheet generation, the varied MoS_2 nanosheet types were included in composite sulfur-MoS_2 based cathodes and subsequently fabricated into Li-S electrochemical cells. These cells were tested using an environmentally friendly glyme-based electrolyte.[152] The impact of the physical (layer thickness) properties of the nanosheets as well as the presence of excess sulfur (defect structure) on reversibility, reduction in AC impedance after cycling, and resultant capacity retention after extended cycling at a constant C-rate and rate capability testing were determined.

3.1.2 Experimental

Synthesis of MoS_2 nanosheets were generated following previous reports in the literature.[153-155] Ammonium heptamolybdate tetrahydrate [$(NH_4)_6Mo_7O_{24}\cdot 4H_2O$] was used as the Mo source, and L-cysteine ($C_3H_7NO_2S$) was used as the sulfur source. Ammonium heptamolybdate tetrahydrate and L-cysteine were dissolved in deionized H_2O and transferred to a polytetrafluoro-ethylene-lined stainless steel autoclave. The autoclave was heated for 18 h at 220 °C, followed by cooling to room temperature. The product was collected by centrifugation, followed by washes with water and then ethanol before drying. Thickness of the MoS_2 nanosheets as well as the level of defects were controlled by changing the concentration and/or the ratio of both Mo- and S-precursors. The nanosheet type, S/Mo ratio and concentrations of L-cysteine and $(NH_4)_6Mo_7O_{24}\cdot 4H_2O$ are summarized in **Table 3.1**.

Table 3.1. S/Mo ratio used in synthesis of varied MoS_2 type nanosheets

Nanosheet Type	S/Mo ratio	L-cystine (M)	$(NH_4)_6Mo_7O_{24}\cdot 4H_2O$ (M)
Thin, sulfur rich	4.28	0.86	0.029
Thin, sulfur poor	2.25	0.45	0.029
Thick, sulfur rich	5.20	0.14	0.004
Thick, sulfur poor	2.25	0.063	0.004

In summarizing the synthesis conditions, thin sheets with varying S content, and thick sheets with varying S content were generated. The utilization of separate S and Mo sources permitted these synthesis conditions. This generated MoS_x (x= 1.9 to 2.3) served as the additive to the composite electrodes. Sulfur were incorporated into CNTs by utilizing a CNT-S melt technique in which CNTs were initially oxidized in a muffle furnace at 550°C for 30 minutes. Following oxidation, the oxidized CNTs were combined with elemental sulfur in a 4:6 mass ratio (CNT:S) and then heat treated at 155°C for 12 hours. The composition of the CNT/S melts was confirmed by thermogravimetric (TGA) analysis.

Cell fabrication and Electrochemistry

Additional details on structural characterization including surface area, electron microscopy and XRD can be found in reference.[156] Electrochemical measurements were performed on electrodes with each type of MoS_x defined by the thickness of the nanosheet and the Mo/S ratio as determined by ICP-OES. These include: 3nm thick nanosheets with excess sulfur (3 nm-$MoS_{2.3}$), or deficient in sulfur (3 nm-$MoS_{1.9}$), and 5 nm thick nanosheets with excess sulfur (5 nm-$MoS_{2.2}$), or deficient in sulfur (5 nm-$MoS_{1.9}$). All electrodes had a composition of 71% CNT-S melt (4:6 CNT/S), 9% MoS_x,10% carbon black, and 10% polyvinylidene fluoride (PVDF) binder, and were cast onto aluminum foil. Coin type cells were assembled in an argon-filled glovebox with lithium foil, 1.0m lithium bis(trifluoromethanesulfonyl)imide (LiTFSI) and 0.2m $LiNO_3$ in dipropylene glycol dimethyl ether (DPGDME) electrolyte, and polypropylene separators.

Electrochemical impedance spectroscopy (EIS) was performed by using a BioLogic VSP multichannel potentiostat. Measurements were collected with a sinus amplitude of 10 mV and a frequency range of 1 MHz to 10 mHz. Data was fit by using ZView fitting soft- ware, Version 3.5d.

Cyclic voltammetry (CV) was performed by using a Biologic VSP multichannel potentiostat at a scan rate of 0.1 mV/s over a voltage range of 2.8 to 1.7 V, starting from open circuit voltage(OCV). Current values were normalized with respect to the sulfur mass of each electrode.

Cycling tests used a Maccor battery cycler. Cells were charged to 2.8 V and discharged to 1.7 V at 308C. Rates of 2C, 1C, C/2, and C/10 were used to test the rate capability of the cells. Capacity of the cells was calculated relative to the mass of the entire electrode (without the foil) and relative to the sulfur mass and electrochemistry.

3.1.3 Results and Discussion

Synthesized nanosheets were characterized by X-ray diffraction (XRD), TEM and SEM. Four distinct nanosheet types were identified, based on their nanosheet thickness, and Mo:S ratio. The four types of nanosheets were identified as 3nm-$MoS_{1.9}$, 3nm-$MoS_{2.3,}$ 5nm-$MoS_{1.9}$ and 5nm-$MoS_{2.2}$. Overall, both of the 3nm nanosheet varieties showed more curvature and had a

smaller lateral size when compared to the 5nm nanosheet types. Both of the 5nm nanosheet types (5nm-$MoS_{1.9}$ and 5nm-$MoS_{2.2}$) exhibited larger assemblies of flower-like spheres that were made up of the individual nanosheets. HR-TEM was able to resolve the structural details of the structures by observing the relative crystallinity and determining the nanosheet layer thickness as well as the range of layers that made up a typical nanosheet bundle. A comparison of the relative nanosheet thicknesses are shown in **Table 3.2**. The 5nm-$MoS_{1.9}$ had the largest nanosheet thickness (6.0 ± 1.2 nm) as well as the greatest number of layers, which ranged from 5-10. This can be compared to the other 5nm-$MoS_{2.2}$ which had an average nanosheet thickness of (4.0 ± 0.7 nm) and an average layer range of 5-8 layers. It was observed that the defects introduced by a stoichiometric excess of sulfur acted to decrease the number of layers, which was accompanied by an excess of interlayer spacing. In addition to providing quantitative information on layer thickness and layer number, HR-TEM also provided evidence of dislocations and distortions in the basal plane of the nanosheets. This was especially noted in the sulfur rich nanosheet types, 3nm-$MoS_{2.3}$ and 5nm-$MoS_{2.2}$, in which the defect rich structure was attributed to the abundance of unsaturated sulfur atoms. The introduction of defects and distortions can affect the electronic properties and subsequently affect the stability of the nanosheets by generating a decrease in the surface energy[157] or by serving as trapping sites to bind polysulfide species that are formed during discharge.

Table 3.2. Thickness, number of layers and interlayer spacing of the MoS_2 nanosheet types.

Material	Thickness (nm)	Number of layers	Interlayer spacing [Å]
3nm-$MoS_{1.9}$	3.3 ± 0.4	3-6	6.2 ± 0.9
3nm-$MoS_{2.3}$	3.1 ± 0.5	3-4	6.6 ± 0.9
5nm-$MoS_{1.9}$	6.0 ± 1.2	5-10	6.3 ± 0.7
5nm-$MoS_{2.2}$	4.0 ± 0.7	5-8	6.6 ± 0.7

All four nanosheet types exhibited low crystallinity, which was confirmed by both the observation of multiple lattice fringes in HR-TEM images as well as by the observation of broad peaks observed in X-ray diffraction patterns. While few broad peaks were observed in the synthesized MoS_2 nanosheets, the peak pattern corresponded to the powder pattern of MoS_2, corresponding to PDF card #01-071-9809. No impurity peaks were detected in any of the generated materials. Additional characterization was used to compare the relative surface areas to determine correlation of surface area properties to subsequent cycling behavior. This included BET measurements to correlate surface area measurements to observed morphology in SEM images. BET measurements are summarized in **Table 3.3**. The low surface area measurements were consistent with observations in microscopy images. Additional characterization of the nanosheets included Raman spectroscopy which provided information on the molecular properties of the synthesized nanosheets which can be correlated to crystallinity and information on defects. Two distinct Raman modes were identified for the MoS_2 nanosheets, showing an in-plane vibration, correlating to the S and Mo, and an out of plane vibration correlating to S.[158] Crystallinity of the samples of the nanosheet samples can be qualitatively evaluated by Raman, where the crystallinity can be evaluated by the broadness of the observed peaks.[159] The broad peak associated with the A_{1g} band correlating the out-of-plane vibration of the S atoms, was observed for all of the MoS_2 nanosheet samples.

Table 3.3. BET measured surface area of MoS_2 nanosheet types.

Material	Surface Area ($m^2 g^{-1}$)
3nm-$MoS_{1.9}$	51
3nm-$MoS_{2.3}$	34
5nm-$MoS_{1.9}$	26
5nm-$MoS_{2.2}$	5

In addition to Raman, additional characterization included conductivity of the MoS_2 nanosheets as well as a comparison of XPS and ICP obtained stoichiometries of the nanosheets. XPS provided information into the relative peak areas associated with Mo and S species observed on the surface, including the Mo 3d and S 2p regions. It was determined that the sulfur

rich MoS_2 synthesized nanosheets contained a combination of both MoS_2 and MoS_3, with the dominant species being MoS_2 (Mo^{4+} oxidation state), as noted by comparing the ratios of the Mo^{4+} and Mo^{6+} peak areas. To evaluate the difference in the surface composition to the bulk composition of the MoS_2 nanosheets, the stoichiometry was determined both by XPS based on the ratio of Mo 3d peaks to the S 2p peaks, and ICP-OES. In all cases, the XPS-determined stoichiometry was significantly higher than that determined by ICP OES, ranging from 0.44 to 0.48 additional S content for the 3nm nanosheet series, and 0.42 to 0.45 S content for the 5nm nanosheets. This suggested that all samples contained sulfur rich surfaces. A comparison of the stoichiometries obtained by XPS and ICP-OES is shown in **Table 3.4.**

Table 3.4. Stoichiometries of MoS_x materials, based on XPS and ICP-OES.

	Stoichiometry	
Material	**XPS**	**ICP-OES**
3nm-$MoS_{1.9}$	$MoS_{2.41}$	$MoS_{1.93}$
3nm-$MoS_{2.3}$	$MoS_{2.70}$	$MoS_{2.26}$
5nm-$MoS_{1.9}$	$MoS_{2.36}$	$MoS_{1.91}$
5nm-$MoS_{2.2}$	$MoS_{2.57}$	$MoS_{2.15}$

To compare the relative conductivity of the MoS_x nanosheets, four point probe measurement was conducted. Measurements of pressed pellets consisting only MoS_2 nanosheets were compared to each other, and to prior literature measurements of various MoS_2 nanosheets. The 5nm-$MoS_{2.2}$ nanosheet demonstrated the highest conductivity, amongst the four nanosheet types tested. This was consistent with prior literature results that showed a relationship between increasing MoS_2 nanosheet thickness and increase in conductivity, where materials ranging in thickness from 0.6 to 4.6 μm (prepared by electrochemical exfoliation) showed an increase in conductivity from 4 to 17 S/cm.[160] A comparison of the relative conductivities measured by four-point probe is shown in **Table 3.5**.

Table 3.5. Conductivities of MoS_x materials based on four-point probe measurements.

Material	Conductivity (S/cm)
3nm-$MoS_{1.9}$	3.41 x 10^{-3}
3nm-$MoS_{2.3}$	1.02 x 10^{-3}
5nm-$MoS_{1.9}$	8.13 x 10^{-1}
5nm-$MoS_{2.2}$	1.87 x 10^{-2}

Electrochemistry

The 3 nm-$MoS_{1.9}$, 3 nm-$MoS_{2.3}$, 5 nm-$MoS_{1.9}$, and 5 nm-$MoS_{2.2}$ nanosheets were included as an additive in the preparation of composite sulfur-based cathodes. Subsequent electrochemistry, including cyclic voltammetry (CV), rate capability tests, extended cycling, and electrochemical impedance spectroscopy (EIS) were performed. During CV tests, two distinct reduction peaks were observed in the cathodic scan at approximately 2.0 and 2.4 V for all cell

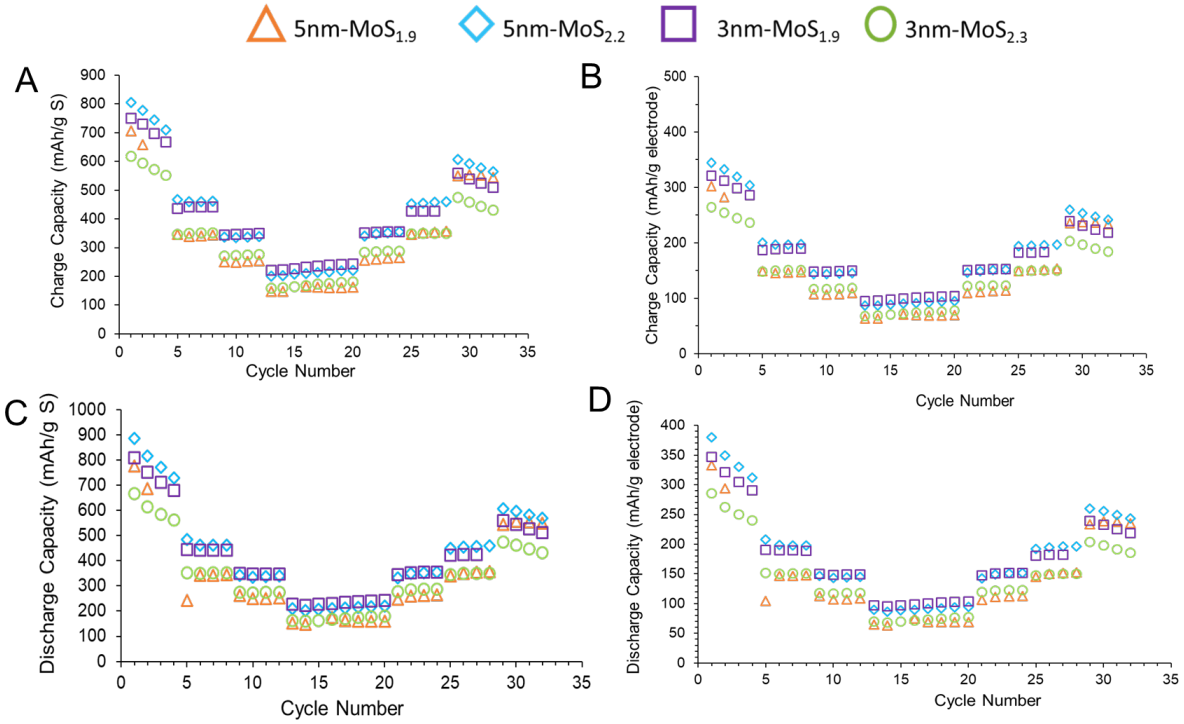

Figure 3.1. Rate capability tests at C/10, C/2, 1C, 2C, 1C, C/2, C/10 of A) 5nm-$MoS_{1.9}$, B) 5nm-$MoS_{2.2}$, C) 3nm-$MoS_{1.9}$, D), 3nm-$MoS_{2.3}$.

types. This was attributed to the formation of long chain (i.e. Li_2S_8, Li_2S_6, Li_2S_4) and short-chain (i.e. Li_2S_2, Li_2S) polysulfides, which is in agreement with previously reported peaks that were observed in systems using ether-based electrolyte.[155] Oxidation was observed between a voltage range of 2.3 to 2.5V, corresponding to the conversion of Li_2S_2 or Li_2S into soluble lithium polysulfides and elemental sulfur.[161]

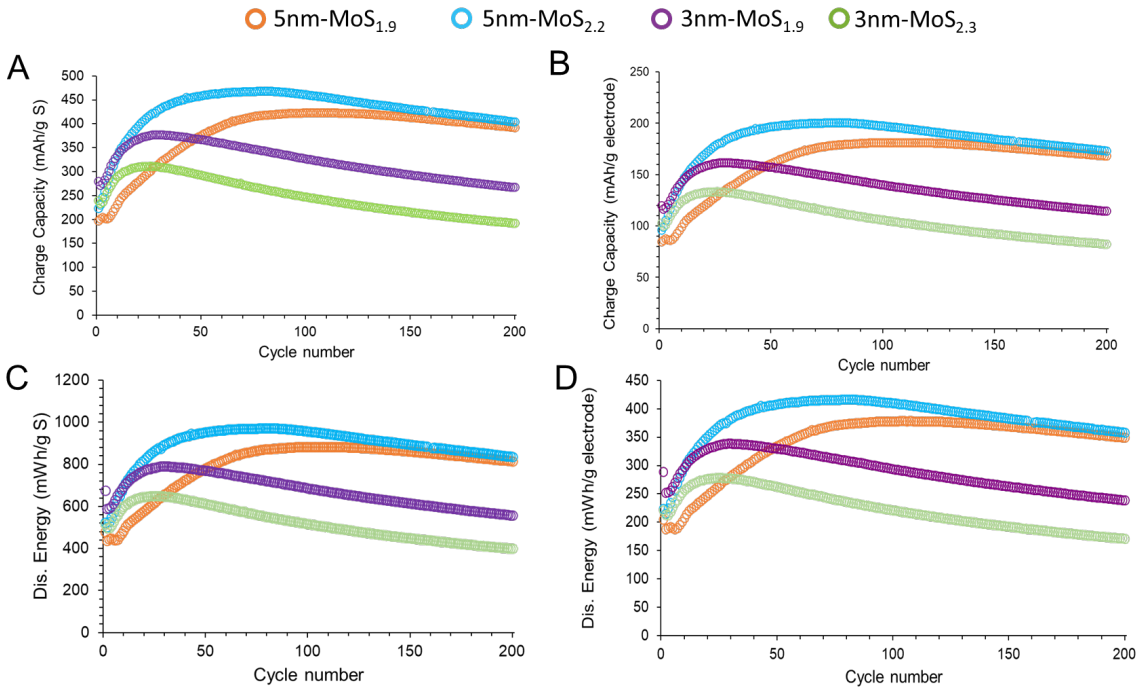

Figure 3.2. 200 discharge-charge cycles at C/2 for all nanosheet types. **A)** Charge capacity per mass Sulfur, B) Charge capacity per mass of electrode, C) Discharge Energy per mass Sulfur, D) Discharge energy per mass electrode.

Cycling tests were initially conducted using rate capability testing with four cycles at the following C-rates: C/10, C/2, 1C, followed by eight cycles at 2C, then four cycles at 1C, C/2, C/10 as shown in **Figure 3.1**. Interestingly, the 5 nm-$MoS_{2.2}$ maintained the highest capacity upon cycling at increasing (dis)charge rates, despite having a much lower surface area when compared to the other nanosheet types. This is an indication that a high surface area of the MoS_2 additive is not a major contributor to high rate capability in composite electrode testing. To evaluate the cells in terms of cycling stability, extended cycling tests were conducted for 200 cycles at a C/2 rate for each cell type, as shown in **Figure 3.2**. Both of the thicker nanosheet

types, 5 nm-$MoS_{2.2}$ and 5 nm-$MoS_{1.9}$ nanosheet containing cells had a higher retention of charge capacity (404 and 393 mAh per g sulfur, respectively) compared to the 3 nm-$MoS_{1.9}$ and $MoS_{2.3}$ cells (192 and 267 $mAhg^{-1}$, respectively). This notable drop in capacity could be correlated to the nanosheet thickness as well as to electrical conductivity. Another interesting observation was the contrast between the 3 nm- and 5 nm- nanosheet types of the same sulfur composition, $MoS_{1.9.}$ The 5 nm-$MoS_{1.9}$ had a near doubling of its charge capacity (from 201 to 393 $mAhg^{-1}$) between the first to 200th cycling. In contrast, both of the thinner, 3 nm nanosheet types (3 nm-$MoS_{1.9}$ and 3 nm-$MoS_{2.3}$) observed a gradual decline during extended cycling.

3.1.4 Conclusions

Synthetic control of MoS_2 nanosheets with varied sheet thickness and defects was demonstrated by generating two types of MoS_2 layer thicknesses (3 and 5 nm), as well as two varieties of bulk stoichiometry; $MoS_{1.9}$ and MoS_{2+x} (x = 0.3 for 3 nm and 0.2 for 5 nm nanosheets). To distinguish the relationship between defected nanosheets and physical characteristics, several overall trends were observed. Thickness of the nanosheets showed a direct impact on the overall morphology, where the thicker (5 nm) nanosheets had a flower like structure, and the thinner (3 nm) sheets had a smaller lateral size and were less compact. There was a general trend of the 5 nm nanosheets to aggregate, where less aggregation was observed in the 3 nm sheet types. Interlayer spacing of both nanosheet types was observed with increasing sulfur content (above MoS_2). An increase in sulfur content also generated nanosheets that had a greater content of dislocation and distortion compared to the $MoS_{1.9}$ nanosheets of both thickness types (3 nm and 5 nm). Surface area measurements showed a larger surface area for the 3 nm-$MoS_{1.9}$ and -$MoS_{2.3}$ nanosheets, which was attributed to the reduced agglomeration observed in these nanosheet types. XPS and ICP-OES measurements provided a comparison on the difference in sulfur distribution between the surface (XPS) and bulk (ICP-OES), where XPS measurements denoted a more sulfur-rich surface for all of the MoS_x nanosheet types. This implies that because the surface of all synthesized materials is sulfur rich, other factors, such as layer thickness and morphology, may have more impact than tuning of the sulfur ratio. Future studies may build upon this framework by normalizing to Mo content, while extending the variations in layer thickness, then can further address variation in sulfur content.

Upon electrochemical testing, there was a notable difference in the capacity retention in relation to cycling conditions. During rate capability testing, the 3 nm-$MoS_{1.9}$ and 5 nm-$MoS_{2.2}$ had similar capacity retention, whereas there was a notable difference between the 3 and 5 nm nanosheets during extended cycling at a constant (C/2) rate. Nominal increases in nanosheet thickness from 3 to 5 nm increased the capacity retention after extended cycling, regardless of sulfur content (MoSx, x < or > 2). When excess sulfur was included in the 5 nm nanosheet type (5 nm-$MoS_{2.2}$), the nanosheet additive enhanced capacity retention both in rate capability and extended cycling tests. Interestingly, the 3 nm-$MoS_{2.3}$ nanosheet type had the poorest capacity retention compared with all nanosheet types, indicating that the contribution may stem from the nanosheet thickness and subsequent morphological considerations as opposed to increases in sulfur content. Additionally, there was an interesting correlation between surface area of the synthesized nanosheets and resultant cycling tests. The 5 nm-$MoS_{2.2}$ material that was noted to have both the highest capacity retention in rate capability and extended cycling tests had a surface area which was approximately seven times lower than the surface area determined for the material with the worse capacity retention during extended cycling (3nm- $MoS_{2.3}$). These findings highlight the importance of synthetic control and morphological tuning of material additives, as notable differences in both short-term and long-term cycling were observed by a modest inclusion (9% of the electrode) of the synthesized MoS_2 nanosheets.

Acknowledgements

The materials synthesis and electrochemistry investigations were funded by the U.S. Department of Energy Office of Energy Efficiency and Renewable Energy, under award DE-EE0008208. Atomic level defect characterization, specifically Raman spectroscopy and high-resolution electron microscopy, were supported as part of the Center for Mesoscale Transport Properties, an Energy Frontier Research Center supported by the U.S. Department of Energy, Office of Science, Basic Energy Sciences, under award #DE-SC0012673. Experimental research characterizations were carried out in part at the Center for Functional Nanomaterials, Brookhaven National Laboratory, an Office of Science User Facility, which is supported by the U.S. Department of Energy, Office of Basic Energy Sciences, under Contract No. DE-SC0012704. We also acknowledge the Advanced Energy Research and Technology Center for access to the ThINC facility. D.M.L. and C.R.T. acknowledge support from the NSF GRF

#1839287. A.H.M. and M.R.D. acknowledge support from the Graduate Assistance in Areas of National Need (GAANN) Fellowship sponsored by the U.S. Department of Education. E.S.T. acknowledges the William and Jane Knapp Chair in Energy and the Environment.

3.2 Tunable Fabrication of Sulfur Equivalent Electrodes for High Capacity or High Power

The following is adapted from the following open access article distributed under the terms of the Creative Commons Attribution 4.0 License, permitting the unrestricted used of the work in any medium, provided citation:

Electrodeposition of MoS_x: Tunable Fabrication of Sulfur Equivalent Electrodes for High Capacity or High Power, Wu, Q., Abraham, A., Wang, L., Tong, X., Takeuchi, E. S., Takeuchi, K. J., Marschilok, A. C., *J. Electrochem. Soc.,* 2020, 167, 050513.

Acknowledgement of contributions:

Personal contribution: Generation of electrodeposited materials for testing, collection and analysis of data on charge passed as a function of deposition time, data collection and analysis of AC-SECM maps over both sample types, plotting of extended cycling data, contributed to manuscript preparation and additional analysis of literature.

Collaborator contributions:

Dr. Qiyuan Wu: Determination of electrodeposition conditions, SEM characterization, EQCM data collection and analysis, ICP-OES data collection, DC SECM data collection and analysis, electrochemical cycling, XPS data collection and analysis, AFM and manuscript preparation.

Dr. Lei Wang: Raman analysis of MoS_x samples, contributions to manuscript.

Dr. Xiao Tong: XPS data collection and instrumentation (Center for Functional Nanomaterials, Brookhaven National Laboratory).

3.2.1 Introduction

As the demand for next-generation batteries with high energy/power density and long cycle life continues to grow, lithium sulfur batteries (LSBs) are considered a promising candidate due to the large theoretical capacity and low cost of sulfur.[162-164] As noted in the previous section, challenges, including formation of intermediate polysulfide species that are highly soluble in organic solvents can lead to observed capacity degradation after continued cycling.

This chapter will report on electrodeposited MoS_x and the effect of deposition conditions on the subsequent electrochemistry.

In the literature, there have been recent reports describing the implementation of "sulfur-equivalent cathode materials" where the use of elemental sulfur is replaced by other sulfur-containing materials.[165-169] In the MoS_x cathode system, an interesting observation was that no Li_2S or other polysulfides have been detected as reaction intermediates, or in final products[167] which may avoid issues with polysulfide shuttling reactions that are commonly observed in Li-S batteries with an elemental sulfur based cathode. In addition to potentially avoiding polysulfide shuttling effects, the MoS_x based systems can be cycled in carbonate based electrolytes, whereas conventional LSBs are completely non-cyclable in the carbonate electrolyte. [167, 169] The ability to use carbonate based electrolyte instead of ether based electrolyte enables a higher thermal stability range, and is also lower cost.[167] Sulfur equivalent cathodes with amorphous molybdenum polysulfide (MoS_x, $x \geq 2$**)** have reported both high capacities and high capacity retention.[166, 167, 169] An example of this is in the $MoS_{3.4}$ cathode system, where $MoS_{3.4}$ has delivered 578 mAh/g and retained 60% capacity after 30 cycles, where the redox active species was sulfur and the oxidation state of Mo remained unchanged during charge/discharge via X-ray spectroscopy (XPS) and operando pair distribution function techniques (PDF).[169] Additionally, with a higher stoichiometric excess of sulfur, $MoS_{5.7}$ reported a 800 mAh/g capacity with a 70% capacity retention after 100 cycles. This report noted a conversion reaction, where both Mo and S were seen as being electrochemically active, as shown by x-ray absorption spectroscopy (XAS).[166] Another report using a MoS_3/CNT composite cathode demonstrated a 70% retention of the 500 mAh/g capacity after 1000 cycles, where, similar to the above reference, both of the Mo metal and S centers were shown to be electrochemically active shown by operando XAS measurements.[167] These prior studies utilized MoS_x materials that have been prepared via chemical synthesis methods, then the synthesized product was physically combined with other electrode components to create the composite electrode heterostructure. While these composite electrodes have demonstrated high capacity and capacity retention after cycling, the complex multi-step preparation challenges of generating these composite electrodes may lead to increased manufacturing costs and present challenges in scaling.

Electrodeposition has been employed as a low-cost and scalable technique for preparation of a wide range of devices, including large area solar panels or displays.[170, 171] Electrodeposition allows for quantitative control in depositing phase pure alloys[172] and metals.[173, 174] To expand on electrodeposition of pure metals, crystalline oxides can be prepared by tuning deposition conditions or post treatments for oxidation[175-177] and the substrate selection can affect the deposited film properties, such as porosity, by implementing a carbon nanotube (CNT) substrate.[178, 179] While it has been demonstrated that MoS_x films can be electrodeposited from a solution of ammonium tetrathiomolybdate, $(NH_4)_2MoS_4$ under different deposition conditions[180-183], the subsequent electrochemistry of these electrodeposited MoS_x films has been unexplored.

This section discusses a flexible and facile one-step electrochemical deposition method of MoS_x-carbon composite electrodes for lithium based batteries. Detailed characterization showed that both the physical and chemical properties of the MoS_x are controlled by the deposition parameters. The difference in the physical and chemical properties from the different deposition conditions led to notable differences in the subsequent electrochemical testing which could be correlated to the materials' properties. The results of this study could provide new insight into strategies for fabrication of next-generation electrode materials.

3.2.2 Experimental

The deposition of MoS_x was performed on 25 **µm** thick conductive graphene sheets (Graphene Supermarket®) using a traditional three-electrode configuration. An Ag/AgCl standard electrode was used as the reference electrode and a Pt wire was used as the counter electrode. A 2 mM $(NH_4)_2MoS_4$ in 0.1 M Na_2SO_4 aqueous solution was used as the deposition solution. Before the constant potential deposition, a CV scan was performed. Anodic deposition (sample denoted as MoS_x-AD) was conducted at 0 V vs the Ag/AgCl reference, and cathodic deposition (sample denoted as MoS_x-CD) was conducted at -0.9 V vs the Ag/AgCl reference.

Scanning Electrochemical Microscopy (SECM) approach curves were measured using a commercial SECM instrument (CHI 920C, CH Instruments). An ultramicroelectrode (UME) with radius a = 5 µm (CHI 116, CH Instruments) was used as the working electrode, with an Ag/AgCl standard electrode and Pt wire as the reference and counter electrodes, respectively. The approach curves were conducted in 1 mM ferrocenemethanol in 0.1 M potassium chloride aqueous solution.

Alternative current scanning electrochemical microscopy (AC-SECM) was performed using a commercial SECM instrument (M470, BioLogic). A UME with a radius a = 5 μm (BioLogic,) was used as the working electrode, with a screen printed Ag/AgCl reference (BioLogic) and Pt wire counter. Water with conductivity of ~ 0.06 μS/cm^2 was used as the electrolyte. The initial probe approach used AC-SECM with intermittent contact (-ic) control with a piezo AC vibration of 455 Hz. Area scans (AC-SECM) were obtained ~ 100 microns above the sample, over a 240 by 240 μm area with a 20 μm scan step, yielding a total of 169 measurements for each sample. The bias conditions used a 0V (vs. open circuit potential) DC-bias, 100mV AC-bias, and 50kHz AC-frequency. Additional experimental details on Scanning Electron Microscopy (SEM), Atomic Force Microscopy (AFM), Raman spectroscopy, and electrochemistry and cycling tests, can be found in the full literature report.

3.2.3 Results and Discussion

Electrochemical Deposition.

To initially test for deposition conditions, an aqueous solution containing $(NH_4)_2MoS_4$ and Na_2SO_4 as the supporting electrolyte showed distinct oxidation and reduction peaks after several cycles when the potential of a conductive working electrode was cycled from 1.0 to -0.1 V vs Ag/AgCl. The oxidation peak was observed at -0.2V, and a reduction peak at -0.8V. The increase in current in over 10 cycles at both of these peaks, suggested that two possible potentials could be selected for deposition conditions. Following a literature report[184], two suggested deposition pathways were proposed, anodic deposition (-0.3V to 0.1 V), and cathodic deposition (-0.8V to -1.0V). The proposed reactions for each are outlined below in **Equation 3.2-1 and 3.2-2:**

Anodic deposition (-0.3 V to 0.1 V):

$$[\mathrm{MoS_4}]^{2-} \rightarrow MoS_3 + \frac{1}{8}S_8 + 2e^- \qquad \textit{Equation 3.2-1}$$

Cathodic deposition (-0.8 V to -1.0 V):

$$[\mathrm{MoS_4}]^{2-} + 2H_2O + 2e^- \rightarrow MoS_2 + 2SH^- + 2OH^- \qquad \textit{Equation 3.2-2}$$

To achieve more efficient deposition conditions, a constant potential hold was utilized following the initial cyclic voltammetry test. Two potentials were chosen to correspond to the range for anodic deposition (0 V) and cathodic deposition (-0.9 V). Herein, these deposition conditions will be referred to MoS_x-AD and MoS_x-CD for anodic and cathodic deposition, respectively. Deposition was initially conducted at a constant potential utilizing an electrochemical quartz crystal microbalance (EQCM) to determine the relationship of current and mass change over deposition time. **Figure 3.3 a, b** shows the deposition current versus time for the anodic MoS_x-AD at 0 V and cathodic MoS_x-CD at -0.9 V deposition conditions. While the current response was non-linear, the mass change as a function of time during deposition increased in both deposition conditions, noting validation of the selection experimental conditions. Plots showing the mass change versus time can be found in the full report.

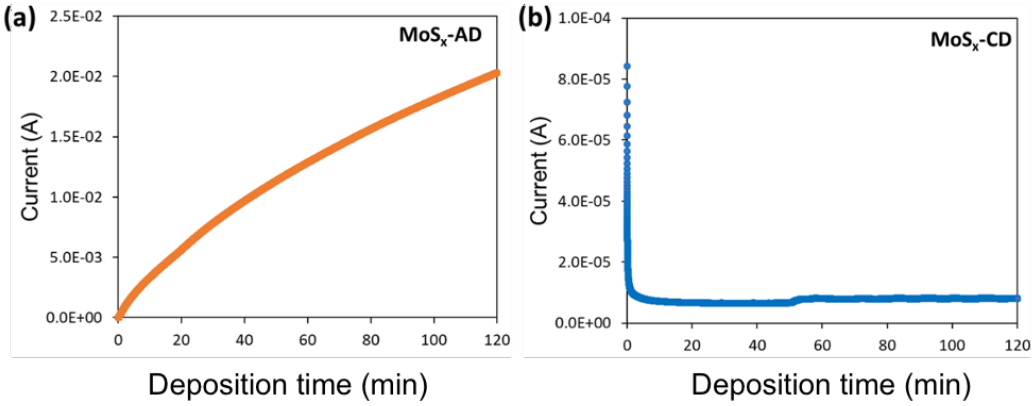

Figure 3.3. EQCM MoSx constant potential deposition on gold coated quartz single crystal. (a, b) Current versus time plots for (a) Anodic deposition (MoSx-AD) at 0V vs Ag/AgCl, (b) Cathodic deposition at -0.9 V vs Ag/AgCl.

The deposition of MoS_x films was investigated on commercially available conductive graphene sheets where the deposited samples were configured to be directly used as electrodes, as shown in **Figure 3.4.** The deposited MoS_x films uniformly cover a 10 cm^2 area of the graphene substrate demonstrating the capability of electrodeposition to produce large-scale electrodes.

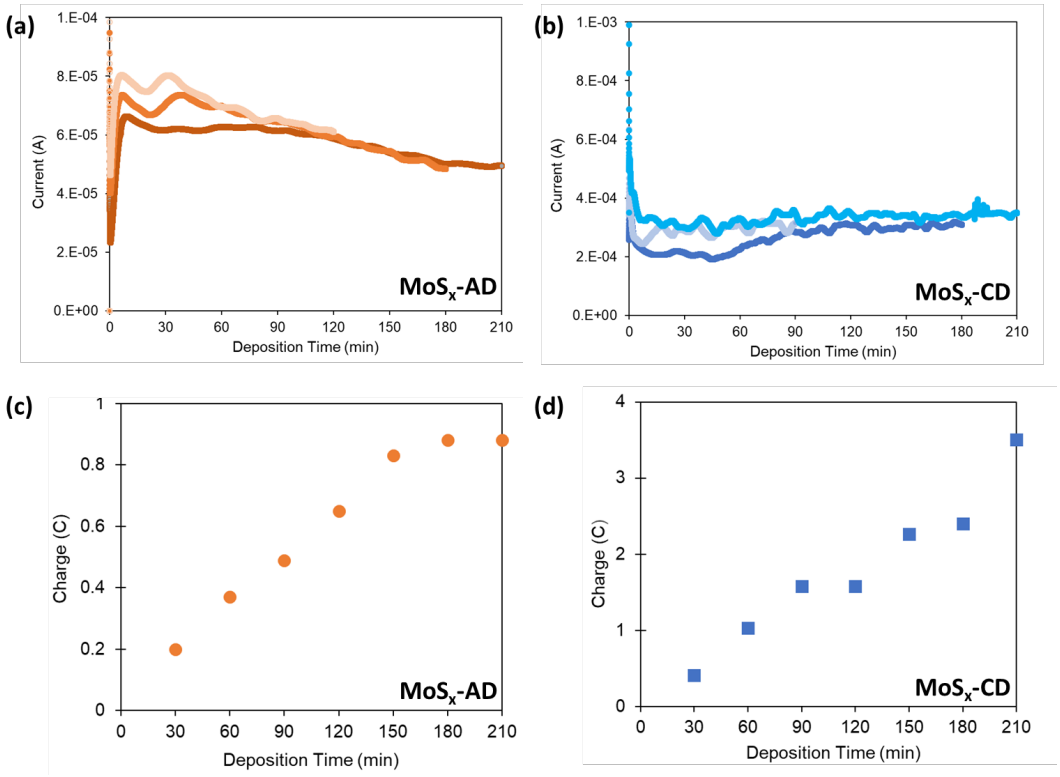

Figure 3.4. MoS_x deposition on graphene sheet for varying time intervals. (a, b) Current versus time plots for (a) Anodic deposition (MoS_x-AD) at 0 V vs Ag/AgCl, (b) Cathodic deposition at -0.9 V vs Ag/AgCl. (c,d) Total charge passed for various time intervals of (c) MoS_x-AD and (d) MoS_x-CD depositions.

Film Characterization

Details on film characterization of the deposited MoS_x-AD and MoS_x-CD can be found in the full literature report, where SEM, Raman, and AFM are discussed in detail. Briefly, deposited films of each deposition condition (MoS_x-AD, MoS_x-CD) were initially characterized by Scanning Electron Microscopy (SEM) and Energy Dispersive Spectroscopy (SEM-EDS). In both samples, the elemental maps of Mo and S obtained by EDS showed uniformity of Mo and S dispersed throughout the electrode, rather than films consisting of segregated islands or species of Mo and S. Following Equation 3.2-1**,** it was expected to have two types of sulfur (S) species, where one species would come from the molybdenum sulfide and the other from elemental sulfur, however based on observations from EDS mapping, the sulfur species that existed were

distributed evenly amongst the deposited Mo. In both samples, there were cracks observed between the MoS_x domains, that were shown to be the carbon substrate, which was visible in the C maps obtained by EDS. High-resolution SEM obtained of both samples showed that the large domains of MoS_x were made up of mainly smaller, irregularly shaped particles. For additional analysis of the chemical composition of the surface, XPS was obtained on both the MoS_x-AD, and MoS_x-CD samples. XPS fitting confirmed the presence of three different S species in the MoS_x-AD samples, whose energies correlated with those of elemental S(0), bridging S_2^{2-} and terminal S^{2-}.[184, 185] In comparison, the MoS_x-CD sample was fit with regions corresponding only to S_2^{2-} and S^{2-} species, with no presence of elemental sulfur. One point of note is the difference between the MoS_x-CD and those of bulk MoS_2 crystals. By ICP-OES the S/Mo ratios were determined, where the S/Mo ratio for the MoS_x-AD sample was 3.9 : 1, and the S/Mo ratio for the MoS_x-CD sample was 1.8 : 1.[184, 186, 187] Raman spectroscopy additionally demonstrated the difference of the near stoichiometric MoS_x-CD to bulk MoS_2 crystals, where an increase in bandwidths of the E^1_{2g} and the A_{1g} peaks was observed in both of the MoS_x samples, but was especially noticeable for the MoS_x-CD sample. Detailed Raman analysis and comparisons to XPS data can be found in the full literature report. A notable observation from Raman analysis was the presence of more oxygenated species in the MoS_x-CD sample.

To evaluate the surface properties of the electrodeposited MoS_x films, several approaches were utilized to provide insight into electronic and morphological features. Herein, specifically the approaches utilizing Scanning Electrochemical Microscopy (SECM) will be discussed. SECM was utilized to characterize the local electrochemical properties of the deposited films by approaching and/or scanning a ultramicroelectrode tip above the surface of a sample or substrate in a solution.[188] The general set-up of SECM is shown in **Figure 3.5**. This set up includes at least one working electrode ("1" in **Figure 3.5**), a counter electrode, reference electrode, and substrate. The substrate can be connected as a second working electrode ("2" in **Figure 3.5**), where a potential can be applied directly to the substrate. The substrate is seated inside a small containing area that is filled with a supporting electrolyte (and a redox mediator in the case of DC SECM). The probe can either be approached to the surface, where the current at the probe is monitored as a function of travel distance, or by scanning an area in the x-y plane across an area of the substrate.

Approach curves, used in direct current (DC) mode, provide insight into the overall conductivity of the substrate.[189] Approach curves utilize a ultramicroelectrode with an exposed Pt surface, that gradually approaches a substrate in a controlled fashion (by a combination of stepper and/or piezo control) along the z-axis. In DC-SECM, a redox mediator, which is added to the solution, undergoes a redox reaction by driving electrochemical reaction of a redox species (e.g. oxidation of ferrocenemethanol, $C_{11}H_{12}FeO$ or FcMeOH) over the ultramicroelectrode tip and measures the current as a function of the position of the scanning tip. **Figure 3.6** shows a schematic of the probe approaching a conductive surface when A) the probe is far away from the substrate, and the redox reaction is governed by steady state, and B) and increase in probe current above the stead state current, when the probe in near a conductive substrate by continuous redox reaction occurring at the probe's surface (inset). In this manner, SECM approach curves reflect the conducting or insulating nature of the substrate materials electrochemically.[190-193]

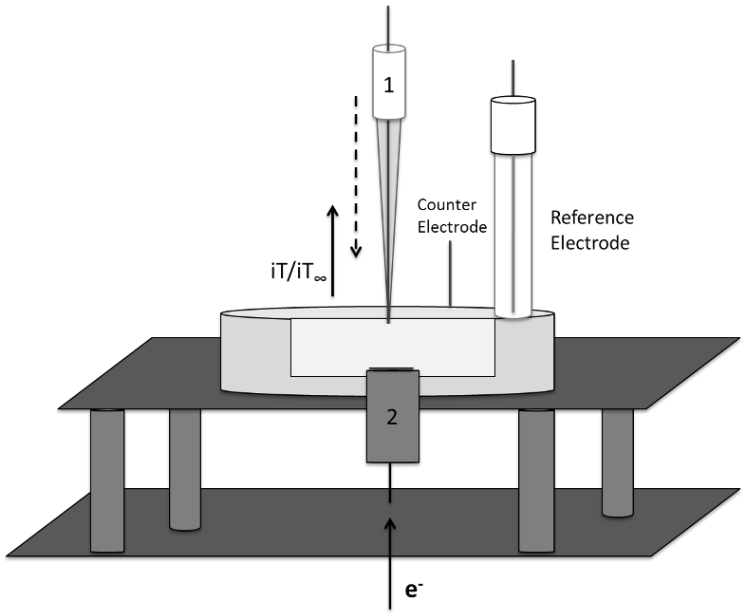

Figure 3.5. Schematic of SECM setup including the probe (working electrode 1), the substrate (which can act as working electrode 2), a reference electrode, counter electrode, and electrochemical cell to hold the electrolyte.

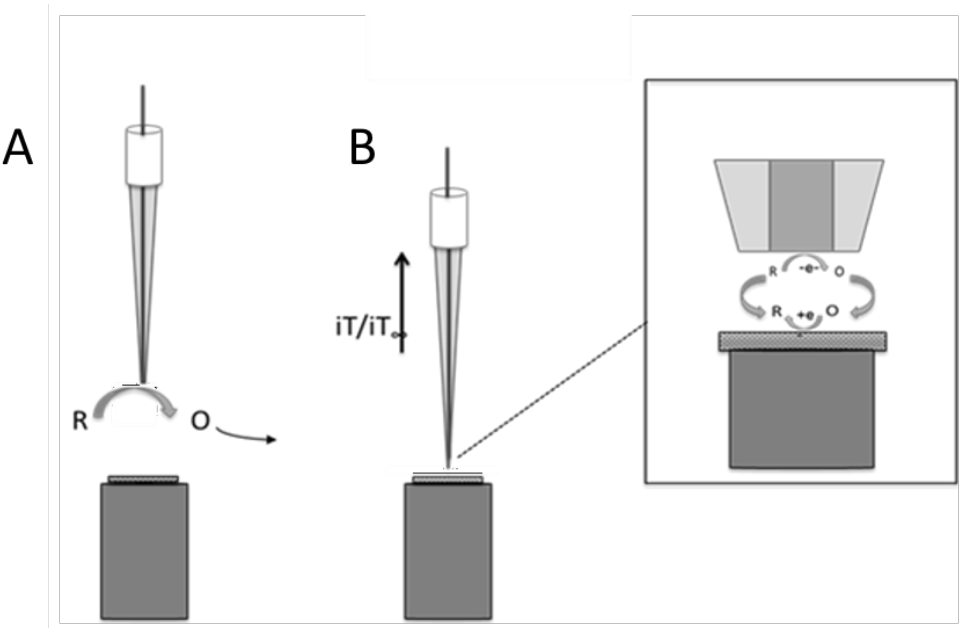

Figure 3.6. A) Probe approach towards substrate, where probe current is defined by steady state behavior of redox couple, B) Probe near surface of conductive substrate where continuous redox generation increases probe current above steady state.

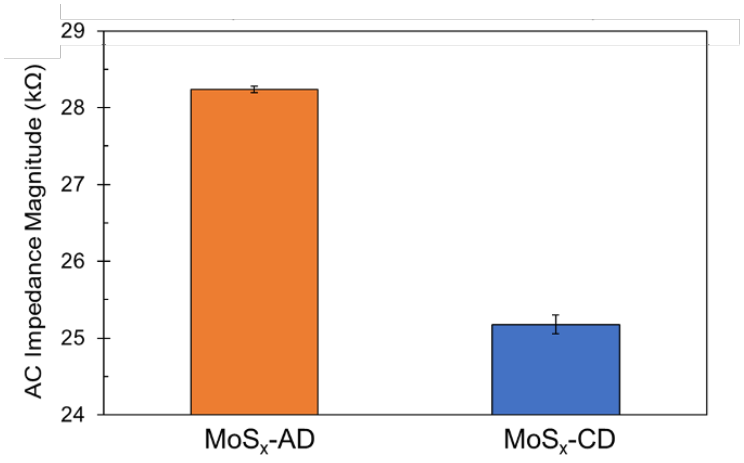

Figure 3.7. Comparison of AC-SECM impedance magnitude over 240 x 240 µm area of MoS_x-AD and MoS_x-CD.

To compliment the DC SECM measurements, and to isolate any effects that could be obscured by the use of a redox mediator, alternating current scanning electrochemical microscopy (AC-SECM) measurements were obtained on 240 x 240 μm areas on both of the MoS_x-AD and MoS_x-CD samples. The benefit of incorporating the AC based technique, is that the samples can be mapped in a low conductivity electrolyte (such as water) without the addition of a redox mediator.[194, 195] AC-SECM can be used both to provide topographic information on the sample, or local surface properties, such as impedance magnitude. Mapping of AC-impedance magnitude of flat samples at the same probe-substrate distance can provide insight into the relative measured impedance over a sample area. DC-SECM approach curves showed decreasing normalized current as the probe approaches the MoS_x-AD sample, where an increase in normalized current is observed in the MoS_x-CD sample as the probe approaches the sample surface. The decrease in current observed with the approach to the MoS_x-AD sample corresponds to more insulating behavior, whereas the increase in current upon approach observed with MoS_x-CD sample corresponds to more conductive behavior.

To compare the relative AC impedance maps of the areas of both of the sample types, AC-SECM maps were obtained as shown in **Figure 3.7.** The AC-SECM maps should trends that were analogous in comparing the impedance magnitude, where the averaged AC- impedance magnitude of the MoS_x-AD sample was great than that of the MoS_x-CD sample (28.2 ± 0.1 k**Ω** compared to 25.2 ± 0.1 k**Ω**, respectively). Additional experiments to support the difference in electrical conductivity included Atomic Force Microscopy using local current voltage (I-V) mode. The current was tracked over the domain between the MoS_x and graphene boundary. In the MoS_x-AD sample, there was a notable increase in current over the area corresponding to the graphene substrate, whereas in the MoS_x-CD sample, the current was high both over the MoS_x substrate domain and the exposed graphene crack. These results additionally supported the SECM conclusions that denoted the MoS_x-CD sample as being more electrically conductive.

Film Electrochemistry

Both samples showed distinct behavior from crystalline MoS_2 yielding higher discharge capacities even under higher current.[167, 196] The MoS_x-AD sample shows a high initial capacity of 900 mAh/g. On the other hand, the MoS_x-CD sample showed an initial capacity of 500 mAh/g. It is worth noting that when the capacity is normalized to sulfur content, the MoSx-AD

would show a high capacity of 1600 mAh/g, and MoSx-CD would have a capacity of 1300 mAh/g making them good candidate for "sulfur-equivalent cathode materials". Differences in rate capability are shown in **Figure 3.8A**, while comparison of extended cycling is shown in **Figure 3.8B**. In comparing Furthermore, even the MoS_x-CD sample which has lower capacity showed comparable capacity to previously reported values of low crystallinity MoS_x-based cathodes.[167, 169] Rate capability is a critical issue in LSBs due to insulating nature of sulfur[162, 164] In rate capability testing, the capacity of MoS_x-AD showed a notable decrease from 900 mAh/g to only 20 mAh/g. In contrast, MoS_x-CD still presented a capacity of 200 mAh/g at the highest current level. To our knowledge, such a rate capability is among the best of reported values.

A similar trend was observed in cycling stability testing (**Figure 3.8B**), where when cycled at 400 mA/g_{MoSx} after 100 cycles, the MoS_x-AD sample had a 10% capacity retention (60 mAh/g), which the MoS_x-CD sample showed a 40% capacity retention of 200 mAh/g. Additionally, the MoS_x-CD sample maintained a higher Coulombic efficiency (> 99.4%) during cycling, while MoS_x-AD showed a lower Coulombic efficiency (< 98%) over the initial 30 cycles, with a minimum value of 94% on Cycle 20, and then efficiencies of ~ 99% over cycles 50-100 (Figure 3-5B, open circles). To explain potential contributions to the differences observed during cycling, the MoS_x-AD sample was shown to contain both a mixture of MoS_3 and elemental sulfur (S_8), with a ratio of MoS_3:S_8 of 8:1. Within the tested voltage window (3.0 to 1.0V), the elemental sulfur is lithiated, which in turn can form polysulfide species, thus potentially leading to the observed capacity fade. With MoS_3, it was previously identified to undergo lithiation reversibly (via a reversible insertion mechanism: $yLi^+ + MoS_x \rightleftharpoons Li_yMoS_x$ where no bond breaking or formation of Li_2S or polysulfides were observed.[167] Since the MoS_x-CD sample only contained MoS_2 and not excess elemental sulfur, it could be concluded that the lithiation would proceed only through the reversible insertion mechanism, which could contribute to the more stable observed cycling behavior.

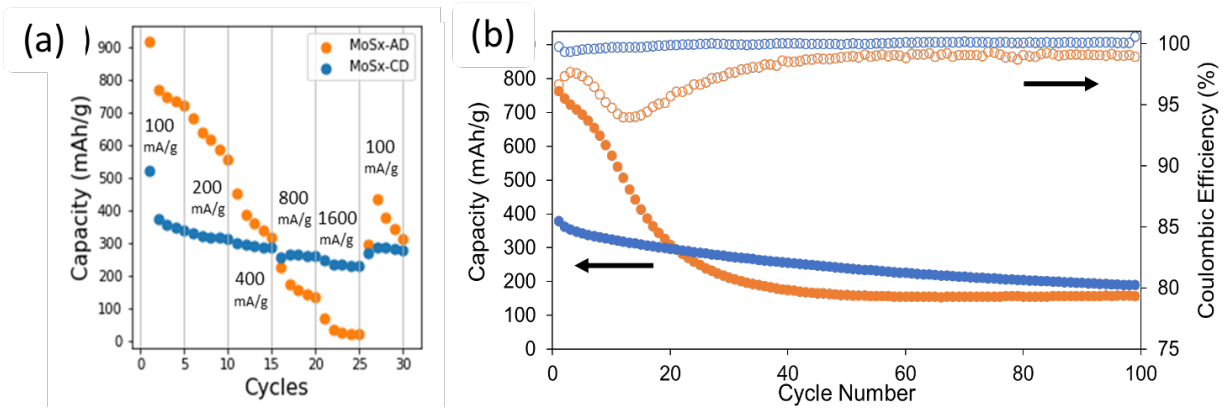

Figure 3.8. a) rate capability from 100 mA/g_{MoSx} to 1600 mA/g_{MoSx}, and (b) cycling stability (solid circles) and corresponding Coulombic efficiency (empty circles) at 400 mA/g_{MoSx}.

3.2.4 Conclusions

In conclusion, we have demonstrated that electrodeposition has great potential in manufacturing MoS_x-based sulfur-equivalent electrodes for lithium based batteries. By tuning the deposition condition, amorphous MoS_x with different physical and chemical properties, as well as electrochemical characteristics can be prepared. MoS_x deposited at anodic potential (MoS_x-AD) showed a higher initial capacity of 919 mAh/g attributed to its higher sulfur content. In contrast, MoS_x deposited at cathodic potential (MoS_x-CD) showed a lower initial capacity of 522 mAh/g with decent cycling stability up to 100 cycles and significantly improved rate capability attributed to its higher conductivity and improved Li^+ transport properties. Compared to conventional fabrication approaches for composite electrodes, electrodeposition can produce MoS_x based electrodes with similar capacity yet improved rate capability. The electrodeposition approach was highlighted here as a scalable fabrication method.

Acknowledgements

ACM acknowledges Brookhaven National Laboratory for support of the scanning electrochemical microscopy research. X-ray photoelectron spectroscopy was performed at the Center for Functional Nanomaterials, Brookhaven National Laboratory, an Office of Science User Facility, which is supported by the U.S. Department of Energy, Office of Basic Energy Sciences, under

Contract No. DE-SC0012704. E.S.T. acknowledges the William and Jane Knapp Chair in Energy and the Environment. Material synthesis and characterization of the pristine samples was supported as part of the Center for Mesoscale Transport Properties, an Energy Frontier Research Center supported by the U.S. Department of Energy, Office of Science, Basic Energy Sciences, under award #DE-SC0012673. Sulfur-equivalent electrochemistry of the materials was supported by the U.S. Department of Energy Office of Energy Efficiency and Renewable Energy, under award DE-EE0008208.

Chapter IV

Material Properties and Electrochemical Response

The following sections are adapted from publications of highly collaborative work as part of the Center for Mesoscale Properties Energy Frontier Research Center (m2m, and m2m/t). Attribution of collaboration are noted below, and details from the full reports can be found in each of the full publications.

4.1 Employing a multiscale method of characterization and analysis

The following is adapted from the following ACS AuthorChoice License, which permits copying and redistribution of the article or any adaptations for non-commercial purposes:

Abraham, A., Housel, L. M., Lininger, C. N., Bock, D. C., Jou, J., Wang, F., West, A. C., Marschilok, A. C., Takeuchi, K. J., Takeuchi, E. S., Investigating the Complex Chemistry of Functional Energy Storage Systems: The Need for an Integrative, Multiscale (Molecular to Mesoscale) Perspective, *ACS Cent. Sci*, 2016, 2(6), 380-387. DOI: 10.1021/acscentsci.6b00100
Copyright © 2016 American Chemical Society.

Personal contribution: Contributor to manuscript draft, generation of Figure 4.2 (with Lisa Housel)

Acknowledgement of collaboration:

The text below is reproduced in part from the above reference, describing the work of members of the Energy Frontier Research Center (EFRC) m2m.

Co-author contributions include:

Lisa M. Housel – Equal contribution to manuscript draft and Figure 4.2

Dr. Christianna N. Lininger, Dr. Alan West – Conducted work on continuum modeling

Dr. David C. Bock – Conducted work on XAS probing discharge mechanism of magnetite

Jeffrey Jou- Contributed to manuscript draft

Dr. Feng Wang – Conducted microscopy work probing discharge mechanism of magnetite

Additional contributors from other EFRC center members can be found in the associated references

4.1.1 Introduction

Batteries are application driven and scientifically complex electrochemical energy storage systems. They are employed in many uses of varying scales, including portable devices, transportation, and stationary storage. High energy density batteries, such as lithium ion, dominate the portable electronics market, where the batteries and devices are typically hand-held and small. Widespread implementation of large format batteries, such as those used for electric vehicles, or for stationary electrical storage demands additional consideration of factors contributing to inefficiency of the EES leading to heat generation. While the generation of heat by a small battery may be unwanted, , the generation of heat by a large format battery demands careful management to prevent potentially catastrophic performance and/or safety concerns.

The governing principles of EES is that energy is the sum of heat and work, and the objective for efficient energy storage systems is to maximize useful work (w) and minimize waste heat (q), as shown in Equation 4.1-1.

$$\Delta E = q + w \qquad \textit{Equation 4.1-1}$$

During the operation of a battery, both ions and electrons are transported to ensure both mass balance and charge balance. During this process, multiple size domains of the electrode are involved, including changes on the atomic, molecular and electrode scale level, that can contribute to phase changes, structural composition, and lead to inefficiencies in the cell, which broadly, can be categorized as polarization. Polarization occurs when there is a difference between the theoretical potential and the usable output. The operating potential is a complex

combination of several terms, including the standard potential, activation and concentration polarization terms, operating current within the cell, and internal resistance, as described by Equation 4.1-2.

$$E = E^0 - [(\eta_{ct})_a + (\eta_c)_a] - [(\eta_{ct})_a + (\eta_c)_a] - iR_i \qquad \textit{Equation 4.1-2}$$

Where:

E = Operating potential

E^0 = Standard potential

i = Operating current

$(\eta_{ct})_a$ and $(\eta_{ct})_c$ = Activation polarization at the anode (a) an cathode (c)

$(\eta_c)_a$ and $(\eta_c)_c$ = Concentration polarization at the anode (a) an cathode (c)

R_i = Internal resistance of the cell

It is important to point out that the operating potential cannot be appropriately described without including both internal resistance and transfer properties. For example, activation polarization describes the kinetics of charge transfer, which concentration polarization describes the kinetics of mass transfer. In EES, where the movement of a negatively charged electron is accompanied by the movement of a positively charged ion to maintain charge balance, it is critical that both transfer properties be accounted for. In combination with the cells internal resistance, these terms can affect the resultant properties that make up conduction at their perspective interfaces.

In carrying out characterization of EES, there are several size domains and characterization tools that can be incorporated to provide a wholistic view of processes both during and or before and after (dis)charge. For example, in the working system, techniques such as Electrochemical Impedance Spectroscopy (EIS) and galvanostatic techniques can provide information on the working system as a whole, but do not provide detailed information when it pertains to heterogeneous processes, such as charge transfer or mass transfer kinetics, as well as areas of localized resistance. Additionally, when local techniques are used in isolation, they may not be fully descriptive of the system as a whole, so when approaching a complex, full working system, it is important to consider macroscopic phenomena from information from all levels, including atomic, interfacial and mesoscale levels.

After taking into account the multiple variables that can lead to overpotential, a fundamental question is what factors contribute to the difference between the theoretical and the useable energy in a system. Theoretical estimates for energy, which can include reported values such as theoretical capacity, energy density and voltage, are frequently reported in the literature based on the system of interest. While these values are a useful tool and can highlight the benefits of studying a system, there is frequently a large discrepancy between the reported theoretical values and experimental observations. While these differences in theoretical and observed values can be attributed in part to the factors described in Equation 4.1-2, the variation in test conditions further complicates pinpointing deviations. The ability to identify the factors that contribute to performance differences between theoretical versus functional capacity, voltage, and energy density, as well as understanding the critical mechanisms during (dis)charge will lead to a comprehensive understanding of EES systems[197] and set a strong baseline for diagnosing and future design considerations of batteries.

Experimental test conditions can vary greatly and can introduce additional subtleties that make it very challenging to provide quantitative metrics. The fundamental issues influencing ion and electron transport, how phenomena change across multiple domains and interfaces and how this interacts with the underlaying atomic and molecular structure is essential.[198, 199] In such cases, investigation over multiple length scales can provide the fundamental understanding that will lead to scientific insights.

The application of integrating investigations over multiple length scales, requires a variety of characterization and computation approaches, incorporating theoretical predictions to inform and explain experimental trends, and to incorporate various modes of characterization tools to evaluate properties on the molecular, crystallite, electrode and working system level. Using magnetite (Fe_3O_4) as a model material, a path for combining synthesis, characterization, electrochemistry, and theory will demonstrate that this type of multi-modal approach can lead to a more comprehensive understanding that can inform development to improvements of battery function.

This section summarizes this approach for a case study for magnetite (Fe_3O_4) as a material that provides a representative case study for this type of multi-scale approach. Details on the particular contributions of each of the techniques highlighted can be found in more detail here.[200]. Subsequent examples will extend this analysis to include other physical characterization

methods to evaluate surface treated magnetite, and then move on to and examine the role of silver in an aqueous zinc system and explore the electrochemical effects of phase change in polymorphic vanadium oxide, VO_2.

4.1.2 Atom scale level characterization and theory

Fe_3O_4 has been a material of particular interest for the expansion of the lithium ion battery into larger scale applications including electric vehicles and the grid, in part due to its high abundance, low cost, and low toxicity.[201] Fe_3O_4 has an inverse spinel structure with an oxygen anion framework, with Fe^{3+} ions occupying both octahedral and tetrahedral sites, while Fe^{2+} ions solely reside in tetrahedral sites[202] as shown in **Figure 4.1** generated from the magnetite structure parameters.[203] Fe_3O_4 along with other metal cation containing compounds, including metal oxides, fluoride, oxyfluorides, nitrides and sulfides[204-208] has been shown to undergo multiple electron transfers (MET) for each metal cation. The MET reactions in these compounds enable higher energy density when compared to intercalation electrodes. When Fe_3O_4 has been fully reduced to Fe^0 and Li_2O, it undergoes a complex process involving multiple phase transitions and is strongly dependent on the electrochemical environment.[202, 209-214]

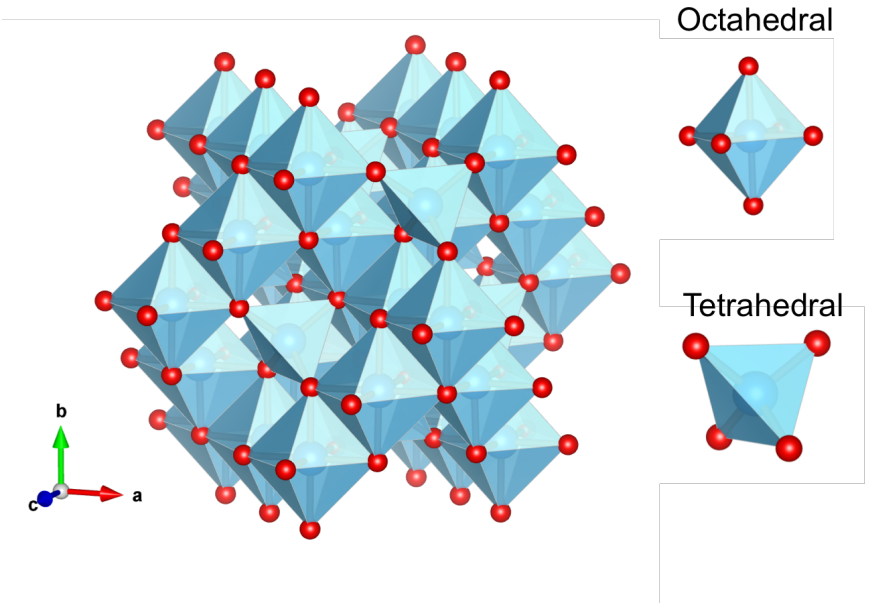

Figure 4.1. Crystal structure of inverse spinel magnetite, Fe_3O_4 (red spheres = Oxygen, blue tetrahedra and octahedra represent Fe^{2+} or Fe^{3+}.)

Previous X-ray diffraction (XRD) studies of phase transformation in Fe_3O_4 have suggested that there are multiple intermediate phases including the rock salt FeO[215] or the rocksalt like phase Li_xFeO_2.[216] In addition to phase changes as a result of (de)lithiation, moderate volume changes occur (i.e., 15% from Fe_3O_4 to $Li_2Fe_3O_4$)[214] which can lead to increases in resistance due to loss of electrical contact within an electrode or between the active material and current collector. Due to the poor crystallinity of lithiated Fe_3O_4 materials, XRD analysis has been limited in its ability to determine the structure of the phases involved, so a complete description of the mechanism of Li and Fe ion migration during MET reactions has remained elusive. Atomic scale level characterization including characterization techniques such as scanning transmission electron spectroscopy (STEM), electron energy loss spectroscopy (EELS) and electron diffraction can identify both chemical and structural changes with high spatial resolution (to the atomic level). For example, the site occupancies of all species (including anions O^{2-} and cations Li^+, Fe^{2+}, and Fe^{3+}), were identified by using annual-bright-field (ABF) STEM imaging in combination with high angle annular-dark field (HAADF) STEM imaging and EELS.[214]

X-ray absorption spectroscopy, provided local information on the surrounding atomic environment within ca. 6Å around the absorbing atom (EXAFS region), and information on local oxidation state (XANES). XAS methods have been previously used to determine detailed electrochemical mechanisms in electrodes that exhibit complex multistep processes, although amorphous phases were primarily involved.[217-221] This combination of techniques can complement and provide additional insight into information obtained by standard X-ray diffraction methods. Notably, XRD can provide information on long-range ordering of the crystalline phases in the materials, but may not be suitable for characterization of structural changes in nanomaterials formed as a result of electrochemical reduction and oxidation, due to their small crystallite size and associated line broadening.[222, 223,224]

The overall reduction for Fe_3O_4 obtained from using a variety of characterization techniques as noted above, can be summarized by the scheme below, showing the progression from reduction with lithium ion insertion to full conversion with formation of iron metal, Fe^0 and lithium oxide, Li_2O:

(1) Reduction by one electron equivalent and insertion of one Li^+ ion to form $LiFe_3O_4$

(2) Reduction by second electron equivalent insertion of the second Li^+ ion to form $Li_2Fe_3O_4$

(3) Additional reduction and insertion of lithium ions to form a composite Li_2O•FeO

(4) Full conversion reaction leading to metallic Fe^0

Density functional theory with the Hubbard correction (DFT+U) was applied for correlating the mechanism to structural ordering, where the partially lithiated $Li_2Fe_3O_4$ structure was shown to preserve the O anion framework with 15% volume expansion, consistent with the experimentally observed structure by EXAFS.[214] Retention of the O anion ccp structure enabled multiple lithium intercalation and conversion reactions where partial reduction at less than 4 electron equivalents resulted in phase transformations from inverse spinel to rock salt like phases, with limited morphological changes. Upon further lithiation within the identified ccp O anion framework, local cation reordering occurred, leading to FeO phase and finally to a Fe/Li_2O nanocomposite phase.

4.1.3 Mesoscale Characterization and Model Development

Synthetic control of crystallite size has been demonstrated to increase the usable capacity by shortening the path length for Li ion diffusion, thus enhancing ion accessibility at higher discharge currents in previously reported metal oxide electrode materials.[206, 225-228] In particular, control of crystallite size has been shown to be important for densely structured materials, such as magnetite. A remaining challenge in realizing magnetite as a usable electrode in a lithium ion battery is to be able to achieve its high theoretical capacity.[229] Despite the improved capacity from efforts to synthetically control nanocrystallite magnetite including size[230] and morphology[231] to limit the path length required for Li ion transport, the theoretical capacity has not been uniformly reached. While prior studies have addressed crystallite size effects,[216, 232-237] on the electrochemistry of Fe_3O_4, there have been few reports that address agglomeration[238, 239] which, due to the nature of active battery material being combined with a conductive additive and binder, is an avenue that warrants analysis and investigation. Additionally, while some of the above studies have indicated that agglomeration during cycling may correlate to electrochemical properties, they have not quantified agglomerate size or made direct correlations of its effect on the system performance.

A complete study of a nanocrystalline material in a battery electrode was conducted to provide a holistic view of the cell and considered both the crystallite size of the material and the

agglomerate size.[197] The combination of sample preparation using an ultra-microtome and characterization using TEM combined with 2D mapping by transmission X-ray microscopy (TXM) and X-ray absorption near edge spectroscopy (XANES) provided a comprehensive two-dimensional map, showing the distribution of iron, and its corresponding oxidation states both before and after cycling. Mapping techniques such as TXM-XANES provide information on the distribution of oxidation states of the samples over a large sample area. While it was found that the smaller crystallite size Fe_3O_4 displayed more uniform discharge, agglomerate size of the sample was not found to depend on crystallite size, as previously suspected from prior wok on particle size of powders.[230, 234] The identification of agglomerates has led to the electrode being categorized into varying length scales with different corresponding properties. In concert with the overarching theme of microscale to mesoscale in understanding battery performance, the three length scales existing within the electrode have been identified using continuum modeling as the bulk electrode (macroscale), the agglomerates (mesoscale), and crystals (nanoscale).[229, 240]

In light of the insights provided by the multiscale performance model of Fe_3O_4 containing electrodes[229], a subsequent study[241] was performed with the aim of reducing agglomeration of Fe_3O_4 as a means of improving lithium ion transport rates, and, thus, delivered capacity. Agglomeration was effectively suppressed in Fe_3O_4/carbon black composite electrodes by using oleic acid as a dispersing agent. A heat treatment process was then used to remove the oleic acid, which was found to result in unfavorable performance, while maintaining Fe_3O_4 dispersion in the carbon black matrix. Thus, in agreement with the performance model simulations, the composite electrodes with dispersed Fe_3O_4 initially delivered a higher functional capacity compared to the electrodes with aggregated magnetite under similar rates of discharge. However, upon extended cycling, the dispersed material exhibited increased capacity fade relative to the agglomerated Fe_3O_4 composites. X-ray absorption spectroscopy measurements of electrodes recovered from cells cycling along with complementary electrochemical impedance spectroscopy data facilitated a mechanistic explanation of the observed performance. After cycling, the dispersed Fe_3O_4 was more oxidized in the discharged state and had higher charge transfer resistance, suggesting that increased surface film formation on the highly dispersed material causes reduced reversibility.

4.1.4 Conclusions

The above examples demonstrated the integration of atomic level characterization techniques to propose a mechanism and identify ion occupancies. Density Functional Theory (DFT) proposed an explanation for experimentally observed trends in volume exchange upon lithiation. On the mesoscale, combined X-ray and microscopy techniques provided insight into agglomeration in a composite battery electrode, and continuum modelling developed nanoscale and agglomerate scale models that subsequently informed subsequent work. These examples affirm that multiscale characterization of Fe_3O_4 composites is critical for full understanding of electrochemical performance. Detailed insights into the performance of Fe_3O_4 as an anode material will help enable realization of its promise as an anode material with a theoretical of ~2.5X higher than that of standard carbon anodes currently used in lithium ion batteries. A review of reported capacities of Fe_3O_4 based batteries shows that their functional capacities range almost 10-fold when configured into a variety of heterostructures, as illustrated in **Figure 4.2** compiled from data from the literature.[202] Notably, the theoretical first discharge capacity of Fe_3O_4 is 924 mAh/g, thus additional capacity is contributed by the carbon component of the heterostructure. This denotes that increased understanding and developments in electrode design will help enable further utilization of active materials.

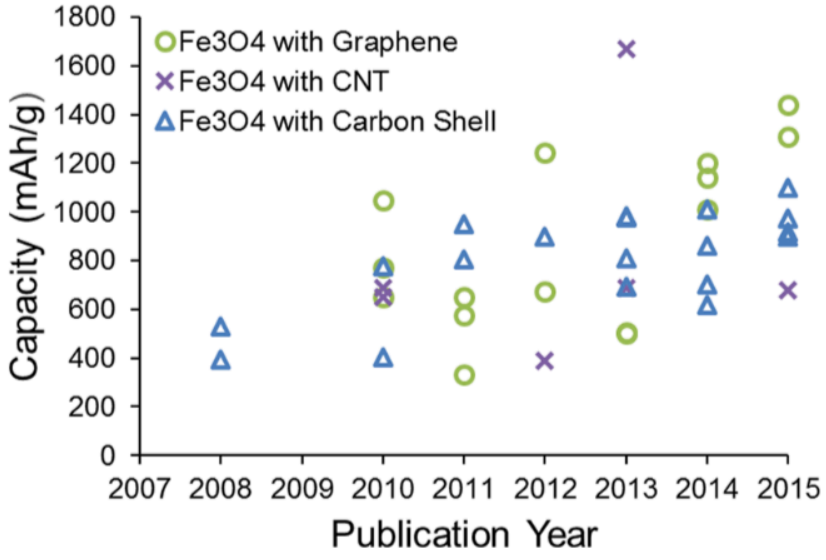

Figure 4.2. Capacity as a function of publication year for Fe_3O_4 based batteries.

Acknowledgements

The authors acknowledge the Center for Mesoscale Transport Properties, an Energy Frontier Research Center supported by the U.S. Department of Energy, Office of Science, Basic Energy Sciences, under Award No. DE-SC0012673 for financial support. C.N.L. acknowledges the support of the National Science Foundation Graduate Research Fellowship under Grant No. DGE-11-44155. The authors thank Yelena Belyavina and Lisa L. Jansson for assistance with graphic artwork. The authors commend the Department of Energy for the vision to create Energy Frontier Research Centers which enable multidisciplinary research over multiple length scales. The opportunity for engagement and extended interaction among scientists with complementary expertise as part of the Center for Mesoscale Transport Properties (m2M) EFRC has enabled the scientific achievements, as well as inspired the philosophy described here.

4.2. Examining surface properties in functionalized magnetite

Reprinted (adapted) with permission from:

Deliberate Modification of Fe_3O_4 Anode Surface Chemistry: Impact on Electrochemistry, Wang, L., Housel, L. M., Bock, D. C., Abraham, A., Dunkin, M. R., McCarthy, A. H., Wu, Q., Kiss, A., Thieme, J., Takeuchi, E. S., Marschilok, A. C., Takeuchi, K. J., *ACS Appl. Mater. Interfaces*, **2019**, *11*, 19920-19932.] Copyright © 2019, American Chemical Society.

Personal contributions: Contact angle data collection and analysis, contributed to AC-SECM data analysis, and contributions to manuscript draft.

Acknowledgement of collaboration:

Dr. Lei Wang- Development, synthesis, and characterization (XRD, Raman, TEM) of pristine and surface treated magnetite, electrochemistry, manuscript preparation

Lisa M. Housel- XRF mapping and XANES data collection and analysis

Dr. David C. Bock- XRF-mapping and XANES data collection and analysis

Mikaela R. Dunkin- XANES data analysis

Allison H. McCarthy- XRF mapping data analysis

Qiyuan Wu- Collection and analysis of AC-SECM data of pristine and surface treated magnetite samples

Dr. Andrew Kiss, Dr. Juergen Thieme - Beamline 5- ID, submicron resolution X-ray spectroscopy (SRX) of the National Synchrotron Light Source II

4.2.1 Introduction

Section 4.1 introduced the methodology and benefits to utilizing various characterization techniques to generate a wholistic picture of an energy storage system on multiple length scales, using magnetite as a case study. Following a similar concept, where an integrated characterization approach is utilized, the section below addresses how surface modified magnetite is characterized by both physical, chemical and electrochemical methods. This section will focus specifically on techniques that provide information on the surface of a composite electrode, and how these techniques can be utilized in tandem to demonstrate generate trends in the surfaces of composite materials.

There is a general trend towards the utilization of more widely abundant and environmentally benign lithium ion battery materials. As the lithium ion battery expands into more applications, it is imperative to consider both material availability and electrochemical performance in developing materials for lithium ion batteries. Graphite, which is a commonly used anode in lithium ion batteries, is limited by lithium deposition on the anode surface. Lithium deposition leads to dendrite growth which then lead to decreased cycling stability, as well increasing the potential for catastrophic shorts. As an alternative to graphite anodes, earth abundant iron oxides, such as magnetite (Fe_3O_4), have been a promising candidate for LIB anodes. The benefits of magnetite include its high theoretical capacity (926 mAh/g), high environmental abundance, and relative non-toxicity. Despite its attractive properties, challenges still exist in reaching its high theoretical capacity and sustained electrochemical cycling, including the tendency of the formation of iron nanocrystals to form and become dispersed with a Li_2O matrix during discharge leading to dramatic volume changes during cycling, which then can result in delamination from the current collector.[242, 243] Additionally, the limited electrical conductivity of magnetite can lead to decreased charge transfer and ion transport, especially at higher current densities.[244, 245]

There are two general methods that have been employed to increase the rate capability and cycling stability of magnetite: synthetic control of the active material, and inclusion of conductive additives into the composite electrode. For the strategy that addressees the active material (Fe_3O_4), synthesis methods to tune transport properties within generated nanoparticles

have been reported.[230, 246-248] The other approach, where conductive additions are added to the composite electrode, seeks both to enhance the overall electrical conductivity as well as accommodate volume changes that occur during cycling. The scope of materials used as conductive additives is wide, and includes materials such as carbon nanofibers, graphene, carbon nanotubes (CNTs) and conducting polymers.[249] Despite improvements to conductivity from the incorporation of carbon based additives, the produced composite electrodes still have a low volumetric capacity. This is contributed to from the population of void spaces that exist within the carbon materials themselves that lead to the decreased density of the carbon additive, which can lead to low volumetric capacities.[250] Maintaining reasonable volumetric capacities within composite electrodes becomes increasing critical as high level working system designs have limitations on the size of functional electrodes.

There has been increasing interest in taking the surface properties of the composite electrode into consideration when considering subsequent electrochemistry.[251-254] Surface treatment based on inorganic coating compounds such as $AlPO_4$ [255] and MO_x (M= Zr, Al, Ti, B)[256, 257] has demonstrated improvements in the energy density and cycle performance of layered $LiCoO_2$ and spinel $LiMn_2O_4$ cathodes. This is attributed to improvements in thermal stability, as well as suppression of electrolyte decomposition, strain formation during phase transition, and Co/Mn dissolution in the electrolyte. Although the coating of inorganic materials on the surface of metal oxides/phosphates improves the electrochemical performance and safety properties of batteries, the microstructure of the coating layers and the mechanism of improvement are not fully understood. Additionally, challenges still remain in creating conformal inorganic coating layers while maintaining electron and ion conductivity throughout the whole electrode. In addition to the inorganic surface coatings to facilitate metal oxide dispersion, capping agents and surfactants have also been employed.[258] For example, oleic acid has been utilized as a capping agent in controlling the aggregate size dispersion of magnetite, Fe_3O_4 within a conductive carbon composite. While the addition of oleic acid capping agent to the Fe_3O_4 did demonstrate a reduction in aggregation, the insulating effect of the capping agent impeded electron transfer and ion diffusion which was observed in extended electrochemical cycling. Heat treatment was requirement to remove these effects of the capping agent on the electrode.[259]

Separate studies have addressed improving ionic and electronic transport by controlling the boundary between a metal oxide motif, such as $Li_4Ti_5O_{12}$[260] and Fe_3O_4[261] and the adjoining CNTs or MWNTs. Small organic ligands were used as bridging agents between the metal oxide and the nanotubes either by covalent attachment (using an amine-functionalized linked, 3-aminopropyl triethylsilane (APTES), or by a non-covalent π-π interaction strategy. The non-covalent attachment, connected the CNTs with the metal oxide utilized π bond interactions between the aromatic, 4-mercaptobenzoic acid (4-MBA) and the CNTs. In electrode testing, it was suggested that the π-π interaction strategy outperformed the covalent interaction strategy, due to smaller charge transfer resistance and faster Li ion diffusion observed in the 4-MBA electrode when compared to APTES.[260] The differences clearly highlighted the significant effect of the physio-chemical structure of the different surface-treatment agents upon the resulting electrochemical properties.[262] It is worth noting that although the two previous studies unambiguously suggested the importance of the surface ligands in governing the resulting electrochemical performance, the incorporation of additional CNTs was likely to decrease the tap density and volumetric capacity of the final electrode. Hence, a more in-depth study was needed to deconvolute the combination effect and delineate merely the impact of surface chemistry governed by the ligands on the resulting electrochemical behaviors of the functionalized metal oxide electrodes.

This section focuses on surface studies of electrodes of the surface treated of Fe_3O_4 without the inclusion of CNTs. This seeks to improve the dispersion of the Fe_3O_4 active material within the electrode, without limiting charge or mass transfer, maintain the volumetric capacity of the electrode, and delineate the surface chemistry from the electrochemical behavior. Synthesized magnetite nanoparticles, have been separately treated with four small molecules, which are relatively small organic compounds with terminal -COOH group, possessing a strong affinity for Fe sites or the -OH groups on the Fe_3O_4 surface. The four ligands can be classified as either aliphatic or aromatic, with or without the -SH functional group. These categories provide information on how surface-treatment agents can influence the electrochemistry when used as a surface treatment in Fe_3O_4 electrodes. Insight was obtained on the impact of the surface chemistry by either the presence or a π-conjugated or alkyl carbon system, as well as the presence of the -SH (and -COOH) groups of the surface agents. The four surface agents

addressed in this study are: 4-Mercaptobenzoic acid (MBA) (aromatic, pendent -SH group), benzoic acid (BA) (aromatic), 3-Mercaptopropionic acid (MPA), (aliphatic, pendent -SH group), and Propionic acid (PA), (aliphatic), whose structures are shown in **Figure 4.3.**

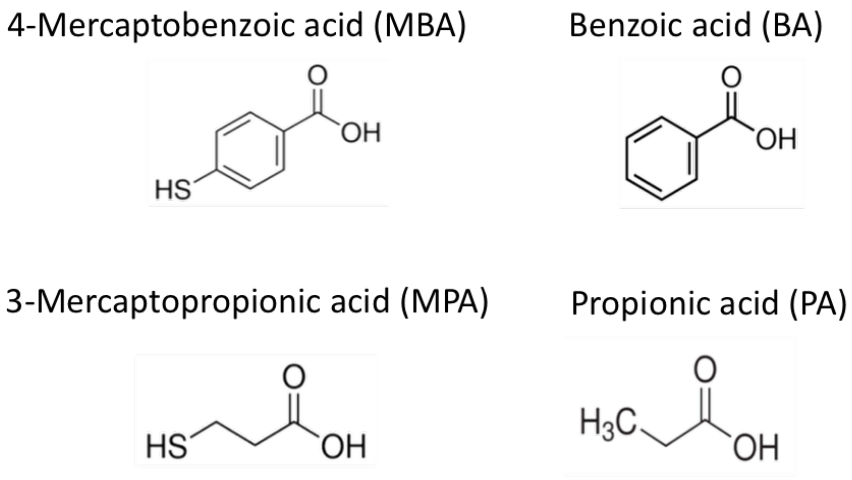

Figure 4.3. Structures of four surface treatments used on magnetite, Fe_3O_4.

Methods for Evaluation of surface properties of treated Fe_3O_4 cast electrodes

Contact Angle Measurements

Contact angle measurement utilizes a liquid drop on a solid surface to provide relative information on the wettability of a surface from a liquid. The contact angle can be as low as 0° which would denote complete wettability, up to the theoretical limit of 180°. Wettability is gauged from the angle that is tangent to the drop in relation to the surface. Young's equation, (Equation 4.2-3) shows the relationship between the surface free energy of the solid, (σ_s), the surface tension of the liquid (σ_l), the interfacial tension between the liquid and the solid (σ_{sl}), and the contact angle (θ).[263] A diagram showing a representative contact angle schematic is shown in **Figure 4.4.**

$$\sigma_s = \sigma_{sl} + \sigma_l \bullet \cos\theta \qquad \textit{Equation 4.2-3}$$

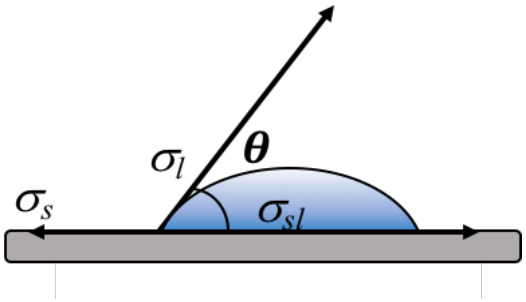

Figure 4.4. Diagram of components of contact angle following Equation 4.2-3

In a previous literature report of carbon electrodes, contact angle was measured using 1M bis(trifluoromethane)sulfonimide lithium salt (LiTFSI) in various nonaqueous solvents and solvent mixtures (including propylene carbonate (PC), ethylene carbonate (EC), and dimethoxyethane (DME). Measurements on the surfaces of carbon electrodes showed a correlation of increased discharge capacity with an increased contact angle, where a contact angle of 47° was 167.5 mAH/G (PC/EC), whereas a contact angle of 5° correlated with a discharge capacity of 27.4 mAh/g in PC/DME.[264]

More recently, contact angle has been utilized recently in evaluating the wettability of binder (either PVDF or PFTE) and carbon composites on a substrate for applications for Li-O_2 batteries.[265] Utilizing static contact angle measurements, the type of binder, amount of binder, and mixture of both binders were compared. The drop consisted of electrolyte of 1M LiTFSI/TEGDME with an average drop volume of 5 µL per drop. As the percentage of PTFE was increased from 15 to 35%, there was a subsequent increase in contact angle from 128.4 to 138.5°, showing poor wettability. A mixed electrode, consisting of a single 15% PVDF coating sandwiched between two 15% PTFE coatings, had a slightly lower contact angle compared to the PTFE (15%) sample. Samples containing only 15% PVDF had the lowest contact angle, 36.5°, noting that it had a greater wettability compared to the PTFE and mixed electrode preparations. Interestingly, when contact angle measurements were correlated to specific discharge capacity, the mixed (PTFE-PVDF-PTFE) sample with a contact angle of 118.8° had greater than 3 times the discharge capacity of the PVDF sample, which had better wettability. This study had shown the importance of the composite electrode surface properties, and notes how wettability

necessarily may not directly correlate to improved discharge capacity.[143] A schematic showing changes in contact angle to trends in wettability is shown in **Figure 4.5.**

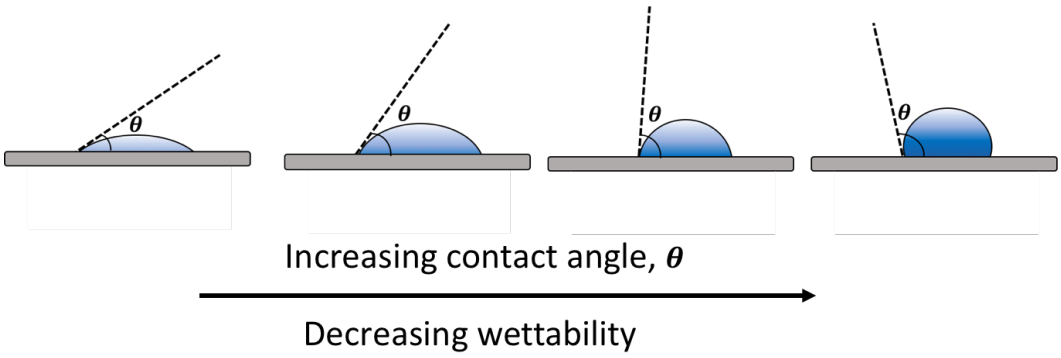

Figure 4.5. Diagram showing relationship of contact angle with drop shape and wettability.

4.2.2 Experimental

Additional details on synthesis of Fe_3O_4 nanoparticles, surface treatment and structural characterization can be found in the full reference.[266]

Contact Angle Measurements. Contact angle measurements were performed using a Kyowa Dropmaster Model DM-501 using the Sessile Drop method on pressed composite electrodes of 70% Fe_3O_4 (pristine or treated)/20% SuperP/10% PVdF using 1 M $LiPF_6$ in EC/DMC (3:7). The following Fe_3O_4 treatments were measured: MBA, BA, MPA, PA and pristine. FAMAS software was used for contact angle analysis using a half angle method. Values were averaged for nine measurements per condition and reported with one standard deviation. All contact angle measurements were performed in a dry room at 2% relative humidity to minimize water uptake during measurement.

AC-SECM measurements. Alternative current scanning electrochemical microscopy (AC-SECM) was performed using a commercial SECM instrument (M470, BioLogic). An ultramicroelectrode (UME) with radius a = 5 μm was used as the working electrode. An Ag/AgCl standard electrode and a Pt sheet were used as reference electrode and counter electrode respectively. Tap water with conductivity of ~200 μS was used as electrolyte. The following conditions were used for each sample type: 0V (vs. open circuit potential) DC-bias, 100 mV AC-bias, and 100kHz AC-frequency. The reported AC-impedance magnitude for each

sample is the average value of the scanned area (300 μm x 300 μm with 5 μm scan step, totaling 3600 measurements for each sample). Error bars shown in **Figure 4.7** represent ± one standard deviation for each sample.

4.2.3 Results and Discussion

Summary of Initial Characterization of Fe_3O_4 and ligand-functionalization Fe_3O_4 NPs

As-prepared Fe_3O_4 NPs were measured 8.8 ± 1.3 nm on average in diameter from TEM, with a corresponding XRD pattern that agreed well with the cubic inverse spinel Fe_3O_4 structure (JCPDS 19-0629). Characterization of the magnetite surfaces after ligand functionalization was confirmed by FT-IR analysis. Additional information on the details of confirmation of surface functionalization can be found in the full literature report[266]. To determine the effects of the surface-treatment on the dispersion of the synthesized Fe_3O_4 NPs, particle size analysis was conducted using the solvent that is used to form the slurry during the electrode fabrication process, N-methyl-2-pyrrolidinone (NMP). Two general trends were observed: surface treatment lead to a narrower size distribution of the Fe_3O_4 aggregates, and the percentage of the larger sized aggregates was decreased. The two aromatic ligands, MBA and BA showed a greater decrease in aggregation, which can be contributed in part to higher solubility of these ligands in the NMP solvent. Of all of the four surface ligands tested, MPA appeared to be the least effective in terms of reducing Fe_3O_4 NP aggregation.

Composite electrode surface measurements

After characterization of the synthesized Fe_3O_4 nanoparticles, confirmation of surface coating, and determination of tendency for aggregation in an NMP dispersion, surface measurements were obtained on composite electrodes to correlate electrode scale properties to subsequent electrochemical measurements. Contact angle measurements were performed to provide additional information regarding wetting in the coating electrodes containing pristine and surface-treated Fe_3O_4 particles using the same electrolyte (1 M $LiPF_6$ EC/DMC (3:7)) as used in the electrochemical tests. To ensure uniformity in representation of contact angle measurement, nine electrode samples were used for each condition, and reported with one standard deviation. The following contact angles were obtained on pressed composite electrodes of 70% Fe_3O_4 (pristine

or treated)/20% SuperP/10% PVdF using 1 M $LiPF_6$ in EC/DMC (3:7) treated with MBA, BA, MPA, PA, and untreated: 29.5°(±4.4°), 25.6°(±1.1°), 19.2°(±1.4°), 27.1°(±2.0°), and 29.7° (±1.9°). Representative images of contact angle measurements on treated and untreated Fe_3O_4 coatings are shown in **Figure 4.6**. The untreated Fe_3O_4 sample is within the range of contact angle measurements reported in the literature for deposited thin films of magnetite,[267] noting that the incorporation of conductive additive and binder did not alter the contact angle outside of the range expected for the pristine material.

The higher contact angle (29.7°) associated with the untreated Fe_3O_4 suggests a lesser degree of wetting when compared to the MPA, which is aliphatic and contains both -SH and -OH end groups. There was not a notable distinction between the contact angle differences between aromatic compounds (MBA and BA) compared to aliphatic compounds (MPA and PA), or when comparing thiol containing groups, as the two thiol containing functionalities (MBA and MPA), had differences in contact angle (29.5° and 19.2° respectively), with the MBA treated sample being closer to the pristine.

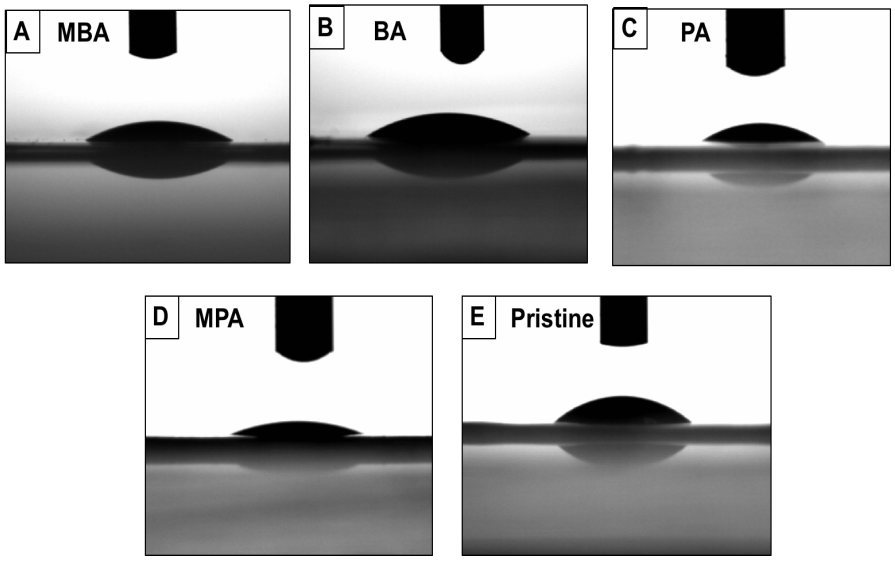

Figure 4.6. Representative contact angle measurements using 1M $LiPF_6$ in EC/DMC (3:7) electrolyte on ligand-Fe_3O_4/Carbon/PVDF coatings: (A) MBA, (B) BA, (C) PA, (D) MPA, (E) Pristine.

To complement the contact angle measurement, the average surface AC-impedance magnitude of different samples was measured and is compared to contact angle measurements in **Figure 4.7**. Initially, a typical AC-impedance magnitude map was obtained, where it was clear that the change in surface AC-impedance magnitude was fairly minor throughout the scanned area indicating homogeneous distribution of the electrode composite, which can be found in the Supplementary Information in the full reference.[266] The average surface AC-impedance magnitudes for MBA, BA, MPA, PA and pristine samples were 17.28 ± 0.10, 16.64 ± 0.09, 15.98 ± 0.10, 17.29 ± 0.10, and 17.62 ± 0.57 kΩ, respectively. Interestingly, the surface impedance magnitude shared the same general trend in the contact angle of different samples. The MPA sample has the smallest surface AC-impedance magnitude, followed by the BA sample. MBA and PA have surface AC-impedance magnitude closest to that of the pristine Fe_3O_4. This general trend also agreed with the trend in R1 in the EIS validating the fitting results of EIS data (details in full report).[266]

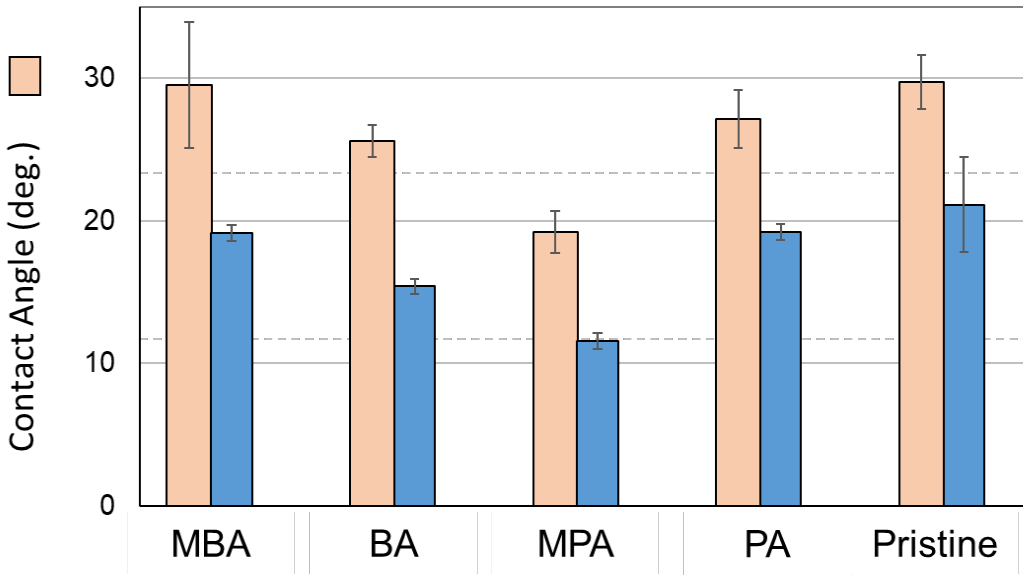

Figure 4.7. Measured average contact angle (orange) and SECM AC-impedance magnitude (blue) of MBA, BA, MPA, PA, and Pristine Fe_3O_4 coatings. Error bars are ± one standard deviation.

Electrochemical cycling

Rate capability measurements were conducted on the pristine and surface-treated electrodes at a series of current densities. A total of 100 cycles using sequential (dis)charge current densities of ranging from 50 to 1600 mA/g were tested for 10 cycles under each current condition. With respect to the discharge capacities the PA-Fe_3O_4 sample demonstrated the highest rate capability at all rates amongst the five Fe_3O_4 samples

In terms of the rate capability of the resulting electrodes, both PA and BA-capped systems demonstrated better performance than that of their thiol-containing counterparts (MPA and MBA) as well as the pristine Fe_3O_4 system, indicating that the thiol functional group has detrimental effect on the resulting electrode behaviors of our Fe_3O_4 system, in part due to the strong electron affinity of -SH group, which withdraws electron from Fe_3O_4. With respect to the cycling stability, it is interesting to note that although the aliphatic PA system demonstrated outstanding rate capability for the initial 100 cycles under various current densities, and good cycling stability in the extended cycles from cycle 101-200 at a low current density of 100 mA/g, when the current density increased to 400 mA/g, the aromatic BA system started to deliver more capacities and show better cycling stability due the improved charge transfer property and ion transport efficiency.

4.2.4 Conclusions

The compilation of both structural and electrochemical results showed that (*i*) the presence of a π-conjugated carbon framework within the surface-treatment agents themselves and (ii) the electron affinity of the pendant groups collectively played important roles in the resulting interfacial charge transfer and ion transport from Fe_3O_4 to the underlying carbon networks. Specifically, the short aromatic ligands without thiol group can potentially improve the electrochemical performance of the Fe_3O_4 anodes, especially during extended cycling under fast (dis)charge rates, due to the enhanced electron and ion conductivity. Due to the small volume of the ligands and the thin coating layer, the tap density can be improved when comparing to those electrodes containing large amount of carbon nanotubes or conducting polymers. Additionally, incorporating physical surface measurement techniques such as contact angle measurement and AC SECM provided insight into trends in physical properties that contributed to explanations of electrochemical cycling.

Acknowledgements

All of the work described in these studies was funded as a part of the Center for Mesoscale Transport Properties, an Energy Frontier Research Center supported by the U.S. Department of Energy, Office of Science, Basic Energy Sciences, under award #DE-SC0012673. This research used resources of beamline 5- ID, submicron resolution X-ray spectroscopy (SRX) of the National Synchrotron Light Source II, a U.S. Department of Energy (DOE) Office of Science User Facility operated for the DOE Office of Science by Brookhaven National Laboratory under Contract No. DE-SC0012704. The electron microscopy measurements used resources of the Center for Functional Nanomaterials, which is a U.S. DOE Office of Science Facility, at Brookhaven National Laboratory under Contract No. DE- SC0012704. A.A., M.R.D., and A.H.M. acknowledge the Graduate Assistance in Areas of National Need Fellowship (GAANN). E.S.T. acknowledges the William and Jane Knapp Chair in Energy and the Environment. A.C.M. acknowledges Brookhaven National Laboratory for purchase of the Scanning Electrochemical Microscope used for AC-SECM measurement.

4.3. Electrochemistry in Rechargeable Aqueous Zn-MnO_2 Batteries

The following is adapted from the following open access article distributed under the terms of the Creative Commons Attribution 4.0 License, permitting the unrestricted used of the work in any medium, provided citation:

© 2019. Wang, L., Wu, Q., Abraham, A., West, P. J., Housel, L. M., Singh, G., Sadique, N., Quilty, C. D., Wu, D., Takeuchi, E. S., Marschilok, A. C., Takeuchi, K. J., Silver Containing α-MnO_2 Nanorods: Electrochemistry in Rechargeable Aqueous Zn-MnO_2 Batteries, *J. Electrochem. Soc.*, 166 (15) A3575-A3584. DOI: 10.1149/2.0101915jes

Personal contributions: Assist in collection and data analysis of SVP data, contributions to manuscript

Dr. Lei Wang – Material synthesis (with Patrick J. West), SEM and characterization, electrochemistry, manuscript preparation.

Dr. Qiyuan Wu – SVP measurements (shown in Figure 4.10), data analysis

Lisa M. Housel – Bulk post electrochemical characterization in collaboration with Gurpreet Singh, Nahian Sadique, Patrick J. West, Daren Wu

Calvin D. Quilty – SVP measurements of charging, data analysis

4.3.1 Introduction

Rechargeable aqueous Zn/MnO_2 batteries are considered viable alternatives to lithium ion batteries for certain applications, due to both the high environmental abundance and safety considerations associated with both zinc and manganese oxide, MnO_2. Additionally, incorporating an aqueous electrolyte has the intrinsic benefit of having high ionic conductivity and non-flammability.[268-271] In traditional alkaline electrolyte systems that include zinc and manganese oxide, there are several insoluble byproducts that form on either the anode (ZnO or $Zn(OH)_2$) and the cathode ($Mn(OH)_2$, Mn_3O_4, Mn_2O_3). The formation of these products is reflected in the electrochemistry by observations of capacity fade and poor Coulombic

efficiencies during cycling.[272, 273] Recently, neutral or mild acidic aqueous electrolytes were utilized in rechargeable aqueous Zn/MnO_2 batteries to improve the functional electrochemistry.[274, 275] During (dis)charge, there have been reports showing that both Zn^{2+} and/or H^+ can (de)insert from the MnO_2 structure, including studies reporting reversible Zn^{2+} (de)intercalation from the MnO_2 structure,[269, 276, 277] and/or H^+ insertion/extraction.[274]
From a functional electrochemistry perspective, hollandite type α-MnO2 materials are of interest due to their high surface area to volume nanorod morphology, ability to accommodate a wide array of ions into their structural channels, including K^+, Ag^+, Li^+, Na^+, and Zn^{2+}, as well as its synthetic versatility.[278, 279] In terms of structure, α-MnO2 is composed of MnO_6 octahedral that form double chains that are edge and corner-sharing with adjacent double chains in the plane to form (2 x 2) tunnel structures (**Figure 4.8**, generated from reported structure parameters[280]), that can accommodate different tunnel cations.[281]

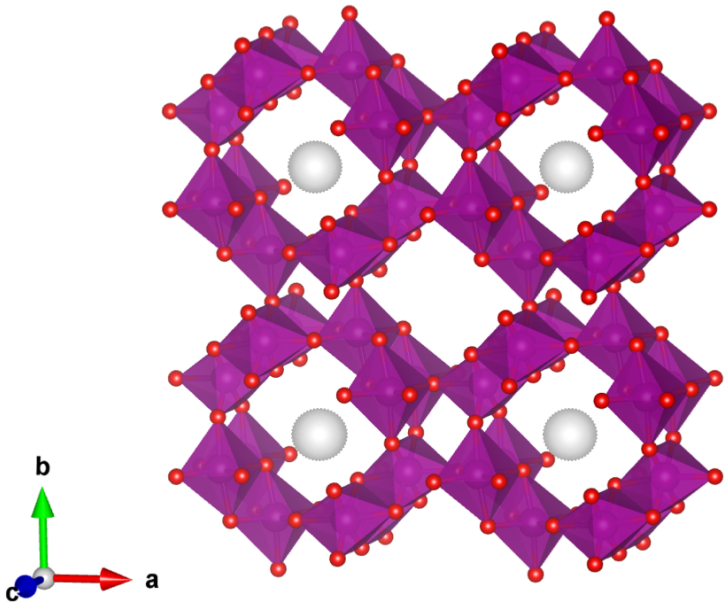

Figure 4.8. Crystal structure of α-MnO_2 showing position of the central cation, M^+, (Oxygen atoms= red spheres, Mn atoms= inside of purple octahedra)

α-MnO2 can be synthesized in various aspect ratios. Long nanofibers, previously used as a cathode material in a mild aqueous $ZnSO_4$-based electrolyte, demonstrated an operating voltage of 1.44V and a capacity of 285 mAh/g at C/3 rate. This was attributed to the chemical conversion reactions between α-MnO2 and H^+.[268] Hydrothermal preparations of nanofibers of α-MnO_2 were previously reported to reduce via a Zn^{2+} insertion mechanism with the reversible formation of a layered manganese oxide birnessite phase.[282] A microemulsion synthesis of α-MnO_2 material delivered a capacity of 210 mAh/g at 0.5C,[269] while in a separate study, α-MnO_2 nanorods delivered an initial capacity of 233 mAh/g and gradually faded to 147 mAh/g in cycle 15 at a current density of 83 mA/g.[277]

Recently, Ag^+ stabilized hollandites, ($Ag_xMn_8O_{16}$) have been extensively explored as cathode materials in both Li- ion[281, 283] and Na- ion[146, 281] based nonaqueous battery systems. Silver ions are located in the α-MnO_2 tunnels to stabilize the tunnels. It has been observed that the presence of Ag^+ reduces both the *a* and *b* dimensions of the unit cell when compared to the similar material without the metal cation located in the tunnel.[281, 284] Ag^+ hollandite exhibits formation of conductive silver (Ag^0) nanoparticles upon discharge through a reduction-displacement reaction.[146,281] This presence of reduced silver has been correlated to reduced cell resistances and improved electronic conductivity.[285] Interestingly, previous studies in nonaqueous battery systems[146, 286] have indicated a notable difference between the lithation and sodiation processes of the $Ag_xMn_8O_{16}$ materials. For example, a significant decrease in charge transfer resistance after 1.5 electron equivalents per $Ag_{1.2}Mn_8O_{16}$ formula unit of Na ion insertion was observed, whereas a gradual increase in impedance with observed with lithiation.[146] The impedance decrease upon sodiation coincided with the formation of silver metal during the early discharge process. In the lithium system, Ag metal was only detected after six electron equivalents (6 e.e.) of lithiation.[286] The earlier onset of silver metal in the sodiation process further supports the observations of a decrease in impedance of the sodiation system in comparison to lithiation. Given the strong electrochemical foundation of $Ag_xMn_8O_{16}$ (where x = 1.2 to 1.6) in batteries containing organic electrolytes, it is worthwhile to investigate whether the positive attributes of Ag^+ stabilized hollandite translate to other electrochemical systems, specifically the aqueous zinc system.

In relation to zinc based aqueous systems, two recent reports have evaluated the role of zinc intercalation in vanadium oxide based cathodes with the inclusion of an additional metal cation (Ag^+ or Cu^{2+}).[287, 288] In the case of $Zn/Ag_{0.4}V_2O_5$ containing cells, a combination of a displacement and intercalation mechanism (CDI) was reported for Zn^{2+} insertion. The combination displacement intercalation, CDI, can be described as providing two pathways for zinc insertion. In the displacement process, the transition metal cation (i.e. Ag^+) would be replaced by Zn^{2+}. In the intercalation process, the Zn^{2+} would (de)insert into vacant sites in the V_2O_5 host structure. Displacement of Ag^+ by Zn^{2+} was demonstrated by the appearance of a $Zn_2(V_3O_8)_2$ phase upon discharging to 0.4V (vs. Zn/Zn^{2+}), and a disappearance of this phase upon charging to 1.4V. The observed reversible peak was attributed to the Zn^{2+}/Ag^+ displacement reaction during Zn^{2+} insertion/extraction, which also resulted in the formation of the reduction of silver from Ag^+ to Ag^0, forming a conductive network of Ag^0.[287]

In aqueous Zn/copper pyrovanadate ($Cu_3(OH)_2V_2O_7 \cdot H_2O$) cells, a reduction-displacement mechanism was reported to stem from the insertion of Zn^{2+} to the reduction of Cu^{2+} to a mixture of Cu^0 and Cu^+, as well as a partial reduction in the vanadium oxidation state from V^{5+} to V^{4+}. Upon charging to 1.4 V, the majority of the Cu^0/Cu^+ was oxidized back to Cu^+/Cu^{2+}, and the vanadium that underwent reduction to V^{4+} was oxidized back to V^{5+}. During discharge, the insertion of Zn^{2+} lead to a new phase of zinc vanadate ($Zn_{0.25}V_2O_5 \cdot H_2O$), which was confirmed by ex situ XRD and HRTEM measurements. It was observed that the Zn^{2+} insertion was concurrent with the reduction of Cu^{2+} to mixed Cu^+/Cu^0) which was confirmed by ex situ XPS and HRTEM/EDS. This noted preference for the formation of Cu^0 nanoparticles to form on the surface. While generally, reversibility was observed during subsequent charging cycles, there still remained some Zn^{2+} that did not extract fully, and this was attributed as the underlying reason for the observed capacity fade.[288]

Additionally, implying mixed vanadium valence cathodes and incorporating potassium into the Mn_8O_{16} structure were also shown to improve charge transport (mixed vanadium valence) or reduce manganese dissolution in ZIB (inclusion of potassium). The mixed valence state vanadium cathode, (V^{4+}-V_2O_5), was prepare initially from VOOH, then used in aqueous Zinc cells with 2M $ZnSO_4$ electrolyte. The presence of the lower vanadium oxidation state (V^{4+}) was attributed to the increased electrochemical activity by reducing polarization and enhancing charge transport when compared to the single valance state V_2O_5 cells,[289] while the incorporation of potassium into Mn_8O_{16} with oxygen defect sites was also shown to suppress manganese dissolution.[271]

No prior reports at the date of the publication (to the best of the authors knowledge) utilized $Ag_xMn_8O_{16}$ compositions as cathode materials for rechargeable aqueous Zn/MnO_2 batteries. $Ag_{1.5}$Mn8O16 nanorods prepared using a facile reflux method were utilized as a cathode materials for Zn/MnO_2 batteries in $ZnSO_4$ based electrolyte. The impact of the tunnel Ag^+ ions on the resulting electrochemistry was probed using a variety of complimentary characterization techniques. Below the utilization of scanning probe instrumentation, mainly Scanning Vibrating Probe (SVP) will be highlighted in the role of silver in an aqueous Zn/α-MnO_2 cells.

4.3.2 Experimental

Synthesis and characterization of $Ag_{1.5}Mn_8O_{16}$

$Ag_{1.5}Mn_8O_{16}$ nanorods were synthesized by reflux methods following previous reports.[281, 290] Briefly, aqueous $MnSO_4$ was added dropwise to a solution of $AgMnO_4$ and held under reflux for 15 hours. The product was collected, washed with DI H_2O and dried. Prior to use, the material was heat treated at 300°C for 6 hours in air. Additional experimental details can be found in the full report.[291]

Electrochemical Measurements

Electrodes were prepared by combining $Ag_{1.5}Mn_8O_{16}$, carbon and polyvinylidene difluoride (PVDF) in a weight ratio of 7:2:1 in N-methyl-2-pyrrolidone. Slurries were cast onto stainless steel foil with an average active mass loading of ~ 1.5mg/cm^2. Coin cells were constructed using the fabricated $Ag_{1.5}Mn_8O_{16}$ electrodes, glass fiber separators and zinc foil with 2M zinc sulfate electrolyte.

Scanning vibrating probe (SVP) is an alternating current (AC) technique which measures the potential difference between the two end-positions of the vibrating probe (across vibration amplitude) due to ionic current flow in the electrolyte solution.[292-295] The SVP experiment was conducted using a commercially available instrument (Bio-Logic M470) in 0.5M $ZnSO_4$ (*aq.*), with a three electrode set up, including an Ag/AgCl reference electrode, Pt counter electrode, and the $Ag_{1.5}Mn_8O_{16}$ coating as the working electrode. (**Figure 4.9**) The working electrode was prepared from 70/20/10 (active/carbon/PVDF) on a stainless steel foil current collector which was affixed to a Bio-Logic cell. Since sample lift or sample tilt could affect the measurement by changing the probe-sample distance, care was taken to level the sample on the cell and checked using a spirit level. The input voltage (V_{in}) of the electrometer was connected to the counter electrode to provide a stable potential in which the potential difference was measured in the electrolyte solution of 0.5M aqueous zinc sulfate ($ZnSO_4$).

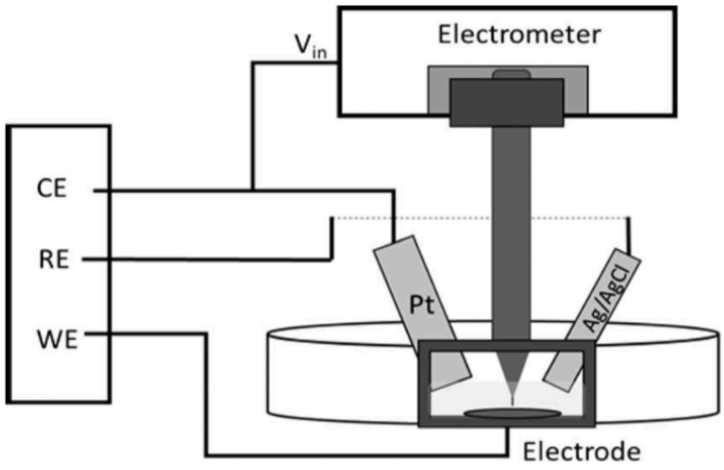

Figure 4.9. Set up of Scanning vibrating probe, (SVP) including positions of counter (CE), reference (RE) and working (WE) electrodes.

Constant potential was applied directly to the working electrode followed by SVP measurement. This methodology enabled successive reduction or oxidation steps with subsequent mapping without changing the sample probe orientation. Constant potential measurements were carried out for 10 minutes at 0.8V and 0.6V (v. Zn/Zn^{2+}) followed by an SVP measurement after each reduction. SVP measurements were performed on a scan area up to 2mm by 4mm using a 25 μm step size at a scanning velocity of 1000 μm/s with a line delay of 2 seconds. The constant potential-SVP measurements were performed sequentially without changing the electrode sample or the probe-sample distance. The probe-sample distance utilized for all measurements was ~100 μm, with a vibration amplitude of 30 μm.
Post-electrochemical testing analysis of $Ag_{1.5}Mn_8O_{16}$ was conducted using scanning electron microscopy and energy dispersive X-ray spectroscopy (SEM-EDX).

4.3.3 Results and Discussion

Initial characterization of the material was verified by combination of X-ray diffraction, ICP-OES and thermogravimetric analysis to arrive at a phase pure pattern that was consistent with previous reports of silver hollandite.[296] Crystallite size determination was conducted using the Scherrer equation to the (211) peak at 37° 2-theta, yielding a crystallite size of 15 nm.[297] ICP-OES characterization provided information on the ratio of silver to manganese, yielding a ratio of 1.46:8 (Ag:Mn). For oxygen determination, TGA analysis was used following a previously reported method.[298-300] TGA results denoted a small mass loss leading to an oxygen deficiency of 0.04 stoichiometric oxygen, yielding a formula of $Ag_{1.5}Mn_8O_{15.96.}$ For simplicity, $Ag_{1.5}Mn_8O_{15.96}$ is referred to as $Ag_{1.5}Mn_8O_{16}$.

Galvanostatic cycling for two (dis)charge cycles showed a difference in voltage plateaus between the first discharge and second discharge. In the first cycle, (at 50 mA/g), a long plateau was observed at ~ 1.27V, which in the second cycle, there were two distinct plateaus at 1.34V and 1.42V. The discharge capacity of the second cycle (at the same rate of 50 mA/g) was less than half that of the discharge capacity of cycle 1. The difference in observed voltage plateau between the first and the second discharge can be attributed to potentially morphology changes in the MnO_2 material.[268] The discharge plateaus observed have been previously assigned in the literature as either proton conversion (associated with plateau I at 1.40V) or Zinc intercalation

(plateau II, 1.34V) causing possible morphology change of the MnO_2 during electrochemical cycling.[155, 268]

To probe the role of Ag^+ in the $Zn/Ag_{1.5}Mn_8O_{16}$ cells, cells containing Zn metal and 2M $ZnSO_4$ electrolyte were discharged to several voltages: 1.4, 1.2, 1.0V, then charged to 1.6, 1.8V (all v. Zn/Zn^{2+}) at a current density of 50 mA/g and held at each potential for 2 hours. Electrochemical impedance spectroscopy was obtained for the pristine electrode and samples discharged to 1.4V, 1.0V and charged to 1.8V. Initially, there was a slight increase in the charge transfer resistance on the 1.4V discharged sample, and this was attributed to a small amount of Ag^0 being displaced with such a minimal discharge (~ 1mAh/g). However, during the subsequent discharge to 1.0 V, there was a large reduction in charge transfer resistance to less than half of the value of the pristine electrode. Upon charging to 1.8V, there was a notable increase in impedance to above that of the pristine.

The formation of silver metal through a reduction-displacement reaction has been previously observed during lithiation of silver vanadium phosphorous oxide, $Ag_2VP_2O_8$.[276, 301] As part of the discharge process, the Ag^+ is reduced to Ag^0, which has been reported in detail as to the size of the silver metal particles formed, which was dependent both on the electrode composition as well as the discharge conditions. Since silver metal deposit size was dependent on both the composition and discharge conditions of the cells, it is probable that the size of silver metal deposits can be impacted by experimental conditions.

Scanning vibrating probe (SVP), also referred to as scanning vibrating electrode technique (SVET), was used to comparing a pristine $Ag_{1.5}Mn_8O_{16}$ electrode to electrodes reduced under applied potentials of 0.8V and then 0.6V vs. Zn/Zn^{2+}. A typical SVP output is represented in terms of the potential difference (V_{pp}) across vibration amplitude (peak to peak amplitude, A_{pp}) in relation to the current flux density along the z axis (j_z), and including the solution conductivity, *k* following Ohm's law, as shown in Equation 4.3-4.[302]

$$V_{pp} = j_z \left(\frac{A_{pp}}{k}\right) \qquad \textit{Equation 4.3-4}$$

Therefore the current density, j ($\mu A/cm^2$) can be calculated by obtaining the measured electric potential (ΔV), solution conductivity, (k), and vibration amplitude, d (cm) as shown in **Equation 4.3-5**. [303]

$$j = -\Delta V \frac{k}{d} \qquad \textit{Equation 4.2-5}$$

The above makes the assumption that the electric field around the probe is constant.

Obtained SVP maps over the $Ag_{1.5}Mn_8O_{16}$ electrodes are shown in **Figure 4.10a-c**, showing a pristine electrode (**4.10a**), electrode after discharging to 0.8V (vs. Zn/Zn^{2+}) (**4.10b**), and after discharging to 0.6V (vs. Zn/Zn^{2+}), (**4.10c**). The sample-probe distance was held constant throughout successive applied potentials and SVP mapping measurements. A consistent scale was used for all images. A lock-in amplifier demodulates the AC signal from the electrometer. This demodulation yields obtained values that represent a DC voltage ,which is proportional to the vibrating probe signal. Therefore, an increasing DC voltage would imply an increasing current density along the x axis of the probe vibration as shown in Equation 4.3.4. In **Figures 4.10a-c** this increasing current density would correlate to the increasing red areas in the SVP maps, which increases in area and intensity when transitioning from the pristine electrode, to a discharged electrode (to 0.8V, then to 0.6V). In the pristine sample (**Figure 4.10a),** there is a small variation in signal that was observed mainly near the right edge over the scanned area, suggesting generally good uniformity of the electrode sample. After applying a potential

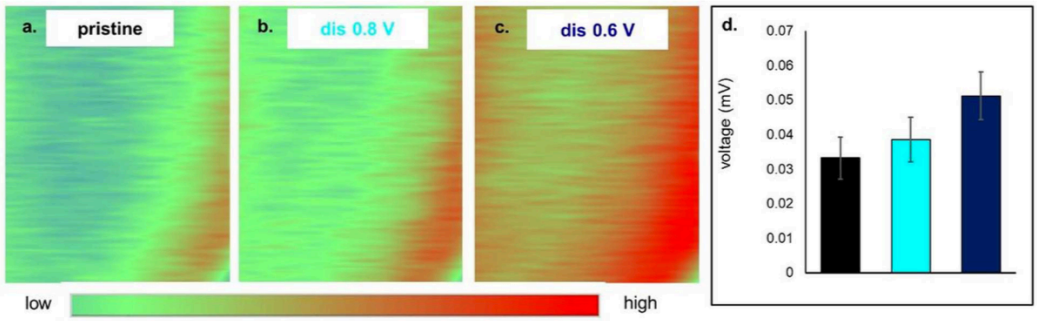

Figure 4.10. a-c) Scanning vibrating probe measurements and corresponding histogram (d) for $Ag_{1.5}Mn_8O_{16}$ electrodes: a. pristine, discharged to b. 0.8V, and c. 0.6V (vs. Zn/Zn^{2+}).

equivalent to 0.8V(vs. Zn/Zn^{2+}), the overall intensity increased, as shown in **Figure 4.10b**. Additionally, the signal continued to increase in intensity upon additional electrochemical reduction to the applied potential of 0.6V as shown in **Figure 4.10c**. The individual SVP data were aggregated for each sample map, and the average and standard deviation in DC voltage were found to be notably different for the pristine and 0.6V conditions as shown in **Figure 4.10d**. To further evaluate changes in conductivity upon discharge of the pristine sample, the same composition electrode was housed in a coin cell with $ZnSO_4$ electrolyte, and discharged to the same potentials as in the SVP experiment, using a constant current discharge followed by 2 hour potential holds. LABE SEM images were obtained of both the pristine and discharged electrodes after de-crimping. By SEM, the pristine electrode was shown to be silver particle free while small and dispersed Ag particles were observed in the sample discharged to 0.8V which then transformed into larger, irregularly shaped particles when discharged to 0.6V.

Separate SVP measurements were obtained over different applied potentials, corresponding to discharge and charge, including 0.8V, 0.6V (discharge) and 1.8V (charge) (vs. Zn/Zn^{2+}). For this set of images, the sample-probe distance remained the same throughout the series of mapping measurements, and a consistent scale was used for all images. After applying a potential of 0.8V (vs. Zn/Zn^{2+}), the overall intensity increased. After further reduction by applying a potential of 0.6V (vs. Zn/Zn^{2+}), the intensity of the signal decreased somewhat, but still remained higher than that of the pristine electrode. To evaluate mapped areas, during potential equivalents of charging, the electrode was oxidized at 1.8V, and a dramatic drop in intensity was observed. To determine the quantitative change in DC voltage from the mapped areas, the average with one standard deviation was plotted. While the average intensities showed an increase in potential upon discharge, and a discharging during the following charge step, the high standard deviation suggested some level of variation of the large map area of 2000 x 2000 μm. To alleviate variation possibly attributed to the large sampling area, the average and standard deviation was determined for a 500 by 500 μm section of each map. This sectioning clearly shows the significant change between each sample condition. The increase in intensity upon reduction (discharge), is consistent with the conductivity increase due to formation of silver metal. The decrease upon charge suggests the formation of a more insulating species. Figures describing the changes in discharge and charge can be found in the full reference.[291]

X-ray diffraction (XRD) was collected ex situ on pristine electrodes and electrodes reduced to 1.0 V (vs. Zn/Zn^{2+}), as well as those reduced to 1.0V, followed by a charge to 1.8 V. The XRD of the pristine material was representative of $Ag_{1.3}Mn_8O_{16}$ pattern. After discharge to 1.0V, the dominant reflections corresponding to the (001), (002), and (003) reflections of the osakite salt $ZnSO_4(Zn(OH)_2)_3$, which was similar to previous reports.[268] Silver metal formation was confirmed by the presence of peaks that corresponded to the (111) and (220) reflections of cubic Ag^0. Upon charge, the (220) and (310) reflections corresponding to silver hollandite are present, but there were no reflections observed correlating to osakite or Ag^0 in the charged electrode. By ex-situ XRD, further evidence is provided that the formation of Ag^0 is formed upon discharge to 1.0 V, and reversibly oxidized to Ag^+ upon charging to 1.8 V.

4.3.4 Conclusions

Synthesized silver hollandite nanorods with a composition of $Ag_{1.5}Mn_8O_{16}$ underwent reduction and subsequent oxidation an aqueous $ZnSO_4$ electrolyte, and was reported for the first time. Combining multiple characterization techniques including scanning electron microscopy (SEM), Scanning Vibrating Probe measurements (SVP), X-ray diffraction, and X-ray absorbance spectroscopy (EXAFS) provided insight into the role of silver upon discharge and subsequent charge of the electrode. In contrast to non aqueous systems, where irreversible formation of silver metal was observed, in aqueous systems, an observed oxidation of Ag^0 to Ag^+ was observed across characterization platforms upon charging to 1.8V. While traditional characterization techniques, namely XRD and SEM are critical in assessing compositional and morphological characterizations of materials, the incorporation of SVP can provide information on a scale length different from that of the aforementioned characterizations. Additionally, since the SVP technique is a surface measurement, correlation between bulk measurements such as XRD and surface oriented scanning probe techniques can additionally provide insight into whether an observation is a localized or bulk phenomenon.

Acknowledgements

Material synthesis and characterization of the pristine samples was supported as part of the Center for Mesoscale Transport Properties, an Energy Frontier Research Center, supported by the U. S. Department of Energy, Office of Science, Basic Energy Sciences, under award #DE-

SC0012673. The aqueous electrochemistry studies were supported by the Department of Energy, Office of Electricity, administered through Sandia National Laboratories, Purchase Order #1955692. ACM acknowledges Brookhaven National Laboratory for support of the SVP research. Experimental characterizations were carried out in part at the Center for Functional Nanomaterials, Brookhaven National Laboratory, an Office of Science User Facility, which is supported by the U. S. Department of Energy, Office of Basic Energy Sciences, under Contract. No DE-SC0012704. The full publication used beamline 5-ID (SRX) and 7-BM (QAS) of the National Synchrotron light Source II, a U. S. Department of Energy (DOE) Office of Science User Facility operated for the DOE Office of Science by Brookhaven National Laboratory under Contract No. DE-SC0012704. The authors express their sincere gratitude to beam line scientists Steven Ehrlich (QAS), Juergen Thieme (SRX) and Andrew Kiss (SRX) for their assistance. EST acknowledges support from the William and Jane Knapp Chair for Energy and the Environment.

4.4. Electrochemical Insights in Polymorphic Vanadium Oxide, VO_2

Reprinted (adapted) with permission from:

Investigation of Conductivity and Ionic Transport of VO_2(M) and VO_2(R) via Electrochemical Study, Housel, L., M., Quilty, C. D., Abraham, A., Tang, C. R., McCarthy, A. H., Renderos, G. D., Liu, P., Takeuchi, E. S., Marschilok, A. C., Takeuchi, K. J., *Chem. Mater.,* 2018, 30, 217535-7544. Copyright © 2018, American Chemical Society.

Personal Contributions: Contributed to initial project development and preps for materials synthesis and calcination. Developed methodology for generating robust material (without addition of binder or carbon additives) for testing in cell configuration, and contributions to manuscript draft.

Acknowledgement of collaboration:

Lisa M. Housel – Contributed to initial project development, synthesis, temperature dependent XRD measurements, electrochemistry and manuscript draft.

Calvin D. Quilty – Temperature dependent XRD measurements, detailed Rietveld refinements at each temperature interval,

Christopher R. Tang – Temperature dependent impedance fitting and analysis, electrochemistry

Allison H. McCarthy – Temperature dependent impedance fitting and analysis, electrochemistry

Genesis D. Renderos- Temperature dependent impedance fitting and analysis, electrochemistry

Dr. Ping Liu- Density Functional Theory calculations on lithiation studies of VO_2

4.4.1 Introduction

The transition metal vanadium has proven useful in a variety of applications due to access of multiple oxidation states and coordination geometries where the applications range from energy related to catalysis[304, 305] to biological applications[306-310]. Specific experimental and theoretical investigations have probed the VO_2 metal to insulator transition, which is an intriguing temperature based phase transition.[311, 312] At 68ºC, VO_2 undergoes a structural change from a monoclinic [VO_2(M)] to rutile [VO_2(R)] phase, which is accompanied by an electrical conductivity increase of several orders of magnitude.[313, 314] The changes to strain,[315, 316] electric field,[317] and optical excitation[318] resulting from this phase transition have led to interest in thermo/electrochromatics and sensing applications.[319, 320] Previous literature reports have demonstrated efforts to control the transition temperature through controlled thin film synthesis[321], doping with tungsten[322, 323] or titanium[324], applying internal/external stress[325, 326], or changing microstructure and controlling crystallite size.[327, 328] Other studies are centered on understanding the electronic and structural aspects of the phase transition at the microscopic level [319], made possible by advanced characterizations such as ultrafast electron diffraction[329] X-ray absorption spectroscopy[330] and nanoscale imaging[331, 332].

Additionally, VO_2 and other vanadium oxides are recognized as potential lithium ion battery electrodes due to their high theoretical energy density, which arises from the variable oxidation state of vanadium.[333] Studies have used the VO_2(B) polymorph as a cathode material[334-337] due to its high reported specific capacity (325 mAh/g)[338] relative to VO_2(M) (<200 mAh/g) for one lithium equivalent at room temperature.[339, 340] VO_2(B) has edge-sharing VO_6 octahedra bilayers, which provide structural stability and facilitate lithium ion diffusion, while VO_2(M) and VO_2(R), have corner-sharing VO_6 octahedra that form a tunneled structure and result in anisotropic lithium ion diffusion**.**

Recently, VO_2(M) nanorod electrodes were fabricated that preferentially expose the (002) facet to improve the kinetics of lithium ion diffusion. Compared to bulk VO_2(M) nanoparticle electrodes, the oriented VO_2(M) electrode delivered three times more reversible capacity vs. Li/Li^+ (320 mAh/g) and approached the specific capacity of VO_2(B) electrodes (325 mAh/g).[341] Other approaches to improve VO_2(M/R) electrodes include harnessing the higher electrical conductivity of the VO_2(R) phase. Prior theoretical studies using *ab initio* calculations indicate the electronic structure is not significantly affected by the insertion of lithium ions at the initial stage, suggesting electrical differences between VO_2(M) and VO_2(R) may be observable in an electrochemical cell.[342] However, the VO_2(R) phase is not stable at room temperature; therefore, accessing the VO_2(R) phase in an electrochemical cell must be done at temperatures above the VO_2(M) to VO_2(R) transition temperature.

This section will briefly describe the electrical and structural changed that occur during the VO_2(M) to VO_2(R) transition as a function of temperature. Additional information, including detailed Rietveld refinement at each temperature interval, impedance studies with various cell configurations, electrochemistry predictions upon lithiation can be found fully described in the full reference.[343] While previous literature has evaluated structural transitions, the linking of the phase transition to behavior in electrochemical cycling had previously not been reported (to the authors' best knowledge) at the date of publication. The incorporation of VO_2(M) into electrochemical cells enabled the determination of phase transition from the application of heating, impedance, and functional electrochemistry. The cell was studied systematically, in different configurations to identify the contributions of the active material itself, as well as the contribution of the addition of lithium.

Through pulse testing, understanding of electron and ion transfer phenomena that occur during the VO_2(M-R) phase transition in an electrochemical cell were elucidated as a function of temperature. Complementary density functional theory calculations were performed to rationalize the experimentally measured intercalation voltages and a possible Li-induced Li_xVO_2(M) to Li_xVO_2(R) phase transition. This provides a foundation for investigating charge transport properties in polymorphic materials and sets a precedent for understanding the impact of phase changes on electrochemistry in a complex energy storage system.

4.4.2 Experimental

Synthesis

Monoclinic vanadium(IV) oxide (VO_2(M)) was synthesized using an approach following a previous report.[344] Briefly, vanadium pentoxide (Avantor®) and oxalic acid (Spectrum Chemicals) reagents, in a 1:4 molar ratio, were reacted hydrothermally at 220°C. The precursor material was then calcined at 750°C under N_2 to generate VO_2(M).
Additional experimental details can be found in the published manuscript.[343]

4.4.3 Results and Discussion

Characterization

The VO_2(M)[345] M2[346], and R[347]) structures, shown in **Figure 4.11**, can be described as a chains of edge sharing VO_6 octahedra where the chains are connected by corner linkages. VO_2(M2) can be viewed as an intermediate of the VO_2(M) and VO_2(R) transition.
In VO_2 (M1) there is a single Vanadium species and Vanadium atoms are aligned, whereas in the M2 phase, there are two Vanadium sites in alternating rows, and in VO_2(R), there is a single Vanadium site with staggered layers of VO_6 octahedra. Synchrotron powder X-ray diffraction data was collected at room temperature, 48, 57, 61, 63, 70, 72, and 75°C,. The weight percentages of VO_2(M) and VO_2(R) as a function of increasing temperature are shown in **Figure**

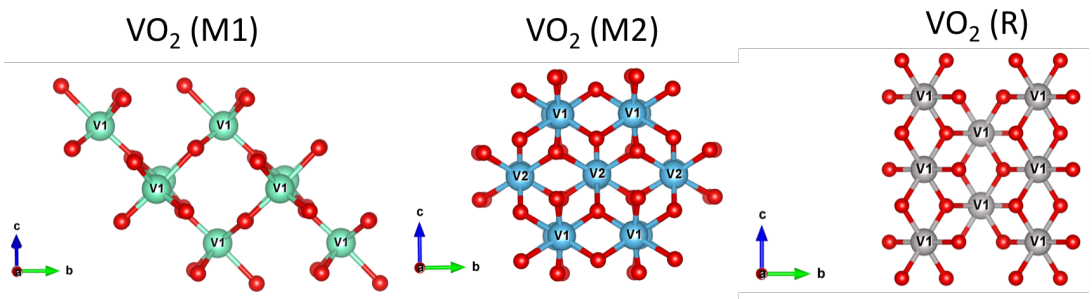

Figure 4.11. Crystallographic structures of VO_2 (M1), (M2) and (R) with labels (V1, V2) showing distinct crystallographic vanadium sites.

4.12 based off of extensive Rietveld refinements by C.D.Q. (noted in Acknowledgement of Collaboration). VO_2(M) is the primary phase at room temperature, confirming that VO_2(M) is produced from the hydrothermal synthesis.[345] A small percentage of V_2O_5 is noted (0.7%) and remains present throughout the temperature series (0.7-0.8%). Upon heating to 48°C, VO_2(M) is

the dominant phase (99.2%). At 57°C, VO_2(M2) contributes 1.6% to the phase composition, which corresponds to a slight decrease in the VO_2(M) weight percent.

At 61°C, the weight percent of VO_2(M2) increases (2.5 %) as VO_2(M) decreases (96.6%). At 63°C, The VO_2(M2) weight percent levels (2.6 %), VO_2(M) decreases (95.5 %), and VO_2(R) appears in small quantity (0.8 %) for the first time. A notable compositional change occurs between 66-70°C (**Figure 4.12**), with VO_2(R) increasing, and then becoming the majority phase. By XRD, the VO_2(M-R) transition is observed by a peak shift from 4.24˚ to 4.22˚, corresponding to the (011) and (110) planes for VO_2(M) and VO_2(R), respectively. The VO_2(M-R) conversion temperature range of 66-70°C is consistent with previous reports. [348, 349]. It is noted that when the material is heated past the transition temperature and allowed to cool again; the VO_2(M-R) transition down-shifts slightly to 64-61˚C.

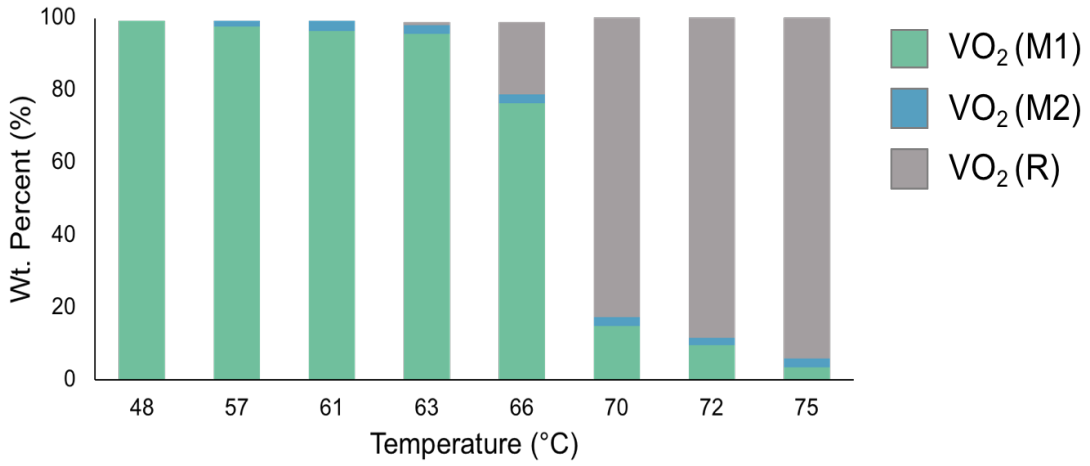

Figure 4.12. Relationship of weight percentage of VO_2 phases upon heating from 48-75°C.

Electrochemistry during phase transition

A main outcome of the VO_2(M-R) transition is the reported change in material conductivity and subsequent effects on electrochemistry. Initially, multiple types of cell configurations were tested, including a one electrode cell (only containing the VO_2 electrode and a Li^+ containing electrolyte) and a two electrode cell, containing lithium metal anode and VO_2 as the cathode. As temperature increased, the semi-circle of the Nyquist plot decreased, with the

most dramatic reduction observed at 65-68°C. The dramatic change in resistance at 68°C agreed with x-ray diffraction data, suggesting a change from VO_2(M) to VO_2(R). X-ray diffraction results also showed that the evolution of VO_2(R) occurred over a series of temperatures as opposed to an instantaneous conversion at 68°C, where it was noted that below 61°C, only VO_2(M) was present and at 75°C, VO_2(R) contributed over 90% to the material present. The impedance of a lithium-VO_2 two electrode cell was measured as a function of temperature to determine the impact of the VO_2(M) to VO_2(R) transition on a full cell. As temperature increased, the Nyquist plot semi-circle decreased, with a noticeably larger reduction at 65-68°C. Changes in R_{ohmic} and R_{ct} were also noticeable, suggesting the VO_2(M) to VO_2(R) transition occurred upon incorporation into a two electrode cell. Similar to the one electrode cell, the two electrode cell demonstrated its most significant change in resistance between 65-68°C, suggesting the VO_2(M) to VO_2(R) transition occurred at this temperature and was detectable in the presence of a lithium anode.

Galvanostatic Intermittent Titration Technique (GITT) was employed to test the 50°C and 70°C cells utilizing a smaller current and longer discharge time. Throughout the discharge, the 50°C cell demonstrated a lower potential at each depth of discharge. The difference in potential between the 50°C and 70°C cell was most significant early in the discharge. In addition, the 70°C cell delivered more capacity (245 mAh/g) than the 50°C cell (194 mAh/g) upon completion of the GITT test. GITT tests as well as additional pulse testing demonstrated that the 50°C cell has a lower operating potential (higher internal resistance) at each depth of discharge relative to the 70°C cell. Thus, the pulse and GITT tests support the initial hypothesis that conversion to VO_2(R) can impact the functional electrochemistry of VO_2.

4.4.4 Conclusions

Through a combination of synchrotron X-ray diffraction, electrochemical impedance spectroscopy, and density function theory, the electrochemistry of the Li_xVO_2 system as a function of temperature has been rationalized. The percentages of VO_2(M) and VO_2(R) phases as a function of increasing temperature were determined quantitatively using synchrotron powder X-ray diffraction data coupled with Rietveld refinement. At room temperature VO_2(M) is the dominant phase present. At 70°C, VO_2(R) was observed to be the dominant phase present and at 75°C it represented 94% of the total material. Electrochemical impedance spectroscopy was

used to interrogate the material as a function of temperature where a dramatic decrease in resistance was noted at 68°C consistent with the phase change from VO_2(M) to VO_2(R). The impact of this phase change on the electrochemical function of lithium anode electrochemical cells was determined through pulse tests at 50°C and at 70°C. Ohmic resistance determined from the voltage drop at the leading edge of the pulse was used to compare the performance and shows that the cells tested at 70°C demonstrated lower ohmic resistance than those tested at 50°C consistent with the increased electrical conductivity associated with the VO_2(M) to VO_2(R) transition.

Acknowledgement

This work was supported as part of the Center for Mesoscale Transport Properties, an Energy Frontier Research Center supported by the U.S. Department of Energy, Office of Science, Basic Energy Sciences via grant #DE-SC0012673. This research used resources, specifically beamline 28-ID-2, of the National Synchrotron Light Source II, a U.S. Department of Energy (DOE) Office of Science User Facility operated for the DOE Office of Science by Brookhaven National Laboratory under Contract No. DE-SC0012704. DFT calculations were performed using computational resources at the Center for Functional Nanomaterials at Brookhaven National Laboratory, an Office of Science User Facility under Contract No. DE-SC0012704. The authors thank Diana Lutz for assistance with data analysis. AA acknowledges support from the Graduate Assistance in Areas of National Need (GAANN) Fellowship. EST acknowledges support as the William and Jane Knapp Chair of Energy and the Environment. The authors declare no competing financial interests.

Chapter V

Examining the lithiation of potassium hollandite surfaces

5.0 Introduction

Theoretical calculations of materials can provide insight into identifying target materials with particular properties that can then subsequently be tested experimentally. Additionally, Density Functional Theory (DFT), can offer insight into repeated experimental observations that may be challenging to explain by purely chemical means. By comparing the calculated energy of a range of structures, trends can be observed in regards to thermodynamic stability, which can provide insight when developing a particular synthetic material.

The goal of many approaches in quantum chemistry is to approximate the solution of the time-independent, non-relativistic Schrödinger equation, where:

$$\widehat{H}\psi(r_i, R_I) = E\psi(r_i, R_I) \qquad \textit{Equation 5-1}$$

Where $\widehat{H}$ is the Hamiltonian operator of a many-body system consisting of *m* nuclei and *n* electrons in the absence of magnetic or electronic fields. ψ represents the wavefunction which depends on both electronic coordinates, r_i, and nuclear coordinates, R_I. The Eigenvalue is represented by E, which provides the energy of the many-body ground state system. The Hamiltonian operator, $\widehat{H}$, represents the total energy, by including several different terms, corresponding to the kinetic energy (Terms I,II) of electrons (I) and nuclei (II). The remaining terms (III-V) represent the attractive electrostatic interactions between the nuclei and the electrons (III), and the repulsive potential due to the electron-electron interaction (IV), and the nucleus-nucleus interactions (V).[83]

Equation 5-2

$$\begin{matrix} & \text{I} & & \text{II} & & \text{III} & & \text{IV} & & \text{V} \\ \widehat{H} = & -\frac{1}{2}\sum_{i=1}^{n}\nabla_i^2 & -\frac{1}{2}\sum_{A=1}^{m}\frac{1}{M_A}\nabla_A^2 & -\sum_{i=1}^{n}\sum_{A=1}^{m}\frac{Z_A}{r_{iA}} & +\sum_{i=1}^{n}\sum_{j>i}^{n}\frac{1}{r_{ij}} & +\sum_{A=1}^{m}\sum_{B>A}^{m}\frac{Z_A Z_B}{R_{AB}} \end{matrix}$$

Where terms A and B run over *m* nuclei, while *i* and *j* denote *n* electrons in the system, and M_A is the mass of nucleus A in multiples of the mass of an electron. Then following the Schrödinger equation (Equation 5-1), the Eigenvalue, E_{total} is the sum of the energies of the Hamiltonian, $\widehat{H}$ operating on the wavefunction, ψ, where:

$$E_{total} = I\ (T_e)\ + II\ (T_n)\ + III\ (V_{ee})\ + IV\ (V_{nn}) + V\ (V_{en})$$

Due to the multiple components that make up the contribution to the total energy $E_{tot,}$ approximations are implemented to enable solving the Schrödinger equation for a system that is greater than an one atom, one electron system.

The Born-Oppenheimer approximation[350] sets the nuclei to be fixed in space (due to the nuclei moving slower than any electron), which yields a kinetic energy of zero, and a constant term for the potential energy due to nuclei-nuclei repulsions. This reduces the total Hamiltonian to the electronic Hamiltonian, as shown below:

$$\widehat{H} = -\frac{1}{2}\sum_{i=1}^{n}\nabla_i^2 - \sum_{i=1}^{n}\sum_{A=1}^{m}\frac{Z_A}{r_{iA}} + \sum_{i=1}^{n}\sum_{j>i}^{n}\frac{1}{r_{ij}} \qquad \textit{Equation 5-3}$$

Then the total energy, is then the sum of $E_{electron}$, and a constant nuclear repulsion term $E_{nuc,}$ which is a constant. While the Born-Oppenheimer approximation reduces the degrees of freedom from 3m + 3n to 3n, this still consisted of a multi electron problem that presented challenges for computational purposes. To further simplify the calculations, further approximations were developed. The Hatree-Fock approximation is based on the wave function, where the basis of the approximation was to split the overall wave function, and to represent the coloumb and exchange interaction by an average potential. However, this can lead to overestimation of the total energy of a multi electron system is a multiple variable system (consisting of 4n, where 3n is spatial, 1n is spin).

Density Functional Theory, (DFT) is a widely used theoretical approach for calculating the ground state energy of a system.[82] DFT provides the total energy of a system by relating the ground state energy to the electron density, ρ resulting in the following equation, where, and in Kohn-Sham formalism, the total energy, E, is given by:[83]

$$-\nabla^2 + V_H[\rho(\boldsymbol{r})] + V_N(\boldsymbol{r}) + V_{XC}[\rho(\boldsymbol{r})])\psi_i(r) = E_{i\psi i}(\boldsymbol{r}) \qquad \textit{Equation 5-4}$$

Where $-\nabla^2$ represents the electron kinetic energy, V_H is the Hartree term which represents the electrostatic energy of an electron moving in a mean electrostatic field due to the presence of other electrons, V_N represents the energy due to the nuclei, and V_{XC} is the exchange-correlation energy.[84]

While the first three terms in Equation 5-4 can be found to an exact value, the exchange-correlation term cannot be computed, so a variety of reasonable approximations have been developed, each of which can be applied depending on the requirements of the system and impacts on calculation time. The Vienna *ab* initio Simulation Package (VASP) uses all plane-wave, all-electron code, that includes the projector-augmented wave (PAW) method to describe electron-core interactions.[351] The PAW approach allows for DFT calculations to be run with greater efficiency by transforming rapidly oscillating wavefunctions that consist of a very fine mesh into smoother wave functions that are less calculation intensive. The PAW approach enables all electron properties to be calculated from these wavefunctions.[352] VASP code enables obtaining total energy calculations and structure optimizations for larger systems (containing up to thousands of atoms), and ab initio molecular dynamics simulations (containing up to a few hundred atoms).

The Local Density Approximation (LDA), was one of the first approximations developed, by Kohn and Sham[353] where the exchange-correlation potential is estimated based on the treatment of the electron surrounded by a uniform electron gas of density, *n*, at each point. While this was found to be effective for pure metals, when applied to other systems, it has setbacks including overestimation of binding energies and underestimation of crystal lattice parameters.[82] A different approach, referred to as the Generalized Gradient Approach (GGA), where a density gradient is applied to the spatial variations of *n(r)*[354, 355] and has been shown to reduce the errors obtained by LDA by a factor of approximately 4.[356] In addition to expanding on the exchange correlation term, additional methods, such as DFT + U allowed for greater accuracy for other systems involving transition metals. *U* is defined as an on-site Coulomb interaction parameter, which is derived by either fitting to experimental data, or by running self consistency calculations. This parameter has been incorporated into many battery material related calculations, such as calculations addressing metal oxides.

Metal oxides with the Hollandite structure, and chemical formula of $A_xM_8O_{16}$ have been widely reported as materials of interest for energy storage applications.[281, 357-361] With the chemical formula of $A_xM_8O_{16}$, *A* refers to the tunnel cation, and *M* refers to the transition metal that forms the backbone of the tunnel structure, which can exist in a mixed valence state, such as the Mn^{4+} and Mn^{3+} mixed valence state that exists when *M*= Mn.[362] Hollandite, α-MnO_2, consists of MnO_6 octahedra, in the parent structure of α-MnO_2 structure (14/*m*), with minimal variation between the six Mn-O bond length (varying 0.02Å near a value of 1.90Å).[363] Jahn-Teller distortion can arise from the 4th electron in Mn^{3+} in the e_g level, leading to possible distortion that can lower the electronic energy. Additionally, other factors including ionic radius ratio, local Coulombic interactions, and magnetic interactions from varying the metal cation, *M*, and the tunnel cation, *A*, can influence structural distortions as well.[362] Experimentally, the effects of this strain have been observed in situ by synchrotron-based X-ray diffraction,[364] and degradation in symmetry has been observed in situ by transmission electron microscopy (TEM).[365] Additional insight into the oriented attachment has been described by in situ liquid cell TEM and first principles studies that showed that nanowire growth is driven by lower stability of the (1 1 0) surface (compared to the (1 0 0) surface), and that saturation of Mn atoms at the (1 1 0) edges that leads to generated nanowire growth.[366] On the electrode scale, the structural changes can be correlated to observed dissolution of Mn^{3+} leading to capacity fade, coupled with additional destabilization during cycling. [367, 368]

Previous bulk theoretical approaches for hollandite and cryptomelane in energy storage applications have utilized Density Functional Theory to predict and rationalize structural and electronic phenomena. For example, a previous study focused on the treatment of the physical properties that resulted from the mixed valence state of Manganese, namely between Mn^{4+} and Mn^{3+}.[362] Initially starting with the Generalized Gradient Approach by Perdew, Burke, and Ernzerhof,[369] the impact of van de Waals interactions were evaluated using the Opt-B88 functional,[370] and then a Hubbard correction (DFT+U) approach was incorporated for the Mn 3d electrons.[371, 372] In a separate study, the electrochemical properties of $\boldsymbol{\alpha}$-MnO_2 were reported using Density Functional Theory with the Hubbard U correction (DFT+U) to determine favorable insertion sites for the Li-ion and Na-ion insertion. The observed tetragonal structure was reproduced, and the calculated lithium intercalation voltage (of 3.36V vs Li/Li^+) was consistent with experimental measurements. Insertion sites for Li insertion showed that the off-

center 8h site was the preferred site by Li ion, but it was observed that there was a shift to the 8h' site **(Figure 5.1)** at the lithiation amount of $\boldsymbol{\alpha}$-$Li_{0.75}MnO_2$. In addition, there was a structural distortion with $\boldsymbol{\alpha}$-$Li_{0.75}MnO_2$ and $\boldsymbol{\alpha}$-$LiMnO_2$, which was noted as being a likely contributing factor to degradation observed with $\boldsymbol{\alpha}$-MnO_2 during cycling.[373]

The above followed previous work that considered Li-ion and lithium oxide insertion into $\boldsymbol{\alpha}$-MnO_2, where structural distortions upon lithiation and the thermodynamics of insertion were evaluated. For Li insertion, it was associated with a particular order of the reduction of Mn ions,

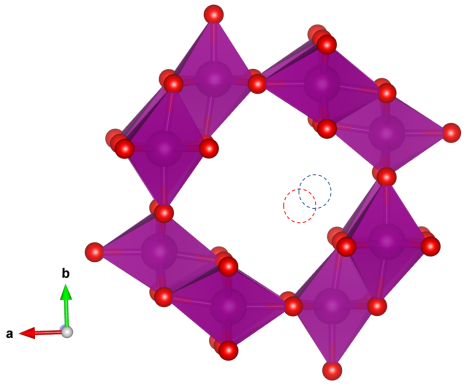

Figure 5.1. Mn_8O_{16} showing positions of 8h site (blue) and 8h' site (red).

where asymmetric changes of the lattice parameters (a and b) were observed, along with a lowering of the symmetry of the structure from tetragonal to orthorhombic. [374] Additional DFT studies have looked at magnetic and electronic structure properties[375] and Li-ion, lithium peroxide (Li_2O_2) and Lithium oxide (Li_2O) insertion in the tunnels of $\boldsymbol{\alpha}$-MnO_2.[376] More recently, a mechanistic understanding of the lithiation pathway of $\boldsymbol{\alpha}$-MnO_2 has been proposed utilizing first-principles calculations, both in $\boldsymbol{\alpha}$-MnO_2 described by a Mn_8O_{16} supercell, and by evaluating the role of a transition metal substituent for one of the eight Mn.[377] It was found that the addition of a substituent can tune multiple variables and lead to diversity in charge ordering, and structural stability, which in turn effects lithiation behavior. Results of the DFT study on Mn substitution, showed that Cr was the most effective substituent in retaining the tunnel structure up to lithiation of 0.625, compared to unsubstituted $\boldsymbol{\alpha}$-MnO_2 tunnels that had breakage at lithiation amounts of 0.5.[377]

The above work on hollandite utilized DFT models representative of the bulk material. However, moving from bulk material investigations to evaluating the surface properties of a

material requires alternate approaches and models. Previously, the lithiation mechanism of zinc ferrite had been studied by DFT, which provided insight into the lithiation of $ZnFe_2O_4$ to $Li_nZnFe_2O_4$ up to $n \leq 2$.[378] Zinc ferrite has a spinel structure with Fe^{3+} located in octahedral 16d sites, Zn^{2+} in tetrahedral 8a sites, and O^{2-} located in octahedra 32e sites. The vacancy sites, which are sites that will accommodate lithiation include the octahedral 16c position, and tetrahedral 48f and 8b sites.[379] This study proposed lithiation intermediates, and was similar to experimental observations in predictions of measured open circuit voltages above $Li_nZnFe_2O_4$ (where $n \geq 0.5$). However, with the smaller amounts of lithiation ($n < 0.5$) in the initial lithiation stage, the predicted OCVs were lower than corresponding measured values.[380, 381] This difference was subsequently addressed by evaluating the role of the surface in this initial lithiation stage. Based on initial High Resolution Transmission Electron Microscopy (HRTEM) data, the bulk material had terminations of several facets including the (2 2 0),[258, 382, 383] (1 1 1)[258, 383-386] and (3 1 1)[258, 382, 385, 387] where upon lithiation the (1 1 1) facet was found both to be the most stable and have the highest rate of Li interaction,[383] but the mechanism was still unclear. DFT calculations provided insight into the experimentally observed stability of the (1 1 1) phase by analysis of surfaces of both high index and lower index planes, whose selection was informed by XRD and TEM studies. The surface slab model utilized was constructed with symmetric terminations on both ends of the slab perpendicular to the vacuum layer, which provides a more representative approach to comparing slab energies compared to slab structures with asymmetric terminations.[378] The calculated surface energy of slabs of various terminations were defined as a function of the chemical potentials of Zn and Fe, for determination of the primary facet(s) over a range over chemical potentials. This follows previous reports using a similar method of utilizing chemical potential diagrams for a multi-component system.[388-391]

DFT studies on the surface effects of hollandite structures, α-MnO_2 have been more limited.[392, 393] For example, the surface properties of hollandite, α-MnO_2 have been studied using the *ab initio* method to identify the relative surface energies that predict the relative morphology and the tendency for the material to form in rod-like morphology along the c axis.[393] Initially, a screening method was utilized to identify low energy surfaces. Once the low energy surface candidates were identified, then Density Functional Theory was utilized to describe the electronic effects of the system. Selected candidate lower energy surfaces were treated using Density Functional Theory using VASP[394], with PAW potentials. The Generalized Gradient

Approximation (GGA) from Perdew, Burke and Erzenhof[369] was used with a Hubbard U correction (PBE + U), which has provided previous descriptions of metal oxide systems.[395] The value of the U parameter was initially determined using Wien2k[396, 397] where a parameter of U_{eff} = (U-J)= 5.2eV was used, and J = 1.0eV. Using the parameters, the calculated results of α-MnO_2 were within 2.5% of experimental lattice parameters, which was shown to be consistent with the use of PBE + U to overestimate the cell volume.[398] The surface energy was calculated by taking the difference between the energy of the constructed slab and the equivalent number of α-MnO_2 formula units in the bulk[393]:

$$\gamma = \frac{E_s - nE_b}{2S} \qquad \textit{Equation 5.5}$$

Where, E_s = Energy of the slab containing n formula units; E_b = Total energy per formula unit of bulk- α-MnO_2, $2S$= Twice the surface area of the slab (accounting for two surfaces per slab)

The predicted morphology of α-MnO_2 was visualized using a Wulff construction from the calculated surface energies. It was noted that the surfaces of the (100) and (110) planes were the most stable, having surface energies of 0.64 and 0.75 J m^{-2}, respectively, as shown in **Figure 5.2**, reproduced from Ref.[393] with permission from the Royal Society of Chemistry. All other

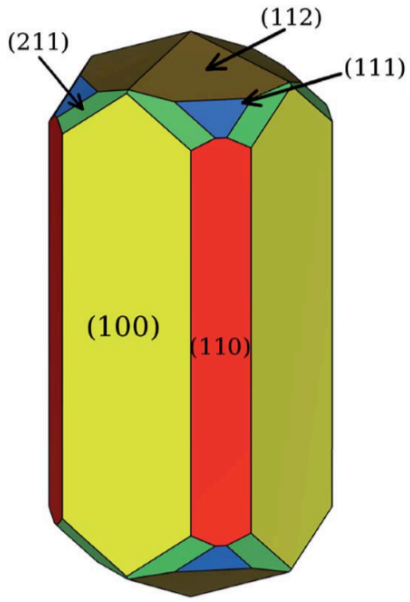

Figure 5.2. Predicted equilibrium surface energies of surface planes of α-MnO_2. Reproduced from Ref. 394 with permission from the Royal Society of Chemistry.

surfaces, had surface energies greater than 1. Following the Wulff diagram, it was proposed that the (100) surface represented 54% of the crystal surface area followed by the (110) surface that made up 20%. It was noted that the surfaces that make up the end caps of the crystal were > 45% higher in energy than the (100) and (110) planar surfaces, explaining then tendency of the crystal morphology to elongate preferentially along the c-axis.[393]

A subsequent study looked at the changes in electronic structure in bulk and nanorod MnO_2 to evaluate the surface effects of the nanomaterials. Several models were generated that considered the bulk material, crystal configurations, and the nanorod.[392] Based on the aforementioned report that evaluated α-MnO_2 surfaces,[393] only two prominent and stable Miller index planes (100) and (110) were considered in the constructions. Extending the evaluation of surfaces, nanorod models were constructed following experimental results reported by Zhang et al.[399] A microfacet structure was built that was only composed of (100) and (110) Miller indices, to link the properties of the bulk structure with the nanorod morphology. This was generated to act as a structure that would link the bulk surface and the nanorod morphologies. It was shown by partial density of states (PDOS) that the stability of the bulk surface was different from the electronic structure of nanorod models generated with only the (1 0 0) and (1 1 0) surfaces, where the (1 1 0) surface facet acted as an electron donor, and the (1 0 0) surface acted as an electron acceptor. The above reports evaluated relative surfaces of α-MnO_2, without a central cation, or substitution of a transition metal for one of the Manganese atoms. In specifically addressing surface stability, DFT calculations employ the slab method, where planes are cleaved from a bulk calculation of the material at a specified facet.

Herein, this study evaluates the surfaces of potassium hollandite, KMn_8O_{16}. Following the reported literature on α-MnO_2, surfaces of the (0 0 1), (1 0 0), and (1 1 0) facets were initially investigated corresponding to the unstable end plane (0 0 1), and majority facets (1 0 0), (1 1 0).

To investigate and compare the relative surface stabilities, two methods are utilized here to evaluate the converged surfaces. This includes a comparison of the cleavage energies and evaluating the surface energies over a range of chemical potentials of Manganese and Oxygen following an approach outlined in previous reports.[379, 400] Cleavage energy determinations will provide the relative stability of the surface slab with respect to the KMn_8O_{16}, where the more negative the cleavage energy, the more stable the surface. The phase diagrams will provide

insight into the predominate facet(s) over a range of chemical potentials (for Manganese and Oxygen). Utilizing a range of chemical potentials to generate phase diagrams enables the comparison of different surfaces that are not specifically repeat units of the bulk, and allows for a variety of surface constructions to be compared.

5.1 Experimental

DFT Calculations. DFT calculations were performed using the Vienna ab initio Simulation Package[394, 401] using spin-polarized DFT +U calculations employing the projector augmented wave potential (PAW)[352] using the Perdew-Burke-Ernzenhof exchange-correlation functional.[369] A kinetic energy cutoff of 415 eV was used, along with a Hubbard U-J correction, U_{eff} = 5.1 – 1.2 eV applied to Mn d orbitals following previous studies.[362, 377] The Gaussian smearing method was used with the total energies converged better than 10^{-5} eV, and the final force on each atom was less than 0.01 eV $Å^{-1}$. The first Brillouin zone was sampled on a 2 x 7 x 1 or 2 x 2 x 2 k-mesh (depending on the supercell lattice parameters).

Surface Stability Calculations. The slab model was generated from converged bulk structures of KMn_8O_{16}. The number of layers varied depending on the termination, and tunnel type (partial tunnel or full tunnel on the surface). A 15 Å thick vacuum layer was included along the axis perpendicular to the surface to prevent interactions between the slab surfaces. For optimization studies, the first three layers (both on the top and bottom of the surface construct) were allowed to relax (denoted as free atoms), and the remaining atoms were fixed in their atomic positions.

Following previous reports on determining the relative surfaces energy of ferrites for Li ion battery studies[379, 400], the stability of the hollandite surface energies can be defined as the following:

Surface energy, ζ, for unsubstituted KMn_8O_{16} surfaces :

$$\zeta = \frac{E_{slab} - x\mu_K - y\mu_{Mn} - z\mu_O}{2S}$$

Where:

E_{slab} = total energy of the hollandite surface, and $\mu_K,\ \mu_{Mn},\ \mu_O$ are the chemical potentials of Potassium (μ_K), Manganese (μ_{Mn}), and Oxygen (μ_O).

$2S$ = 2 times the surface area of the slab, accounting for both the upper and lower surfaces

The chemical potentials can exist in a range where the sum of the chemical potentials of the constituent elements (accounting for stoichiometry) is equivalent to the energy of the surface slab, where, for the undoped structure:

$$\mu_{KMn_8O_{16}} = \mu_K + 8\mu_{Mn} + 16\mu_O = E_{KMn_8O_{16}}$$

The range of $\mu_K,\ \mu_{Mn},\ \mu_O$ where hollandite (KMn_8O_{16}) is stable:

$$\Delta\mu_K = \mu_K - E_K < 0$$

$$\Delta\mu_{Mn} = \mu_{Mn} - E_{Mn} < 0$$

$$\Delta\mu_O = \mu_O - E_O < 0$$

Since Mn and O are dominant by stoichiometry, the surface energy can be expressed in terms of Mn and O.

The surface energy is expressed as a function of $\Delta\mu_{Mn}$ and $\Delta\mu_O$, where potassium (K) is held constant:

For KMn_8O_{16}:

$$\zeta = \vartheta - \frac{(y-8x)\Delta\mu_{Mn} + (z-16x)\Delta\mu_O}{2S}$$

Where, ϑ is a constant for cleavage energy, and is utilized to determine the relative surface stability with respect to the KMn_8O_{16} bulk :

$$\vartheta = \frac{E_{K_xMn_yO_z} - xE_{KMn_8O_{16}} - (y-8x)E_{Mn} - (z-16x)E_O}{2S}$$

Based on the above equations, phase diagrams of various surfaces with different configurations were generated. Additionally, calculated cleavage energies, ϑ, were compared to compare the relative stability of surfaces, including all surfaces tested.

5.2 Results and Discussion

5.2.1 *Comparison of Cleavage Energies of KMn_8O_{16} Surfaces*

Initially, the unsubstituted surfaces were evaluated and cleavage energy, ϑ, was determined by comparing termination, and/or full or partial tunnel constructs on the surface. The cleavage energy is a measure of surface stability with respect to the KMn_8O_{16} bulk and metallic K, Mn and O_2 gas. For the (0 0 1) surface, termination of the surface was varied, since the tunnel structure for (0 0 1) was not visible from the side view of the surface slab. The Mn-O_2-K termination had Mn atoms located on the plane corresponding to the surface layer that were in a lower coordination environment compared to full MnO_6 octahedra, where each of the four surface Manganese atoms were coordinated to four oxygen atoms, as shown in **Figure 5.3A, B.** Alternatively, a separate surface representing the (0 0 1) facet was tested with full MnO_6 octahedra representing the surface termination, and potassium atoms located in what would be representative of the bulk layers of the structure, **Figure 5.3C, D.** In comparing the cleavage energies of the two surface structures, the (0 0 1) surface with Mn-O_2-K termination had a slightly higher cleavage energy (0.28 J/m^2) compared to the cleavage energy of the (0 0 1) surface with Oxygen termination (0.26 J/m^2). The cleavage energy reported was reported for the whole surface slab, where the surface areas of the two slabs were both 98 $Å^2$.

The lower cleavage energy of the O-terminated (0 0 1) surface could potentially be contributed to the increased coordination of the surface manganese.

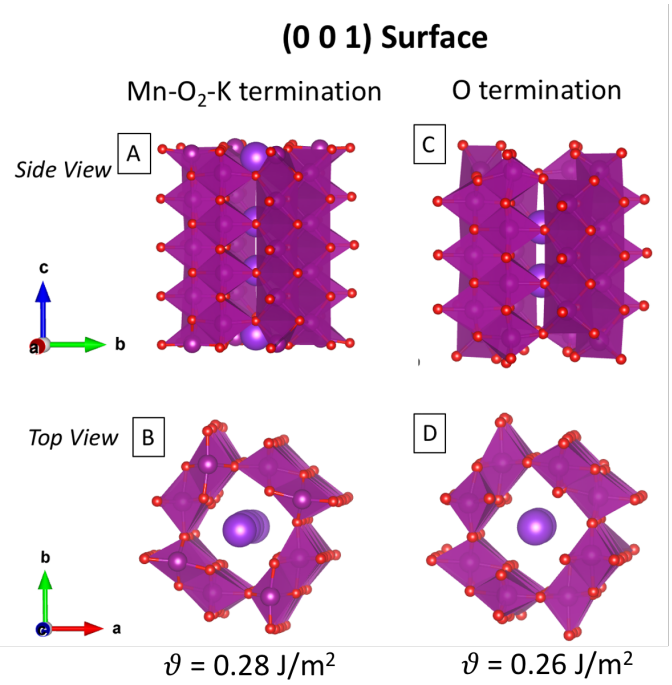

Figure 5.3. Comparison of the (0 0 1) surface constructions, with: (A,B) Mn-O_2-K termination, and (C, D) O- termination.

Next a comparison of the (1 0 0) and (1 1 0) surfaces utilized models that varied the arrangement of the surface octahedra along the area that was surface adjacent. Initially, two constructs of the (1 0 0) surface were evaluated comparing termination of a full tunnel and partial tunnel making up the surface **(Figure 5.4, A, B).** Comparing the two configurations of the (1 0 0) surface, the full tunnel construction **(Figure 5.4A)** had a lower cleavage energy (-1.01 J/m^2) compared to the partial tunnel on the surface (-0.49 J/m^2), which would be consistent with expectations of an extra dimer configuration on the surface, compared to a fully coordinated intact tunnel. However, despite the lower cleavage energy of the full tunnel compared to the partial tunnel, the partial tunnel cleavage energy was still low compared to the other (0 0 1) surfaces. To compare the relative stability of the surface Mn on the full tunnel and partial tunnel constructs, projected density of states (PDOS) was obtained for the 3d orbitals of two Mn atoms either on the surface **(Figure 5.4,A, B**, or sublayer (B) of full and partial KMn_8O_{16} tunnels. Initially comparing the surface Mn of the full tunnel structure **(5.4A- green**), to the surface dimer

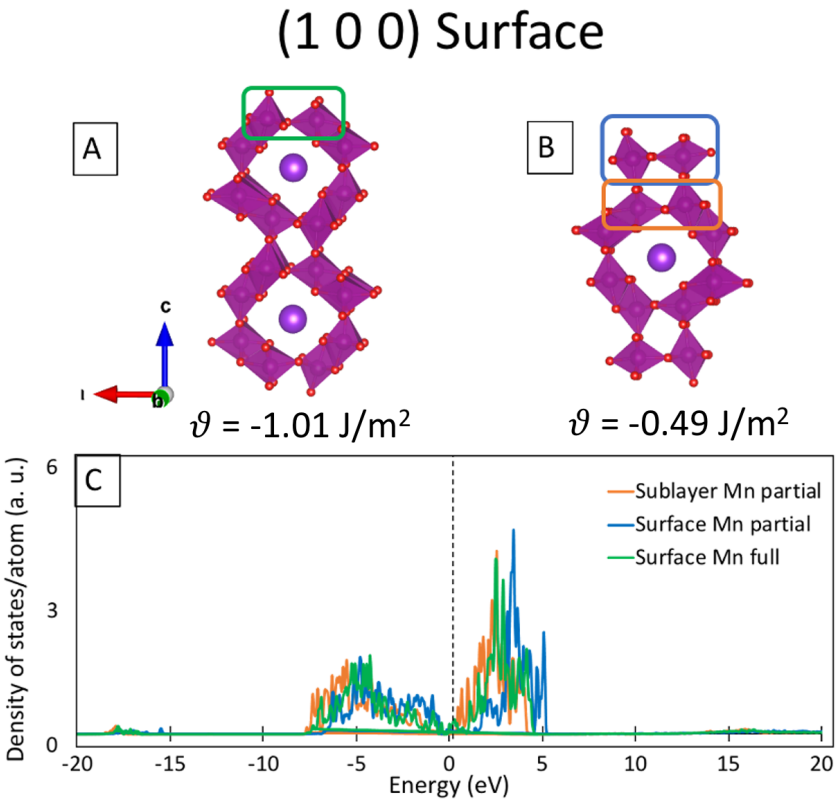

Figure 5.4. Comparison of cleavage energies of (1 0 0) surfaces with (A) full tunnel structure, (B) partial tunnel structure, and (C) comparison of electronic structure of surface and sublayer Mn 3d partial density of states.

MnO_6 octahedra on the partial tunnel structure (**B-blue**), there was a downshift in the energy of the surface Mn on the full tunnel compared to the dimer surface Mn on the partial tunnel, noting increased stability in the full tunnel construct. Additionally, when comparing the sublayer the structure in **Figure 5.4B,** there was an additional downshift observed, noting that the relative stability would be: Mn partial tunnel sublayer > Mn full tunnel surface > Mn partial tunnel dimer surface.

Following observations of the surface configuration of the MnO_6 octahedra, two constructs of the (1 1 0) surface were generated that varied the architecture of the partial tunnel surface (**Figure 5.5, A, B)** in addition to the full tunnel structure (**Figure 5.5C**). When comparing the cleavage energies, the structure with a partial tunnel on the surface consisting of two layers of MnO_6 octahedra (**Figure 5.5A**) had the lowest cleavage energy within the series, followed by the partial tunnel structure with a single MnO_6 octahedra on the surface (**Figure 5.5B**). In contrast to the (1 0 0) surface, for the (1 1 0) surface, partial tunnels were shown to have lower cleavage energy compared to the full tunnel surfaces. To compare the effects of the MnO_6 varied surface architecture, projected density of states (PDOS) for Mn 3d was compared for the full tunnel (**Figure 5.5C**), and two partial tunnel structures (**Figure 5.5A,B**). As shown in **Figure 5.5D,** there was a notable downshift in energy and increase of intensity (of the states per surface atom for Mn 3d) with the addition of levels of MnO_6 octahedra on the surface.

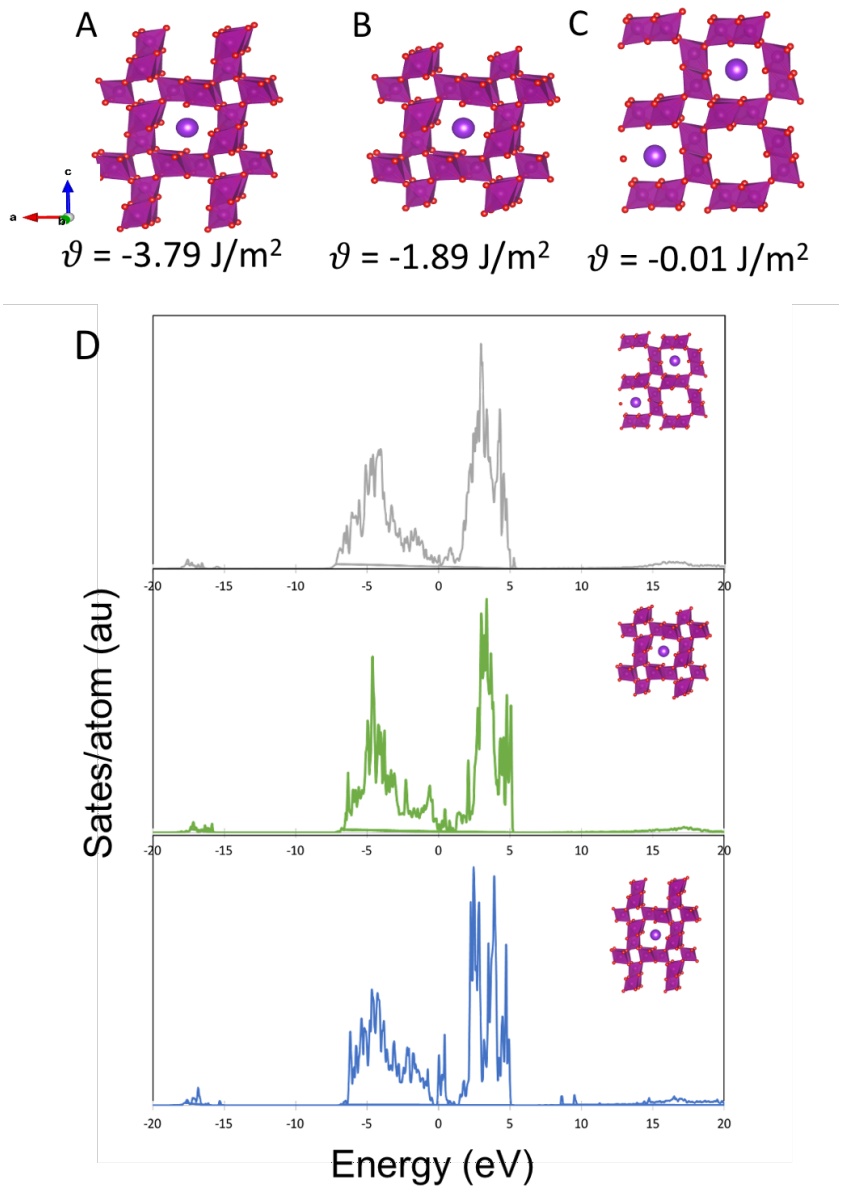

Figure 5.5. Comparison of terminations and cleavage energies of KMn_8O_{16} (1 1 0) with (A) 2 layers of MnO_6 surface octahedra,(B) single layer of MnO_6 surface octahedra, (C) full tunnel structure; (D) Projected density of states for Mn 3d or surface Mn atoms comparing all three surface types.

An additional set of structures evaluated the location of the surface K^+ in location in either a hollow site or bridging site. To eliminate discrepancy between the number of and placement of K atoms, the binding energy (E_b) was calculated comparing the location of the K ion as either "hollow" (**Figure 5.6A)** or "bridging" (**Figure 5.6B**) sites, following notation used in a previous report on lithium ion placement on a cleaved surface, where the hollow site has an environment with additional oxygen atoms compared to the bridging site.[378] Binding energy for the bridging and hollow sites were quantified and compared as shown in **Figure 5.6C.** The hollow site, which correlated to the natural position of the K ion after convergence of the bulk KMn_8O_{16} material, had a reduced binding energy (-8.82 eV), compared to the bridging site, which had a binding energies of -7.68eV, respectively.

In the bridging site, the K ion was situation between two O-O atoms, acting as a bridge, whereas in the hollow site, the K ion was positioned to be in an O-O-O environment.

Binding energy was determined from the following equation:

$$E_b = E_{nK/Surface} - E_{Surface} - nE_{K\text{-}bulk}$$

Where $E_{nK/Surface}$, $E_{Surface}$ and nE_{K^+} correspond to the total energy of K-adsorbed surface, bare surface and K_{bulk}, respectively.

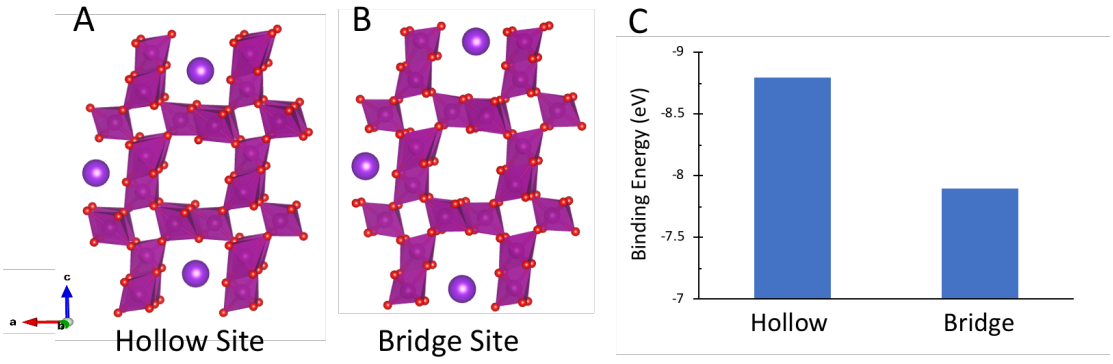

Figure 5.6. Comparison of position of K^+ in A) Hollow site, B) Bridge site and C) Comparison of binding energy of each (compared to K_{bulk}).

The cleavage energies of all unsubstituted surfaces previously discussed are shown in **Table 1.** In comparing only the full tunnel structures, (1 0 0) had the lowest cleavage energy, whereas when both full and partial tunnel structures were compared, (1 1 0) partial tunnel structure had the lowest cleavage energy.

Table 5.1. Comparison of cleavage energies of KMn_8O_{16} surfaces

Crystal	Surface slab	Termination	Cleavage Energy to Mn-O (J/m^2)	Tunnel
KMn_8O_{16}	(0 0 1)	-O	0.26	Full
		-Mn-O_2-K	0.28	Full
	(1 0 0)	-O	-0.49	Partial
		-O	-1.01	Full
	(1 1 0)	-O	0.01	Full
		-O	3.37	Partial
		-O	-3.79	Partial
		-O	-1.89	Partial

5.2.2 *Phase Diagrams of Unsubstituted KMn_8O_{16} Surfaces*

After determination of cleavage energy to compare the relative stability of a variety of surfaces (0 0 1), (1 0 0), (1 1 0) of the KMn_8O_{16} crystal, phase diagrams were generated showing the dominant facet over a range of chemical potential based on Manganese and Oxygen. The range of chemical potential notes which phase would exist in Mn rich, Mn poor, or Oxygen rich and Oxygen poor structures, as shown in **Figure 5.7A** Two comparisons were conducted, first, all of the structures containing full tunnel structures were compared, and there was one single primary facet obtained over the range of chemical potentials, the full tunnel structure of the (1 0 0) surface. This corresponds to previous literature reports on α-MnO_2 surface studies, that reported the (1 0 0) surface to have the lowest surface energy, and therefore be the most stable facet.[393] Following comparison of the full tunnel unsubstituted surfaces, all of the unsubstituted surfaces reported in **Table 1** were compared to determine the primary facet to generate phase diagrams. When the partial tunnel structures were included, the partial tunnel structure of the (1 1 0) surface with two MnO_6 octahedra layers became a primary facet over a small range of

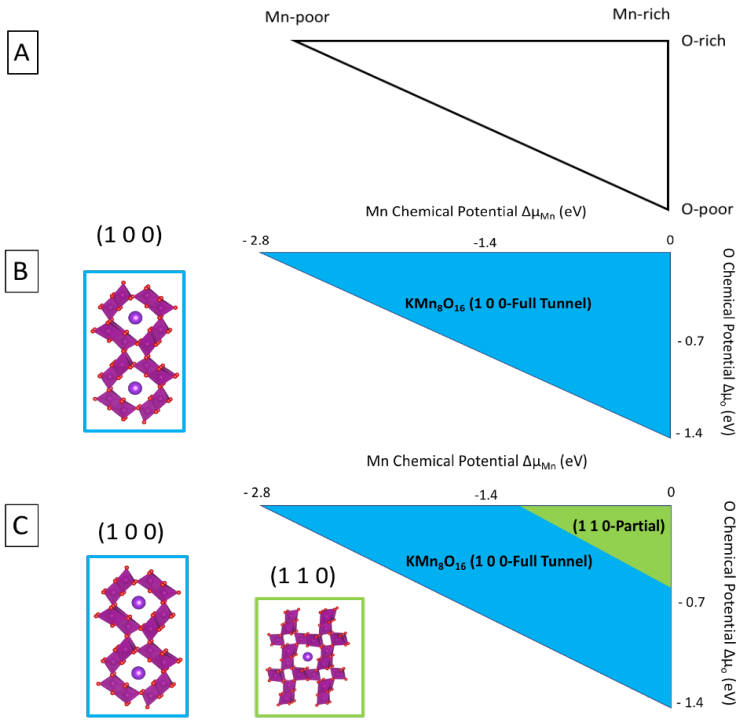

Figure 5.7. Phase diagrams showing (A) Mn- and O- rich and poor regions in schematic, (B) Comparison of only full tunnel structures, (C) comparison of both full and partial surfaces.

chemical potentials corresponding to the area of Mn-rich and O-rich. Calculated results and subsequent cleavage energies and phase diagrams agreed with prior literature reports that showed the (1 0 0) surface to be more stable compared to the (1 1 0) or the (0 0 1) surfaces.[392, 393] The difference in methods by calculating cleavage energy and utilizing a phase diagram approach to compare tested facets, allows for the expansion of structures to be tested outside of stoichiometric equivalents of the bulk (i.e. KMn_8O_{16}). An interesting benefit to expanding the type of supercell to outside of a stoichiometric repeat is to incorporate the termination of the surface in terms of partial or full tunnel structure, where the (1 1 0) surface was shown to be the primary facet over chemical potentials ranges rich in Mn and O.

Summary

A comparison of unsubstituted KMn_8O_{16} surfaces showed that chosen termination (partial or full tunnel) of the selected surfaces can affect the observed facets observed in a phase diagram across the chemical potential range for Mn and O. Additionally, the addition of MnO_6 octahedra layers on the surface plane either generated a higher cleavage energy (1 0 0) or a lower cleavage energy (1 1 0) depending on the surface plane. The addition of utilizing cleavage energy and chemical potential provides opportunities to alter the supercell outside of stoichiometric repeats of a unit.

5.3 Outlook and Future Directions

Previously, a series of structures containing substituent atoms, M= Ti, V, Cr, Nb, Ru, were examined using DFT to substitute one of the Mn atoms in the tunnel wall, yielding $Mn_{0.875}M_{0.125}O_2$. Substitution was conducted in an effort to improve the structural stability of the tunnel, which is prone to Jahn-Teller distortion leading to expansion of the unit cell in the reduction of Mn^{4+} (d^3) → Mn^{3+} (d^4) upon lithiation.[377] Results of the DFT study on Mn substitution, showed that Cr was the most effective substituent in retaining the tunnel structure up to lithiation of 0.625, compared to unsubstituted $\boldsymbol{\alpha}$-MnO_2 tunnels that had breakage at lithiation amounts of 0.5.[377]

More recently, reported experimental studies examined Vanadium substitution in a series of Vanadium-substituted silver hollandite samples, ($Ag_{1.2}V_yMn_{8-y}O_{16}$, y = 0 – 0.8) which showed that upon Vanadium substitution, there was a decrease in the length of the nanowires with an accompanying reduction in the diffusion path length along the c-axis.[402] The above examples highlight the potential impact of metal substitution into α-MnO_2, and highlight the need to continue to link experimental observations to theoretical predictions to be able to understand observed trends, such as developing explanations for the change in nanowire length upon Vanadium substitution of silver hollandite surfaces. Various locations for vanadium substituents will be considered. Based upon the initial results with unsubstituted KMn_8O_{16} surfaces, it is anticipated that upon introduction of a Vanadium substituent for Mn, the location of the substituted Vanadium (on surface versus within the bulk) may impact the cleavage energy.

Acknowledgements

I would like to acknowledge Dr. Ping Liu for advisement on this project, as part of collaborative work in the Center for Mesoscale Transport Properties (m2m/t) Energy Frontier Research Center (EFRC) funded by the U. S. Department of Energy, and Dr. Haoyue Guo for the methodology, surface development and calculations for evaluating the surfaces. The calculations were conducted using Stony Brook Research Computing and Cyberinfrastructure, and the Institute for Advanced Computational Science at Stony Brook University through the high-performance SeaWulf computing system, funded through the National Science Foundation. I would also like to acknowledge Killian Tallman for instruction on VASP, and Dr. Alexander Brady for developing methodology utilized for hollandite DFT calculations.

VI. Summary

The above work describes a multi-pronged approach, both in correlating structure to function relationships in energy storage systems by characterizing the material and subsequent electrochemistry, and by addressing a variety of systems that are ultimately linked to requirements of a particular application. For example, work on the solid state, self-forming rechargeable battery eliminates the use of flammable organic electrolytes, and begins with a single composite that has the potential for a longer shelf life due to the nature of the development of anode, cathode, and separator components upon charge. Work on the lithium sulfur system, has demonstrated two distinct approaches for improving capacity retention after sustained cycling either by tuning synthetic methods to develop additives that can directly be incorporated into a composite cathode, or by demonstrating a single facile approach for larger scale electrodeposition. Future studies can build on the above work, by incorporating theoretical models, and implementing a multitude of characterization techniques that can evaluate the electrode scale, including the inclusion of scanning probe techniques to provide insight into the conductive or insulating behavior of electrodes. This approach will facilitate the future of research into expanding into beyond Li systems for the future of energy storage.

References

1. Kim, T.; Song, W.; Son, D.-Y.; Ono, L. K.; Qi, Y., Lithium-ion batteries: outlook on present, future, and hybridized technologies. *Journal of Materials Chemistry A* **2019,** *7* (7), 2942-2964.

2. Bock, D. C.; Marschilok, A. C.; Takeuchi, K. J.; Takeuchi, E. S., Batteries used to power implantable biomedical devices. *Electrochimica Acta* **2012,** *84*, 155-164.

3. Takeuchi, E. S.; Leising, R. A.; Spillman, D. M.; Rubino, R.; Gan, H.; Takeuchi, K. J.; Marschilok, A. C., Lithium Batteries for Medical Applications. In *Lithium Batteries*, Nazri, G. A.; Pistoia, G., Eds. Springer: Boston, M.A., 2009; pp 686-700.

4. Baumann, M.; Weil, M.; Peters, J. F.; Chibeles-Martins, N.; Moniz, A. B., A review of multi-criteria decision making approaches for evaluating energy storage systems for grid applications. *Renewable and Sustainable Energy Reviews* **2019,** *107*, 516-534.

5. Hao, X.; Zhou, Y.; Wang, H. W.; Ouyang, M. G., Plug-in electric vehicles in China and the USA: a technology and market comparison. *Mitig. Adapt. Strateg. Glob. Chang.* **2020**, 25.

6. *Global EV Outlook 2018*. International Energy Agency: 2018.

7. Zhou, Y., Wang, M., Hao, H., Johnson, L., Wang, H., Hao, H., Plug-in electric vehicle market penetration and incentives: a global review. . *Mitig Adapt Strateg Glob Chang* **2015,** *20*, 777–795.

8. Tullo, A., Samsung reports on Galaxy Note 7 fires. *Chem. Eng. News* **2017,** *95* (5), 11-11.

9. Fact Sheet- Lithium Batteries in Baggage. https://www.faa.gov/news/fact_sheets/news_story.cfm?newsId=23054 (accessed Feb. 4th).

10. *Energy Frontier Research Centers: Science for Our Nation's Energy Future*; U. S. Department of Energy: Basic Energy Sciences: Washington, D. C., 2019.

11. 2016-2020 Strategic Plan and Implementing Framework. U. S. Department of Energy: Office of Energy Efficiency and Renewable Energy: 2015.

12. Batteries: 2018 Annual Progress Report. U. S. Department of Energy:Office of Energy Efficiency and Renewable Energy: Vehicle Technology Office: 2019.

13. DOE OE Global Energy Storage Database.

14. Cannarella, J., Arnold, C. B., Stress evolution and capacity fade in constrained lithium-ion pouch cells. *J. Power Sources* **2014,** *245*, 745-751.

15. Zhang, Z.; Shao, Y.; Lotsch, B.; Hu, Y.-S.; Li, H.; Janek, J.; Nazar, L. F.; Nan, C.-W.; Maier, J.; Armand, M.; Chen, L., New horizons for inorganic solid state ion conductors. *Energy & Environmental Science* **2018,** *11* (8), 1945-1976.

16. Teng, S., Tan, J., Tiwari, A., Recent developments in garnet based solid state electrolytes for thin film batteries. *Curr. Opin. Solid State Mater Sci.* **2014,** *18* (1), 29-38.

17. Dudney, N. J., West, W. C., Nanda, J., *Handbook of Solid State Batteries. 2nd edition*. World Scientific Publishing Co.: Singapore, 2015.

18. Duan, H.; Fan, M.; Chen, W. P.; Li, J. Y.; Wang, P. F.; Wang, W. P.; Shi, J. L.; Yin, Y. X.; Wan, L. J.; Guo, Y. G., Extended Electrochemical Window of Solid Electrolytes via Heterogeneous Multilayered Structure for High-Voltage Lithium Metal Batteries. *Adv. Mater.* **2019,** *31* (12), 7.

19. Zhao, Q.; Liu, X. T.; Stalin, S.; Khan, K.; Archer, L. A., Solid-state polymer electrolytes with in-built fast interfacial transport for secondary lithium batteries. *Nat. Energy* **2019,** *4* (5), 365-373.

20. Zhu, Y. S.; Connell, J. G.; Tepavcevic, S.; Zapol, P.; Garcia-Mendez, R.; Taylor, N. J.; Sakamoto, J.; Ingram, B. J.; Curtiss, L. A.; Freeland, J. W.; Fong, D. D.; Markovic, N. M., Dopant-Dependent Stability of Garnet Solid Electrolyte Interfaces with Lithium Metal. *Adv. Energy Mater.* **2019,** *9* (12), 11.

21. Zhang, X.; Wang, S.; Xue, C. J.; Xin, C. Z.; Lin, Y. H.; Shen, Y.; Li, L. L.; Nan, C. W., Self-Suppression of Lithium Dendrite in All-Solid-State Lithium Metal Batteries with Poly(vinylidene difluoride)-Based Solid Electrolytes. *Adv. Mater.* **2019,** *31* (11).

22. Xu, L. Q., Li, J.Y., Cheng, L., Zou, G.Q., Hou, H.S., Ji, X.B., Research Progress in Inorganic Solid-State Electrolytes for Sodium-Ion Batteries. *Acta Phys-Chim Sin.* **2020,** *36* (5), DOI: 10.3866/PKU.WHXB201905013.

23. Zhao, C. L., Liu, L.L., Qi, X.G., Lu, Y. X., Wu, F. X., Zhao, J. M., Yu, Y., Hu, Y. S., Chen, Y. Q., Solid-State Sodium Batteries *Adv. Energy Mater.* **2018,** *8* (17), 1703012.

24. Deivanayagam, R.; Cheng, M.; Wang, M. C.; Vasudevan, V.; Foroozan, T.; Medhekar, N. V.; Shahbazian-Yassar, R., Composite Polymer Electrolyte for Highly Cyclable Room-Temperature Solid-State Magnesium Batteries. *Acs Applied Energy Materials* **2019,** *2* (11), 7980-7990.

25. Wang, L. P.; Zhao-Karger, Z.; Klein, F.; Chable, J.; Braun, T.; Schur, A. R.; Wang, C. R.; Guo, Y. G.; Fichtner, M., MgSc(2)Se(4)A Magnesium Solid Ionic Conductor for All-Solid-State Mg Batteries? *Chemsuschem* **2019,** *12* (10), 2286-2293.

26. Zhang, Q.; Ding, Z. G.; Liu, G. Z.; Wan, H. L.; Mwizerwa, J. P.; Wu, J. H.; Yao, X. Y., Molybdenum trisulfide based anionic redox driven chemistry enabling high-performance all-solid-state lithium metal batteries. *Energy Storage Materials* **2019,** *23*, 168-180.

27. Sakuda, A.; Sato, Y.; Hayashi, A.; Tatsumisago, M., Sulfur-Based Composite Electrode with Interconnected Mesoporous Carbon for All-Solid-State Lithium-Sulfur Batteries. *Energy Technology* **2019,** *7* (12).

28. Zhang, Q.; Huang, N.; Huang, Z.; Cai, L. T.; Wu, J. H.; Yao, X. Y., CNTs@S composite as cathode for all-solid-state lithium-sulfur batteries with ultralong cycle life. *Journal of Energy Chemistry* **2020,** *40*, 151-155.

29. Han, Q.; Chi, X. W.; Liu, Y. Z.; Wang, L.; Du, Y. X.; Ren, Y.; Liu, Y., An inorganic salt reinforced Zn2+-conducting solid-state electrolyte for ultra-stable Zn metal batteries. *Journal of Materials Chemistry A* **2019,** *7* (39), 22287-22295.

30. Takeuchi, E. S., Leising, R. A., Lithium batteries for biomedical applications. *MRS Bull.* **2002,** *27* (8), 624.

31. Bock, D. C., Marschilok, A. C., Takeuchi, K. J., Takeuchi, E. S., Batteries used to power implantable biomedical devices. *Electrochim. Acta* **2012,** *84*, 155-164.

32. Schlaikjer, C. R., Liang, C. C., Ionic Conduction in Calcium Doped Polycrystalline Lithium Iodide. *J. Electrochem. Soc.* **1971,** *118* (9), 1447.

33. Li, D., Qin, D., Deng, M., Luo, Y., Meng, Q., Optimization the solid-state electrolytes for dye-sensitized solar cells. *Energy Environ. Sci.* **2009,** *2* (3), 283-291.

34. Weppner, W., Welzel, W., Kniep, R., and Rabenau, A., Fast Ionic Conduction in LiI·4 Methanol: [Li(CH3OH)4]+I−. *Angew. Chem. Int. Ed.* **1986,** *25* (12), 1087-1089.

35. Weppner, W., Welzel, W., Kniep, R., and Rabenau, A., *Angew. Chem. Int. Ed.* **1986,** *25* (12), 1087.

36. Wang, H., Wang, Z., Xue, B,. Meng, Q., Huang, X. Chen, L., Polymer-in-salt like conduction behavior of small-molecule electrolytes. *Chem. Commun.* **2004,** *19*, 2186-2187.

37. Wang, H.; Wang, Z.; Li, H.; Meng, Q.; Chen, L., Ion transport in small-molecule electrolytes based on LiI/3-hydroxypropionitrile with high salt contents. *Electrochimica acta* **2007,** *52* (5), 2039-2044.

38. Wang, H., Wang, Z., Xue, B,. Meng, Q., Huang, X. Chen, L., *Chem. Commun.* **2004,** *19*, 2186.

39. Yourey, W.; Weinstein, L.; Halajko, A.; Amatucci, G. G., Pathways to enabling solid state electrolytically formed batteries: The solid electrolyte interphase. *Electrochimica Acta* **2012,** *66*, 193-203.

40. Weinstein, L.; Yourey, W.; Gural, J.; Amatucci, G., Electrochemical Impedance Spectroscopy of Electrochemically Self-Assembled Lithium–Iodine Batteries. *Journal of the Electrochemical Society* **2008,** *155* (8), A590-A598.

41. Yourey, W., Weinstein, L., Halajko, A., Amatucci, G. G., Electrode Development in a Novel Self-Assembled Lithium Iodide Battery. *ECS Trans.* **2010,** *28* (30), 159-165.

42. Abraham, A.; Huang, J.; Smith, P. F.; Marschilok, A. C.; Takeuchi, K. J.; Takeuchi, E. S., Demonstration and Electrochemistry of a Self-Forming Solid State Rechargeable $LiI(HPN)_2$ based Li/I_2 Battery. *J. Electrochem. Soc.* **2018,** *165* (10), A2115-A2118.

43. Yourey, W., Weinstein, L. and Amatucci, G. G., Structure and charge transport of polyiodide networks for electrolytically in-situ formed batteries. *Solid State Ionics* **2011,** *204*, 80-86.

44. Ji, X., Nazar, L. F. , Advances in Li-S Batteries. *J. Mater. Chem.* **2010,** *20*, 9821-9826.

45. Yu, S.-H. F., X.; Zhang, N.; Seok, J.; Abruña, H. D., Understanding Conversion-Type Electrodes for Lithium Recharge- able Batteries. *Acc. Chem. Res.* **2018,** *51*, 273-281.

46. Gu, X. L., C. , Recent Development of Metal Compound Applications in Lithium−Sulphur Batteries. *J. Mater. Res.* **2018,** *33*, 16-31.

47. Mikhaylik, Y. V. A., J. R., Polysulfide Shuttle Study in the Li/S Battery System. *J. Electrochem. Soc.* **2004,** *151*, A1969-A1976.

48. Evers, S. N., L. F., New Approaches for High Energy Density Lithium−Sulfur Battery Cathodes. *Acc. Chem. Res.* **2013,** *46*, 1135-1143.

49. Safari, M. K., C. Y.; Nazar, L. F. , Transport Properties of Polysulfide Species in Lithium−Sulfur Battery Electrolytes: Coupling of Experiment and Theory. *ACS Cent. Sci.* **2016,** *2*, 560-568.

50. Mistry, A. N., Mukherjee, P. P, "Shuttle" in Polysulfide Shuttle: Friend or Foe? *J. Phys. Chem. C* **2018,** *122* (42), 23845-23851.

51. Gu, X. L., C.; Liu, F.; Yang, W.; Hou, Y.; Zhang, S. , A Conductive Interwoven Bamboo Carbon Fiber Membrane for Li−S Batteries. *J. Mater. Chem. A* **2015,** *3*, 9502-9509.

52. Carbone, L. C., T.; Gobet, M.; Munoz, S.; Devany, M.; Greenbaum, S.; Hassoun, J., A Simple Approach for Making a Viable, Safe, and High-Performances Lithium-Sulfur Battery. *J. Power Sources* **2018,** *377*, 26-35.

53. Zhang, X. W., Z.; Yao, L.; Mai, Y.; Liu, J.; Hua, X.; Wei, H., Synthesis of Core-Shell Covalent Organic Frameworks/Multi-Walled Carbon Nanotubes Nanocomposite and Application in Lithium-Sulfur Batteries. *Mater. Lett.* **2018,** *213*, 143-147.

54. Kim, M. S. M., L.; Choudhury, S.; Moganty, S. S.; Wei, S.; Archer, L. A., Fabricating Multifunctional Nanoparticle Membranes by a Fast Layer-by-Layer Langmuir−Blodgett Process: Application in Lithium−Sulfur Batteries. *J. Mater. Chem. A* **2016,** *4*, 14709-14719.

55. Ai, G. D., Y.; Mao, W.; Zhao, H.; Fu, Y.; Song, X.; En, Y.; Battaglia, V. S.; Srinivasan, V.; Liu, G. , Biomimetic Ant-Nest Electrode Structures for High Sulfur Ratio Lithium−Sulfur Batteries. *Nano Lett.* **2016,** *16*, 5365-5372.

56. Zhang, J. H., H.; Bae, J.; Chung, S.-H.; Zhang, W.; Manthiram, A.; Yu, G., anostructured Host Materials for Trapping Sulfur in Rechargeable Li−S Batteries: Structure Design and Interfacial Chemistry. **2018,** (2), 1700279.

57. Peng, L. Z., Y.; Chen, D.; Ruoff, R. S.; Yu, G., Two- Dimensional Materials for Beyond-Lithium-Ion Batteries. *Adv. Energy Mater.* **2016,** *6*, 1600025.

58. Lv, D., Zheng, J., Li, Q., Xie, X., Ferrara, S., Nie, Z., Mehdi, L. B., Browning, N. D., Zhang, J.-G., Graff, G. L., Liu, J.; Xiao, J., High Energy Density Lithium−Sulfur Batteries: Challenges of Thick Sulfur Cathodes. *Adv. Energy Mater.* **2015,** *5*, 1402290.

59. He, G. E., S.; Liang, X.; Cuisinier, M.; Garsuch, A.; Nazar, L. F., Tailoring Porosity in Carbon Nanospheres for Lithium-Sulfur Battery Cathodes. *ACS Nano* **2013,** *7*, 10920-10930.

60. Lu, D. L., Q.; Liu, J.; Zheng, J.; Wang, Y.; Ferrara, S.; Xiao, J.; Zhang, J.-G.; Liu, J., Enabling High-Energy-Density Cathode for Lithium−Sulfur Batteries. *ACS Appl. Mater. Interfaces* **2018,** *10*, 23094-23102.

61. Chung, S.-H. M., A., Eggshell Membrane-Derived Polysulfide Absorbents for Highly Stable and Reversible Lithium− Sulfur Cells. *ACS Sustainable Chem. Eng.* **2014,** *2*, 2248-2252.

62. Yu, S. H. L., B.; Choi, S.; Park, S.; Hong, B. H.; Sung, Y. E., Enhancement of electrochemical properties by polysulfide trapping in a graphene-coated sulfur cathode on patterned current collector. *Chem. Commun.* **2016,** *52*, 3203-3206.

63. Chang, C.-H. C., S.-H.; Manthiram, A., Highly Flexible, Freestanding Tandem Sulfur Cathodes for Foldable Li−S Batteries with a High Areal Capacity. *Mater. Horiz.* **2017,** *4*, 249-258.

64. Chung, S.-H., Manthiram, A., Designing Lithium-Sulfur Cells with Practically Necessary Parameters. *Joule* **2018,** *2* (4), 710-724.

65. Qin, F. Z., K.; Fang, J.; Lai, Y.; Li, Q.; Zhang, Z.; Li, J., High Performance Lithium Sulfur Batteries with a Cassava-Derived Carbon Sheet as a Polysulfides Inhibitor. *New J. Chem.* **2014,** *38*, 4549-4554.

66. Zhou, F. L., Z.; Luo, X.; Wu, T.; Jiang, B.; Lu, L. L.; Yao, H. B.; Antonietti, M.; Yu, S. H., Low Cost Metal Carbide Nanocrystals as Binding and Electrocatalytic Sites for High Performance Li-S Batteries. *Nano Lett.* **2018,** *18*, 1035-1043.

67. Liang, X. R., Y.; Kwok, C. Y.; Pang, Q.; Nazar, L. F., Interwoven MXene Nanosheet/Carbon-Nanotube Composites as Li− S Cathode Hosts. *Adv. Mater.* **2017,** *29*, 1603040.

68. Park, J. Y., B.-C.; Park, J. S.; Choi, J. W.; Kim, C.; Sung, Y.-E.; Goodenough, J. B., Tungsten Disulfide Catalysts Supported on a Carbon Cloth Interlayer for High Performance Li−S Battery. *Adv. Energy Mater.* **2017,** *7*, 1602567.

69. Zhou, G. T., H.; Jin, Y.; Tao, X.; Liu, B.; Zhang, R.; Seh, Z. W.; Zhuo, D.; Liu, Y.; Sun, J.; Zhao, J.; Zu, C.; Wu, D. S.; Zhang, Q.; Cui, Y., Catalytic Oxidation of Li2S on the Surface of Metal Sulfides for Li−S Batteries. *Proc. Natl. Acad. Sci. U. S. A* **2017,** *114*, 840-845.

70. Park, J. B.-C., Y.; Sun, P. J.; Wook, C. J.; Chunjoong, K.; Yung-Eun, S.; B, G. J., Tungsten Disulfide Catalysts Supported on a Carbon Cloth Interlayer for High Performance Li−S Battery. *Adv. Energy Mater.* **2017,** *7*, 1602567.

71. Wei, Y. K., Z.; Pan, Y.; Cao, Y.; Long, D.; Wang, J.; Qiao, W.; Ling, L. , Sulfur Film Sandwiched between Few-Layered Mos2 Electrocatalysts and Conductive Reduced Graphene Oxide as a Robust Cathode for Advanced Lithium−Sulfur Batteries. *J. Mater. Chem. A* **2018,** *6*, 5899-5909.

72. Ren, J.; Zhou, Y.; Xia, L.; Zheng, Q.; Liao, J.; Long, E.; Xie, F.; Xu, C.; Lin, D., Rational design of a multidimensional N-doped porous carbon/MoS2/CNT nano-architecture hybrid for high performance lithium–sulfur batteries. *Journal of Materials Chemistry A* **2018,** *6* (28), 13835-13847.

73. Xu, H. W., X.; Li, X.; Luo, C.; Liang, F.; Orignac, E.; Zhang, J.; Chu, J. , Properties of Graphene-Metal Contacts Probed by Raman Spectroscopy. *Carbon* **2018,** *127*, 491-497.

74. Jeong, Y. C. K., J. H.; Kwon, S. H.; Oh, J. Y.; Park, J.; Jung, Y.; Lee, S. G.; Yang, S. J.; Park, C. R. , Rational Design of Exfoliated 1T MoS2@CNT-Based Bifunctional Separators for Lithium Sulfur Batteries. *J. Mater. Chem. A.* **2017,** *5*, 23909-23918.

75. Hu, L. D., C.; Lim, J.-M.; Chen, Y.; Lian, X.; Wang, M.; Li, Y.; Xiao, P.; Henkelman, G.; Xu, M. , A Highly Efficient Double- Hierarchical Sulfur Host for Advanced Lithium−Sulfur Batteries. *Chemical Science* **2018,** *9*, 666-675.

76. Han, P.; Chung, S. H.; Manthiram, A., Thin-Layered Molybdenum Disulfide Nanoparticles as an Effective Polysulfide Mediator in Lithium-Sulfur Batteries. *ACS Appl Mater Interfaces* **2018,** *10* (27), 23122-23130.

77. Zhang, Q. W., Y.; Seh, Z. W.; Fu, Z.; Zhang, R.; Cui, Y., Understanding the Anchoring Effect of Two-Dimensional Layered Materials for Lithium−Sulfur Batteries. **2015,** *15*, 3780-3786.

78. Wang, H. Z., Q.; Yao, H.; Liang, Z.; Lee, H.-W.; Hsu, P.- C.; Zheng, G.; Cui, Y., High Electrochemical Selectivity of Edge Versus Terrace Sites in Two-Dimensional Layered MoS2 Materials. *Nano Lett.* **2014,** *14*, 7138-7144.

79. Chatti, M. G., T.; King, R.; Spiccia, L.; Simonov, A. N., Vertically Aligned Interlayer Expanded MoS2 Nanosheets on a Carbon Support for Hydrogen Evolution Electrocatalysis. *Chem. Mater.* **2017,** *29*, 3092-3099.

80. Cao, P. P., J.; Li, J.; Zhai, M., Highly Conductive Carbon Black Supported Amorphous Molybdenum Disulfide for Efficient Hydrogen Evolution Reaction. *J. Power Sources* **2017,** *347*, 210-219.

81. Anichini, C., Czepa, W., Pakulski, D., Aliprandi, A., Ciesielski, A., Samori, P., Chemical sensing with 2D materials. *Chem. Soc. Rev.* **2018,** *47*, 4860-4908.

82. Islam, M. S.; Fisher, C. A., Lithium and sodium battery cathode materials: computational insights into voltage, diffusion and nanostructural properties. *Chem Soc Rev* **2014,** *43* (1), 185-204.

83. Koch, W., M. C. Holthausen, M. C., *A Chemist's Guide to Density Functional Theory*. Wiley-VCH: Weinheim, 2001.

84. Cramer, C. J., Truhlar, D. G., Density functional theory for transition metals and transition metal chemistry. *Phys. Chem. Chem. Phys.* **2009,** *11*, 10757.

85. Xu, K., Electrolytes and interphases in Li-ion batteries and beyond. *Chemical reviews* **2014,** *114* (23), 11503-11618.

86. Wu, B.; Wang, S.; Evans IV, W. J.; Deng, D. Z.; Yang, J.; Xiao, J., Interfacial behaviours between lithium ion conductors and electrode materials in various battery systems. *Journal of Materials Chemistry A* **2016,** *4* (40), 15266-15280.

87. Thangadurai, V.; Narayanan, S.; Pinzaru, D., Garnet-type solid-state fast Li ion conductors for Li batteries: critical review. *Chemical Society Reviews* **2014,** *43* (13), 4714-4727.

88. Varzi, A.; Raccichini, R.; Passerini, S.; Scrosati, B., Challenges and prospects of the role of solid electrolytes in the revitalization of lithium metal batteries. *Journal of Materials Chemistry A* **2016,** *4* (44), 17251-17259.

89. Yan, Y.; Kühnel, R.-S.; Remhof, A.; Duchêne, L.; Reyes, E. C.; Rentsch, D.; Łodziana, Z.; Battaglia, C., A Lithium Amide-Borohydride Solid-State Electrolyte with Lithium-Ion Conductivities Comparable to Liquid Electrolytes. *Adv. Energy Mater.* **2017,** *7* (19).

90. Fu, K., Gong, Y., Liu, B., Zhu, Y., Xu, S., Yao, Y., Luo, W., Wang, C., Lacey, S. D., Dai, J., Chen, Y., Mo, Y., Wachsman, E., Hu, L., Toward garnet electrolyte-based Li metal batteries: An ultrathin, highly effective, artificial solid-state electrolyte/metallic Li interface. *Science Advances* **2017,** *3* (4), e1601659.

91. Kato, Y.; Hori, S.; Saito, T.; Suzuki, K.; Hirayama, M.; Mitsui, A.; Yonemura, M.; Iba, H.; Kanno, R., High-power all-solid-state batteries using sulfide superionic conductors. *Nature Energy* **2016,** *1*, 16030.

92. Weinstein, L.; Yourey, W.; Gural, J.; Amatucci, G. G., Electrochemical Impedance Spectroscopy of Electrochemically Self-Assembled Lithium–Iodine Batteries. *J. Electrochem. Soc.* **2008,** *155* (8), A590-A598.

93. Pack, S.; Owens, B.; Wagner, J., Electrical Conductivity of the LiI-H2O-Al2O3 System. *Journal of The Electrochemical Society* **1980,** *127* (10), 2177-2179.

94. Liu, F.-C.; Liu, W.-M.; Zhan, M.-H.; Fu, Z.-W.; Li, H., An all solid-state rechargeable lithium-iodine thin film battery using LiI (3-hydroxypropionitrile) 2 as an I− ion electrolyte. *Energy & Environmental Science* **2011,** *4* (4), 1261-1264.

95. Wang, H., Li, H., Xue, B., Wang, Z., Meng, Q., Chen, L., Solid-State Composite Electrolyte LiI/3-Hydroxypropionitrile/SiO_2 for Dye-Sensitized Solar Cells. *J. Am. Chem. Soc.* **2005,** *127*, 6394-6401.

96. Shi, S.; Xu, L.; Ouyang, C.; Wang, Z.; Chen, L., Iodine ion transport in solid electrolyte LiI(C3H5NO)2: a first-principles identification. *Ionics* **2006,** *12* (6), 343-347.

97. Liu, F.-C.; Shadike, Z.; Ding, F.; Sang, L.; Fu, Z.-W., Preferential orientation of I 2-LiI (HPN) 2 film for a flexible all-solid-state rechargeable lithium–iodine paper battery. *Journal of Power Sources* **2015,** *274*, 280-285.

98. Xu, H.; Li, Y.; Zhou, A.; Wu, N.; Xin, S.; Li, Z.; Goodenough, J. B., Li3N-Modified Garnet Electrolyte for All-Solid-State Lithium Metal Batteries Operated at 40 degrees C. *Nano Lett* **2018,** *18* (11), 7414-7418.

99. Alexander, George V.; Rosero-Navarro, N. C.; Miura, A.; Tadanaga, K.; Murugan, R., Electrochemical performance of a garnet solid electrolyte based lithium metal battery with interface modification. *Journal of Materials Chemistry A* **2018,** *6* (42), 21018-21028.

100. Han, X.; Gong, Y.; Fu, K. K.; He, X.; Hitz, G. T.; Dai, J.; Pearse, A.; Liu, B.; Wang, H.; Rubloff, G.; Mo, Y.; Thangadurai, V.; Wachsman, E. D.; Hu, L., Negating interfacial impedance in garnet-based solid-state Li metal batteries. *Nat Mater* **2017,** *16* (5), 572-579.

101. Abraham, A.; Dunkin, M. R.; Huang, J.; Zhang, B.; Takeuchi, K. J.; Takeuchi, E. S.; Marschilok, A. C., Interface effects on self-forming rechargeable Li/I2-based solid state batteries. *MRS Communications* **2019,** *9* (02), 657-662.

102. Poulsen, F. W., Ionic Conductivity of Solid Lithium Iodide and Its Monohydrate. *Solid State Ionics* **1981,** *2*, 53-57.

103. Neudecker, B. J., Weppner, W., Li_9SiAlO_8: A Lithium Ion Electrolyte for Voltages above 5.4 V. *J. Electrochem. Soc.* **1996,** *143* (7), 2198-2203.

104. Schlaikjer, C. R., Liang, C. C., *J. Electrochem. Soc.* **1971,** *118* (9), 1447.

105. Berg, E. J.; Villevieille, C.; Streich, D.; Trabesinger, S.; Novák, P., Rechargeable Batteries: Grasping for the Limits of Chemistry. *Journal of The Electrochemical Society* **2015,** *162* (14), A2468-A2475.

106. Wedepohl, K. H., Composition of the continental crust. *Geochimica et Cosmochimica Acta* **1995,** *59* (7), 1217-1232.

107. Zhao, Q.; Zheng, J.; Archer, L., Interphases in Lithium–Sulfur Batteries: Toward Deployable Devices with Competitive Energy Density and Stability. *ACS Energy Letters* **2018,** *3* (9), 2104-2113.

108. Hao, F., Liu, Z., Balbuena, P. B., Mukherjee, P. P. , Mesoscale Elucidation of Self-Discharge-Induced Performance Decay in Lithium–Sulfur Batteries. *ACS Appl Mater Interfaces* **2019,** *11* (14), 13326-13333.

109. Liu, Z., Mistry, A., Mukherjee, P. P., Mesoscale Physicochemical Interactions in Lithium–Sulfur Batteries: Progress and Perspective. *J. Electrochem. Energy Convers. Storage* **2018,** *15*, 010802.

110. Gnana Kumar, G.; Chung, S. H.; Raj Kumar, T.; Manthiram, A., Three-Dimensional Graphene-Carbon Nanotube-Ni Hierarchical Architecture as a Polysulfide Trap for Lithium-Sulfur Batteries. *ACS Appl Mater Interfaces* **2018,** *10* (24), 20627-20634.

111. Xu, H.; Wang, S.; Manthiram, A., Hybrid Lithium-Sulfur Batteries with an Advanced Gel Cathode and Stabilized Lithium-Metal Anode. *Adv. Energy Mater.* **2018,** *8* (23).

112. Li, S.; Mou, T.; Ren, G.; Warzywoda, J.; Wei, Z.; Wang, B.; Fan, Z., Gel based sulfur cathodes with a high sulfur content and large mass loading for high-performance lithium–sulfur batteries. *Journal of Materials Chemistry A* **2017,** *5* (4), 1650-1657.

113. Yang, Y.; Yu, G.; Cha, J. J.; Wu, H.; Vosgueritchian, M.; Yao, Y.; Bao, Z.; Cui, Y., Improving the Performance of Lithium-Sulfur Batteries by Conductive Polymer Coating. *ACS Nano* **2011,** *5* (11), 9187-9193.

114. Sun, K.; Cama, C. A.; DeMayo, R. A.; Bock, D. C.; Tong, X.; Su, D.; Marschilok, A. C.; Takeuchi, K. J.; Takeuchi, E. S.; Gan, H., Interaction of FeS2and Sulfur in Li-S Battery System. *Journal of The Electrochemical Society* **2016,** *164* (1), A6039-A6046.

115. Sun, K.; Su, D.; Zhang, Q.; Bock, D. C.; Marschilok, A. C.; Takeuchi, K. J.; Takeuchi, E. S.; Gan, H., Interaction of CuS and Sulfur in Li-S Battery System. *Journal of The Electrochemical Society* **2015,** *162* (14), A2834-A2839.

116. Sun, K.; Zhang, Q.; Bock, D. C.; Tong, X.; Su, D.; Marschilok, A. C.; Takeuchi, K. J.; Takeuchi, E. S.; Gan, H., Interaction of TiS2 and Sulfur in Li-S Battery System. *Journal of The Electrochemical Society* **2017,** *164* (6), A1291-A1297.

117. Zhang, Q.; Bock, D. C.; Takeuchi, K. J.; Marschilok, A. C.; Takeuchi, E. S., Probing Titanium Disulfide-Sulfur Composite Materials for Li-S Batteries via In Situ X-ray Diffraction (XRD). *Journal of The Electrochemical Society* **2017,** *164* (4), A897-A901.

118. Ren, J., Zhou, Y., Xia, L., Zheng, Q., Liao, J., Long, E., Xie, F., Xu, C., Lin, D., Rational design of a multidimensional N-doped porous carbon/MoS2/CNT nano-architecture hybrid for high performance lithium–sulfur batteries. *J. Mater. Chem. A* **2018,** *6*, 13835-13847.

119. Pi, L., Li, L., Liu, K., Zhang, Q., Li, H., Zhai, T., Recent Progress on 2D Noble-Transition-Metal Dichalcogenides. *Adv. Funct. Mater.* **2019,** *29* (51), 1904932.

120. Yin, H., Dou, Y., Chen, S., Zhu, Z., Liu, P., Zhao, H., *Adv. Mater* **2019,** *31*, 1904870

.

121. Chen, Z. W., Gao, W., Zheng, W. T., Jiang, Q., Steric Hindrance in Sulfur Vacancy of Monolayer MoS2 Boosts Electrochemical Reduction of Carbon Monoxide to Methane. *ChemSusChem* **2018,** *11* (9), 1455-1459.

122. Dai, R., Wang, Y., Wang, J., Deng, X., Metal-Organic-Compound-Modified MoS2 with Enhanced Solubility for High-Performance Perovskite Solar Cells. *ChemSusChem* **2017,** *10* (14), 2869-2874.

123. Jia, Y., Wang, Z., Wang, L., Ma, Y., Wang, G., Lin, Y., Hu, X., Zhang, K., Awakening solar hydrogen evolution of MoS2 in alkalescent electrolyte through doping with Co. *ChemSusChem* **2019,** *12* (14), 3336-3342.

124. Jiang, Q., Sun, L., Bi, J., Liang, S., Li, L., Yu, Y., Wu, L., MoS2 Quantum Dots-Modified Covalent Triazine-Based Frameworks for Enhanced Photocatalytic Hydrogen Evolution. *ChemSusChem* **2018,** *11* (6), 1108-1113.

125. Kang, S., Han, S.,Kang, Y., Unveiling Electrochemical Reaction Pathways of CO2 Reduction to CN Species at S-Vacancies of MoS2. *ChemSusChem* **2019,** *12* (12), 2671–2678.

126. Lee, C., Ozden, S., Tewari, C. S., Park, O.-K., Vajtai, R., Chatterjee, K., Ajayan, P. M. , MoS2–carbon nanotube porous 3D network for enhanced oxygen reduction reaction. *ChemSusChem* **2018,** *11*, 2960-2966.

127. Liu, X., Xing, Z., Zhang, H., Wang, W., Zhang, Y., Li, Z., Wu, X., Yu, X., Zhou, W., Fabrication of 3 D Mesoporous Black TiO2/MoS2/TiO2 Nanosheets for Visible-Light-Driven Photocatalysis *ChemSusChem* **2016,** *9*, 1118–1124.

128. Sari, F. N. I., Ting, J.-M., MoS2/MoOx-Nanostructure-Decorated Activated Carbon Cloth for Enhanced Supercapacitor Performance. *ChemSusChem* **2018,** *11* (5), 897 – 906.

129. Wang, Q., Huang, J., Sun, H., Ng, Y. H., Zhang, K.-Q., Lai, Y. , MoS2 Quantum Dots@TiO2 Nanotube Arrays: An Extended-Spectrum-Driven Photocatalyst for Solar Hydrogen Evolution. *ChemSusChem* **2018,** *11* (10), 1708–1721.

130. Wu, L., Longo, A., Dzade, N. Y, Sharma, A., Hendrix, M. M. R. M., Bol, A. A., de Leeuw, N. H., Hensen, E. J. M., Hofmann, J. P., The Origin of High Activity of Amorphous MoS2 in the Hydrogen Evolution Reaction. *ChemSusChem* **2019,** *12*, 4383 – 4389.

131. Yao, K., Xu, Z., Li, Z., Liu, X., Shen, X., Cao, L., Huang, J., Synthesis of Grain-like MoS2 for High-Performance Sodium-Ion Batteries. *ChemSusChem* **2018,** *11* (13), 2130–2137.

132. Li, B.; Xu, H.; Ma, Y.; Yang, S., Harnessing the unique properties of 2D materials for advanced lithium–sulfur batteries. *Nanoscale Horizons* **2019,** *4* (1), 77-98.

133. Huang, J., Hu, X., Brady, A. B., Wu, L., Zhu, Y., E. S. Takeuchi, A. C. Marschilok, K. J. Takeuchi, , Unveiling the Structural Evolution of Ag1.2Mn8O16 under Coulombically Controlled (De)Lithiation. *Chem. Mater.* **2018,** *30* (2), 366-375.

134. Tan, L.; Li, X.; Wang, Z.; Guo, H.; Wang, J., Lightweight Reduced Graphene Oxide@MoS2 Interlayer as Polysulfide Barrier for High-Performance Lithium-Sulfur Batteries. *ACS Appl Mater Interfaces* **2018,** *10* (4), 3707-3713.

135. Jeong, Y. C.; Kim, J. H.; Kwon, S. H.; Oh, J. Y.; Park, J.; Jung, Y.; Lee, S. G.; Yang, S. J.; Park, C. R., Rational design of exfoliated 1T MoS2@CNT-based bifunctional separators for lithium sulfur batteries. *Journal of Materials Chemistry A* **2017,** *5* (45), 23909-23918.

136. Guo, P.; Liu, D.; Liu, Z.; Shang, X.; Liu, Q.; He, D., Dual functional MoS 2 /graphene interlayer as an efficient polysulfide barrier for advanced lithium-sulfur batteries. *Electrochimica Acta* **2017,** *256*, 28-36.

137. Xiang, K., Wen, X., Hu, J., Wang, S., Chen, H., Rational Fabrication of Nitrogen and Sulfur Codoped Carbon Nanotubes/MoS2 for High-Performance Lithium–Sulfur Batteries. *ChemSusChem* **2019,** *12* (15), 3602-3614.

138. Cha, E.; Patel, M. D.; Park, J.; Hwang, J.; Prasad, V.; Cho, K.; Choi, W., 2D MoS2 as an efficient protective layer for lithium metal anodes in high-performance Li-S batteries. *Nat. Nanotechnol.* **2018,** *13* (4), 337-344.

139. Liu, H.; Yi, M.; Liu, L.; Shen, Z.; Liang, S.; Zhang, X.; Ma, S., Self-Stacked, Small-Sized MoS2 Nanosheets for High-Performance Lithium-Ion Batteries. *Energy Technology* **2017,** *5* (11), 2039-2045.

140. Chen, M.; Xu, W.; Jamil, S.; Jiang, S.; Huang, C.; Wang, X.; Wang, Y.; Shu, H.; Xiang, K.; Zeng, P., Multifunctional Heterostructures for Polysulfide Suppression in High-Performance Lithium-Sulfur Cathode. *Small* **2018,** *14* (49), e1803134.

141. Zensich, M.; Jaumann, T.; Morales, G. M.; Giebeler, L.; Barbero, C. A.; Balach, J., A top-down approach to build Li2S@rGO cathode composites for high-loading lithium–sulfur batteries in carbonate-based electrolyte. *Electrochimica Acta* **2019,** *296*, 243-250.

142. You, Y.; Ye, Y.; Wei, M.; Sun, W.; Tang, Q.; Zhang, J.; Chen, X.; Li, H.; Xu, J., Three-dimensional MoS2/rGO foams as efficient sulfur hosts for high-performance lithium-sulfur batteries. *Chemical Engineering Journal* **2019,** *355*, 671-678.

143. Wei, Y.; Kong, Z.; Pan, Y.; Cao, Y.; Long, D.; Wang, J.; Qiao, W.; Ling, L., Sulfur film sandwiched between few-layered MoS2 electrocatalysts and conductive reduced graphene oxide as a robust cathode for advanced lithium–sulfur batteries. *Journal of Materials Chemistry A* **2018,** *6* (14), 5899-5909.

144. Lin, H.; Yang, L.; Jiang, X.; Li, G.; Zhang, T.; Yao, Q.; Zheng, G. W.; Lee, J. Y., Electrocatalysis of polysulfide conversion by sulfur-deficient MoS2 nanoflakes for lithium–sulfur batteries. *Energy & Environmental Science* **2017,** *10* (6), 1476-1486.

145. Xiang, K., Wen, X., Hu, J., Wang, S., Chen, H., *ChemSusChem* **2019,** *12*, 3602-3614.

146. Xu, F., Wu, L., Meng, Q., Kaltak, M., Huang, J., Durham, J. L., Fernandez-Serra, M., Sun, L, Marschilok, A. C., Takeuchi, E. S., Takeuchi, K. J., Hybertsen, M. S., Zhu, Y., Visualization of lithium-ion transport and phase evolution within and between manganese oxide nanorods. *Nat. Commun.* **2017,** *8*, 15400.

147. Dirlam, P. T.; Park, J.; Simmonds, A. G.; Domanik, K.; Arrington, C. B.; Schaefer, J. L.; Oleshko, V. P.; Kleine, T. S.; Char, K.; Glass, R. S.; Soles, C. L.; Kim, C.; Pinna, N.; Sung, Y. E.; Pyun, J., Elemental Sulfur and Molybdenum Disulfide Composites for Li-S Batteries with Long Cycle Life and High-Rate Capability. *ACS Appl Mater Interfaces* **2016,** *8* (21), 13437-48.

148. Bugga, R. V.; Jones, S. C.; Pasalic, J.; Seu, C. S.; Jones, J.-P.; Torres, L., Metal Sulfide-Blended Sulfur Cathodes in High Energy Lithium-Sulfur Cells. *J. Electrochem. Soc.* **2017,** *164* (2), A265-A276.

149. Wang, H.; Zhang, Q.; Yao, H.; Liang, Z.; Lee, H. W.; Hsu, P. C.; Zheng, G.; Cui, Y., High electrochemical selectivity of edge versus terrace sites in two-dimensional layered MoS2 materials. *Nano Lett* **2014,** *14* (12), 7138-44.

150. Kamphaus, E. P.; Balbuena, P. B., Long-Chain Polysulfide Retention at the Cathode of Li–S Batteries. *The Journal of Physical Chemistry C* **2016,** *120* (8), 4296-4305.

151. Abraham, A., Wang, L., Quilty, C. D., Lutz, D. M., McCarthy, A. H., Tang, C. R., Dunkin, M. R., Housel, L. M., Takeuchi, E. S., Marschilok, A. C., Takeuchi, K. J., Defect Control in the Synthesis of 2D MoS2 Nanosheets: Polysulfide Trapping in Composite Sulfur Cathodes for Li–S Batteries. *ChemSusChem* **2019,** *12*, DOI: 10.1002/cssc.201903028.

152. Wang, L., Abraham, A., Lutz, D. M., Quilty, C. D., Takeuchi, E. S., Takeuchi, K. J., Marschilok, A. C., Toward Environmentally Friendly Lithium Sulfur Batteries: Probing the Role of Electrode Design in MoS2-Containing Li–S Batteries with a Green Electrolyte. *ACS Sustainable Chem. Eng.* **2019,** *7*, 5209-5222.

153. Xie, J.; Zhang, H.; Li, S.; Wang, R.; Sun, X.; Zhou, M.; Zhou, J.; Lou, X. W.; Xie, Y., Defect-rich MoS2 ultrathin nanosheets with additional active edge sites for enhanced electrocatalytic hydrogen evolution. *Adv Mater* **2013,** *25* (40), 5807-13.

154. Wu, Z.; Li, B.; Xue, Y.; Li, J.; Zhang, Y.; Gao, F., Fabrication of defect-rich MoS2ultrathin nanosheets for application in lithium-ion batteries and supercapacitors. *J. Mater. Chem. A* **2015,** *3* (38), 19445-19454.

155. Liu, J.; Chen, H.; Chen, W.; Zhang, Y.; Zheng, Y., New Insight into the "Shuttle Mechanism" of Rechargeable Lithium-Sulfur Batteries. *ChemElectroChem* **2019,** *6* (10), 2782-2787.

156. Abraham, A., Wang, L., Quilty, C. D., Lutz, D. M., McCarthy, A. H., Tang, C. R., Dunkin, M. R., Housel, L. M., Takeuchi, E. S., Marschilok, A. C., Takeuchi, K. J., *ChemSusChem* **2019,** *12*, DOI: 10.1002/cssc.201903028.

157. Gu, Y., Wu, A., Sohn, H., Nicoletti, C., Iqbal, Z., Federici, J. F., Fabrication of rechargeable lithium ion batteries using water-based inkjet printed cathodes. *J. Manufact. Process* **2015,** *20*, 198-205.

158. Li, H., Zhang, Q., Yap, C. C. R., Tay, B. K., Edwin, T. H. T., Oliver, A., Baillargeat, D., From Bulk to Monolayer MoS2: Evolution of Raman Scattering. *Adv. Funct. Mater.* **2012,** *22* (7), 1385-1390.

159. Vilá, R. A., Rao, R., Muratore, C., Bianco, E., Robinson, J. A., Maruyama, B., Glavin, N. R., In situ crystallization kinetics of two-dimensional MoS2. *2D Mater.* **2017,** *5* (1), 011009.

160. Wang, T., Liu, C., Xu, J., Zhu, Z., Liu, E., Hu, T., Li, C., Jiang, F., Thermoelectric performance of restacked MoS2 nanosheets thin-film. *Nanotechnology* **2016,** *27* (28), 285703.

161. Benítez, A., Di Lecce, D., Elia, G. A., Caballero, A., Morales, J. Hassoun, J., A Lithium-Ion Battery using a 3 D-Array Nanostructured Graphene-Sulfur Cathode and a Silicon Oxide-Based Anode. *ChemSusChem* **2018,** *11* (9), 1512 – 1520.

162. Seh, Z. W.; Sun, Y.; Zhang, Q.; Cui, Y., Designing high-energy lithium–sulfur batteries. *Chemical Society Reviews* **2016,** *45* (20), 5605-5634.

163. Sigita, U.; Tiphaine, P.; Petr, N., Progress Towards Commercially Viable Li–S Battery Cells. *Adv. Energy Mater.* **2015,** *5* (16), 1500118.

164. Manthiram, A.; Fu, Y.; Chung, S.-H.; Zu, C.; Su, Y.-S., Rechargeable Lithium–Sulfur Batteries. *Chemical Reviews* **2014,** *114* (23), 11751-11787.

165. Min, W.; Yi, C.; Amruth, B.; Yaroslav, L.; Amanda, S.; Mangilal, A.; Ying, M.; Yongzhu, F., Organotrisulfide: A High Capacity Cathode Material for Rechargeable Lithium Batteries. *Angewandte Chemie International Edition* **2016,** *55* (34), 10027-10031.

166. Wang, X. S.; Du, K. Z.; Wang, C.; Ma, L. X.; Zhao, B. L.; Yang, J. F.; Li, M. X.; Zhang, X. X.; Xue, M. Q.; Chen, J. T., Unique Reversible Conversion-Type Mechanism Enhanced Cathode Performance in Amorphous Molybdenum Polysulfide. *Acs Applied Materials & Interfaces* **2017,** *9* (44), 38606-38611.

167. Ye, H. L.; Ma, L.; Zhou, Y.; Wang, L.; Han, N.; Zhao, F. P.; Deng, J.; Wu, T. P.; Li, Y. G.; Lu, J., Amorphous MoS3 as the sulfur-equivalent cathode material for room-temperature Li-S and Na-S batteries. *P Natl Acad Sci USA* **2017,** *114* (50), 13091-13096.

168. Grayfer, E. D.; Pazhetnov, E. M.; Kozlova, M. N.; Artemkina, S. B.; Fedorov, V. E., Anionic Redox Chemistry in Polysulfide Electrode Materials for Rechargeable Batteries. *Chemsuschem* **2017,** *10* (24), 4805-4811.

169. Doan-Nguyen, V. V. T.; Subrahmanyam, K. S.; Butala, M. M.; Gerbec, J. A.; Islam, S. M.; Kanipe, K. N.; Wilson, C. E.; Balasubramanian, M.; Wiaderek, K. M.; Borkiewicz, O. J.; Chapman, K. W.; Chupas, P. J.; Moskovits, M.; Dunn, B. S.; Kanatzidis, M. G.; Seshadri, R., Molybdenum Polysulfide Chalcogels as High-Capacity, Anion-Redox-Driven Electrode Materials for Li-Ion Batteries. *Chem Mater* **2016,** *28* (22), 8357-8365.

170. Dharmadasa, I.; Haigh, J., Strengths and advantages of electrodeposition as a semiconductor growth technique for applications in macroelectronic devices. *Journal of the Electrochemical Society* **2006,** *153* (1), G47-G52.

171. Gurrappa, I.; Binder, L., Electrodeposition of nanostructured coatings and their characterization—A review. *Science and Technology of Advanced Materials* **2008,** *9* (4), 043001.

172. Wang, L., Abraham, A., Lutz, D. M., Quilty, C. D., Takeuchi, E. S., Takeuchi, K. J., Marschilok, A. C., *ACS Sustainable Chem. Eng.* **2019,** *7*, 5209-5222.

173. Lee, S., Zhu, S., Milleville, C. C., Lee, C.-Y., Chen, P., Takeuchi, K. J., Takeuchi, E. S., Marschilok, A. C., Metal-Air Electrochemical Cells: Silver-Polymer-Carbon Composite Air Electrodes. *Electrochemical and Solid-State Letters* **2010,** *13* (11), A162-A164.

174. DiLeo, R. A., Zhang, Q., Marschilkok A. C., Takeuchi, K. J., Takeuchi, E. S., Composite Anodes for Secondary Magnesium Ion Batteries Prepared via Electrodeposition of Nanostructured Bismuth on Carbon Nanotube Substrates. *Electrochemistry Letters* **2015,** *4* (1), A10.

175. Wheeler, G. P., Choi, K.-S., Photoelectrochemical Properties and Stability of Nanoporous p-Type LaFeO3 Photoelectrodes Prepared by Electrodeposition. *ACS Energy Lett.* **2017,** *2* (10), 2378-2382.

176. Koza, J. A., He, Z., Miller, A. S., Switzer, J. A., Electrodeposition of Crystalline Co3O4—A Catalyst for the Oxygen Evolution Reaction. *Chem. Mater.* **2012,** *24* (18), 3567-3573.

177. Vertegel, A. A., Vohannan, E. W., Shumsky, M. G., Switzer, J. A., Epitaxial Electrodeposition of orthorhombic alpha-PbO2 on (100)-oriented Single-Crystal Au. *J. Electrochem. Soc.* **2001,** *148*, C253-C256.

178. Schulze, M. C., Belson, R. M., Kraynak, L. A., Preito, A. L., Electrodeposition of Sb/CNT composite films as anodes for Li- and Na-ion batteries. *Energy Storage Materials* **2019,** *25*, 572-584.

179. Marschilok, A. C., Lee, S. H., Milleville, C. C., Chen, P., Takeuchi, E. S., Takeuchi, K. J., Three-dimensional carbon-conductive polymer-silver composite air electrodes for non-aqueous metal air batterie. *Journal of Composite Materials* **2013,** *47*, 33.

180. Merki, D.; Fierro, S.; Vrubel, H.; Hu, X. L., Amorphous molybdenum sulfide films as catalysts for electrochemical hydrogen production in water. *Chemical Science* **2011,** *2* (7), 1262-1267.

181. Murugesan, S.; Akkineni, A.; Chou, B. P.; Glaz, M. S.; Bout, D. A. V.; Stevenson, K. J., Room Temperature Electrodeposition of Molybdenum Sulfide for Catalytic and Photoluminescence Applications. *Acs Nano* **2013,** *7* (9), 8199-8205.

182. Vrubel, H., Hu, X. L., Growth and Activation of an Amorphous Molybdenum Sulfide Hydrogen Evolving Catalyst. *ACS Catalysis* **2013,** *3* (9), 2002-2011.

183. Maijenburg, A. W., Regis, M., Hattori, A. N., Tanaka, H., Choi, K. S., ten Elshof, J. E., MoS2 nanocube structures as catalysts for electrochemical H2 evolution from acidic aqueous solutions. *ACS Appl Mater Interfaces* **2014,** *6*, 2003.

184. Vrubel, H., Hu, X. L., *ACS Catalysis* **2013,** *3*, 2002.

185. Weber, T., Muijsers, J. C., Niemantsverdriet, J. W., Structure of amorphous MoS3. *J. Phys. Chem-US* **1995,** *99*, 9194.

186. Matsuyama, T., Deguchi, M., Hayashi, A., Tatsumisago, M., Ozaki, T., Togawa, Y., Mori, S., Structure Analyses of Amorphous MoS3 Active Materials in All-Solid-State Lithium Batteries. *Electrochemistry* **2015,** *83* (10), 889-893.

187. Brown, N. M. D., Cui, N., McKinley, A., An XPS study of the surface modification of natural MoS2 following treatment in an RF-oxygen plasma. *Appl. Surf. Sci.* **1998,** *134*, 11-21.

188. Bard, A. J., Fan, F.-R. F., Kwak, J., Lev, O., Scanning electrochemical microscopy. Introduction and principles. *Anal. Chem.* **1989,** *61*, 132-138.

189. Bard, A. J., Denuault, G., Lee, C., Mandler, D., Wipf, D. O., Scanning Electrochemical Microscopy: A New Technique for the Characterization and Modification of Surfaces. *Acc. Chem. Res.* **1990,** *23*, 357-363.

190. Bard, A. J., Fan, F.-R. F., Kwak, J., Levo, O., Scanning electrochemical microscopy. Introduction and principles. *Analytical Chemistry* **1989,** *61*, 132.

191. Bard, A. J., Mirkin, M. V., *Scanning Electrochemical Microscopy*. CRC Press: 2012.

192. Polcari, D., Dauphin-Ducharme, P., Mauzeroll, J., Scanning Electrochemical Microscopy: A Comprehensive Review of Experimental Parameters from 1989 to 2015. *Chemical Reviews* **2016,** *116* (22), 13234-13278.

193. Polcari, D., Dauphin-Ducharme, P., Mauzeroll, J., *Chemical Reviews* **2016,** *116*, 13234.

194. Eckhard, K., Schuhmann, W., Alternating current techniques in scanning electrochemical microscopy (AC-SECM). *Analyst* **2008,** *133* (11), 1486-1497.

195. Baranski, A., Diakowski, P., Application of AC impedance techniques to Scanning Electrochemical Microscopy. *Journal of Solid State Electrochemistry* **2004,** *8*, 683-692.

196. Zhang, L., Sun, D., Kang, J., Feng, J., Bechtel, H. A., Wang, L.-W., Cairns, E. J., Guo, J., Electrochemical Reaction Mechanism of the MoS2 Electrode in a Lithium-Ion Cell Revealed by in Situ and Operando X-ray Absorption Spectroscopy. *Nano Lett* **2018,** *18* (2), 1466-1475.

197. Bock, D. C. K., K. C.; Wang, J.; Zhang, W.; Wang, F.; Wang, J.; Marschilok, A. C.; Takeuchi, K. J.; Takeuchi, E. S. , 2D Cross Sectional Analysis and Associated Electrochemistry of Composite Electrodes Containing Dispersed Agglomerates of Nanocrystalline Magnetite, Fe3O4. *ACS Appl. Mater. Interfaces* **2015,** *7*, 13457-13466.

198. Hemminger, J. C., G.; Sarrao, J. *From Quanta to the Continuum: Opportunities for Mesoscale Science: A Report from the Basic Energy Sciences Advisory Committee; Department of Energy Office of Basic Energy Sciences "Basic Research Needs" Report Series*; 2012; pp pp 1-75.

199. Rubloff, G. W. L., S. B., New science at the meso frontier: Dense nanostructure architectures for electrical energy storage. *Curr. Opin. Solid State Mater. Sci.* **2015,** *19*, 227-234.

200. Abraham, A.; Housel, L. M.; Lininger, C. N.; Bock, D. C.; Jou, J.; Wang, F.; West, A. C.; Marschilok, A. C.; Takeuchi, K. J.; Takeuchi, E. S., Investigating the Complex Chemistry of Functional Energy Storage Systems: The Need for an Integrative, Multiscale (Molecular to Mesoscale) Perspective. *ACS Cent Sci* **2016,** *2* (6), 380-7.

201. Hussain, S. H., K.; Gearhart, J.; Geiss, K.; Schlager, J., In vitro toxicity of nanoparticles in BRL 3A rat liver cells. *Toxicol. In Vitro* **2005,** *19*, 975-983.

202. Bruck, A. C., C.; Gannett, C.; Marschilok, A. C.; Takeuchi, E. S.; Takeuchi, K. J. , Nanocrystalline iron oxide based electroactive materials in lithium ion batteries: The critical roles of crystallite size, morphology, and electrode heterostructure on battery relevant electrochemistry. *Inorg. Chem. Front.* **2016,** *3*, 26-40.

203. Fleet, M. E., The structure of magnetite. *Acta Crystallogr., Sect. B* **1981,** *37* (4), 917-920.

204. Amatucci, G. G. P., N., Fluoride based electrode materials for advanced energy storage devices. *J. Fluorine Chem.* **2007,** *128*, 243-262.

205. Malini, R. U., U.; Sheela, T.; Ganesan, M.; Renganathan, N., Conversion reactions: a new pathway to realise energy in lithium-ion battery□review. *Ionics* **2009,** *15*, 301-307.

206. Poizot, P. L., S.; Grugeon, S.; Dupont, L.; Tarascon, J, Nano-sized transition-metal oxides as negative-electrode materials for lithium-ion batteries. *Nature* **2000,** *407*, 496-499.

207. Kim, S.-W. P., N.; Chernova, N. A.; Omenya, F.; Gao, P.; Whittingham, M. S.; Amatucci, G. G.; Su, D.; Wang, F., Structure Stabilization by Mixed Anions in Oxyfluoride Cathodes for High- Energy Lithium Batteries. *ACS Nano* **2015,** *9*, 10076-10084.

208. Wang, F. K., S.-W.; Seo, D.-H.; Kang, K.; Wang, L.; Su, D.; Vajo, J. J.; Wang, J.; Graetz, J., Ternary metal fluorides as high-energy cathodes with low cycling hysteresis. *Nat. Commun.* **2015,** *6*, 6668.

209. Thackeray, M. D., W.; Goodenough, J. , Structural characterization of the lithiated iron oxides LixFe3O4 and LixFe2O3. *Mater. Res. Bull.* **1982,** *17*, 785-793.

210. Fontcuberta, J. R., J.; Pernet, M.; Longworth, G.; Goodenough, J., Structural and magnetic characterization of the lithiated iron oxide LixFe3O4. *J. Appl. Phys.* **1986,** *59*, 1918-1926.

211. Thackeray, M. D. P., L.; De Kock, A.; Johnson, P.; Nicholas, V.; Adendorff, K. , Spinel electrodes for lithium batteries-a review. *J. Power Sources* **1987,** *21*, 1-8.

212. Islam, M. C., C., Lithium insertion into Fe3O4. *J. Solid State Chem.* **1988,** *77*, 180-189.

213. Yamada, T. M., K.; Kume, K.; Yoshikawa, H.; Awaga, K., The solid-state electrochemical reduction process of magnetite in Li batteries: in situ magnetic measurements toward electrochemical magnets. *J. Mater. Chem. C* **2014,** *2*, 5183-51888.

214. He, K. L., J.; Yu, X.; Meng, Q.; Hu, E.; Sun, K.; Yang, X.-Q.; Zhu, Y.; Gan, H.; Stach, E. A.; Su, D.; Zhang, S.; Yun, H.; Murray, C. B.; Zhu, Y.; Mo, Y., Visualizing non-equilibrium lithiation of spinel oxide via in situ transmission electron microscopy. *Nat. Commun.* **2016,** *7*, 11441.

215. Thackeray, M. C., J., A preliminary investigation of the electrochemical performance of α-Fe2O3 and Fe3O4 cathodes in high-temperature cells. *Mater. Res. Bull.* **1981,** *16*, 591-597.

216. Menard, M. C. T., K. J.; Marschilok, A. C.; Takeuchi, E. S, Electrochemical discharge of nanocrystalline magnetite: structure analysis using X-ray diffraction and X-ray absorption spectroscopy. *Phys. Chem. Chem. Phys.* **2013,** *15*, 18539-18548.

217. Munoz, M. A., P.; Farges, F. , Continuous Cauchy wavelet transform analyses of EXAFS spectra: a qualitative approach. *Am. Mineral.* **2003,** *88*, 694-700.

218. Funke, H. S., A. C.; Chukalina, M., Wavelet analysis of extended x-ray absorption fine structure data. *Phys. Rev. B: Condens. Matter Mater. Phys.* **2005,** *71*, 094110.

219. Timoshenko, J. K., A., Wavelet data analysis of EXAFS spectra. *Comput. Phys. Commun.* **2009,** *180*, 920-925.

220. Otal, E. H. S., E.; Aguirre, M. H.; Fabregas, I. O.; Kim, M., Structural characterization and EXAFS wavelet analysis of Yb doped ZnO by wet chemistry route. *J. Alloys Compd.* **2015,** *622*, 115-120.

221. Pelliccione, C. J. L., Y. R.; Marschilok, A. C.; Takeuchi, K. J.; Takeuchi, E. S., X-ray absorption spectroscopy of lithium insertion and de-insertion in copper birnessite nanoparticle electrodes. *Phys. Chem. Chem. Phys.* **2016,** *18*, 2959-2967.

222. Manceau, A. G., A. I.; Drits, V. A., Structural chemistry of Mn, Fe, Co, and Ni in manganese hydrous oxides; Part II, information from EXAFS spectroscopy and electron and X-ray diffraction. *Am. Mineral.* **1992,** *77*, 1144-1157.

223. Beale, A. M. W., B. M., EXAFS as a tool to interrogate the size and shape of mono and bimetallic catalyst nanoparticles. *Phys. Chem. Chem. Phys.* **2010,** *12*, 5562-5574.

224. Srabionyan, V. V. B., A. L.; Pryadchenko, V. V.; Avakyan, L. A.; van Bokhoven, J. A.; Bugaev, L. A., EXAFS study of size dependence of atomic structure in palladium nanoparticles. *J. Phys. Chem. Solids* **2014,** *75*, 470-476.

225. Duan, H. G., J.; Liang, J. , Synthesis and rate performance of Fe3O4-based Cu nanostructured electrodes for Li ion batteries. *J. Power Sources* **2011,** *196*, 4779-4784.

226. Larcher, D. M., C.; Bonnin, D.; Chabre, Y.; Masson, V.; Leriche, J. B.; Tarascon, J. M., Effect of particle size on lithium intercalation into alpha-Fe2O3. *J. Electrochem. Soc. 150*, A133-A139.

227. Xiong, Q. Q. T., J. P.; Lu, Y.; Chen, J.; Yu, Y. X.; Qiao, Y. Q.; Wang, X. L.; Gu, C. D., Synthesis of hierarchical hollow-structured single-crystalline magnetite (Fe3O4) microspheres: the highly powerful storage versus lithium as an anode for lithium ion batteries. *J. Phys. Chem. C* **2012,** *116*, 6495-6502.

228. Okubo, M. H., E.; Kim, J.; Enomoto, M.; Kojima, N.; Kudo, T.; Zhou, H.; Honma, I. , Nanosize Effect on High-Rate Li-Ion Intercalation in LiCoO2 Electrode. *J. Am. Chem. Soc.* **2007,** *129*, 7444-7452.

229. Knehr, K. W. B., N. W.; Cama, C. A.; Bock, D. C.; Lin, Z.; Lininger, C. N.; Marschilok, A. C.; Takeuchi, K. J.; Takeuchi, E. S.; West, A. C., Modeling the Mesoscale Transport of Lithium-Magnetite Electrodes Using Insight from Discharge and Voltage Recovery Experiments. *J. Electrochem. Soc.* **2015,** *162*, A2817-A2826.

230. Zhu, S. L. M., A. C.; Takeuchi, E. S.; Yee, G. T.; Wang, G. B.; Takeuchi, K. J., Nanocrystalline Magnetite: Synthetic Crystallite Size Control and Resulting Magnetic and Electrochemical Properties. *J. Electrochem. Soc.* **2010,** *157*, A1158-A1163.

231. Muraliganth, T. M., A. V.; Manthiram, A., Facile synthesis of carbon-decorated single-crystalline Fe3O4 nanowires and their application as high performance anode in lithium ion batteries. *Chem. Commun.* **2009**, 7360-7362.

232. Komaba, S. M., T.; Ogata, A., Electrochemical activity of nanocrystalline Fe3O4 in aprotic Li and Na salt electrolytes. *Electrochem. Commun.* **2008,** *10*, 1276-1279.

233. Komaba, S. M., T.; Yabuuchi, N.; Ogata, A.; Yoshida, H.; Yamada, Y. , Electrochemical insertion of Li and Na ions into nanocrystalline Fe3O4 and alpha-Fe2O3 for rechargable batteries. *J. Electrochem. Soc.* **2010,** *157*, A60-A65.

234. Zhu, S. M., A. C.; Takeuchi, E. S.; Takeuchi, K. J., Crystallite size control and resulting electrochemistry of magnetite, Fe3O4. *Electrochem. Solid-State Lett.* **2009,** *12*, A91-A94.

235. Zhu, S.; Marschilok, A. C.; Takeuchi, E. S.; Takeuchi, K. J., Crystallite Size Control and Resulting Electrochemistry of Magnetite, Fe_3O_4. *Electrochemical and Solid-State Letters* **2009,** *12* (4), A91-A94.

236. Sasaki, S., Radial distribution of electron density in magnetite, Fe3O4. *Acta Crystallogr., Sect. B: Struct. Sci.* **1997,** *B53*, 762-766.

237. Menard, M. C. M., A. C.; Takeuchi, K. J.; Takeuchi, E. S. , Variation in the iron oxidation states of magnetite nanocrystals as a function of crystallite size: The impact on electrochemical capacity. *Electrochim. Acta* **2013,** *94*, 320-326.

238. Li, J. L. A., B. L.; Kiggans, J.; Daniel, C.; Wood, D. L., Lithium Ion Cell Performance Enhancement Using Aqueous LiFePO4 Cathode Dispersions and Polyethyleneimine Dispersant. *J. Electrochem. Soc.* **2013,** *160* (A201-A206).

239. Cornut, R. L., D.; Schougaard, S. B., Ohmic Drop in LiFePO4 Based Lithium Battery Cathodes Containing Agglomerates. *J. Electrochem. Soc.* **2012,** *159*, A822-A827.

240. Knehr, K. W. B., N. W.; Cama, C. A.; Bock, D. C.; Lin, Z.; Lininger, C. N.; Marschilok, A. C.; Takeuchi, K. J.; Takeuchi, E. S.; West, A. C. , Mesoscale Transport in Magnetite Electrodes for Lithium- Ion Batteries. *ECS Trans.* **2015,** *69*, 7-19.

241. Bock, D. C. P., C. J.; Knehr, K. W.; Wang, J.; Zhang, W.; Wang, F.; Wang, J.; West, A. C.; Marschilok, A. C.; Takeuchi, K. J.; Takeuchi, E. S. , Dispersion of Iron Oxide, Fe3O4, Nanomaterials in Composite Electrodes: Impact on Functional Electrochemistry. *ACS Appl. Mater. Interfaces* **2016,** *8*, 11418-11430.

242. Jiang, Y. J., Z. J.; Yang, L. F.; Cheng, S.; Liu, M. L., , A High-Performance Anode for Lithium Ion Batteries: Fe3O4 Microspheres Encapsulated in Hollow Graphene Shells. *J. Mater. Chem. A* **2015,** *3*, 11847-11856.

243. Qu, Q. T. C., J. M.; Li, X. X.; Gao, T.; Shao, J.; Zheng, H. H., Strongly Coupled 1d Sandwich-Like C@ Fe3O4@C Coaxial Nanotubes with Ultrastable and High Capacity for Lithium-Ion Batteries. *J. Mater. Chem. A* **2015,** *3*, 18289-18295.

244. He, Y.; Huang, L.; Cai, J. S.; Zheng, X. M.; Sun, S. G., Structure and electrochemical performance of nanostructured Fe_3O_4/carbon nanotube composites as anodes for lithium ion batteries. *Electrochimica Acta* **2010,** *55* (3), 1140-1144.

245. Yang, L.; Hu, J. H.; Dong, A. G.; Yang, D., Novel Fe_3O_4-CNTs nanocomposite for Li-ion batteries with enhanced electrochemical performance. *Electrochimica Acta* **2014,** *144*, 235-242.

246. Zhu, S. L.; Marschilok, A. C.; Takeuchi, E. S.; Yee, G. T.; Wang, G. B.; Takeuchi, K. J., Nanocrystalline Magnetite: Synthetic Crystallite Size Control and Resulting Magnetic and Electrochemical Properties. *Journal of the Electrochemical Society* **2010,** *157* (11), A1158-A1163.

247. Cui, Z. M.; Hang, L. Y.; Song, W. G.; Guo, Y. G., High-Yield Gas-Liquid Interfacial Synthesis of Highly Dispersed Fe_3O_4 Nanocrystals and Their Application in Lithium-Ion Batteries. *Chemistry of Materials* **2009,** *21* (6), 1162-1166.

248. Durham, J.; Takeuchi, E. S.; Marschilok, A. C.; Takeuchi, K. J., Nanocrystalline Iron Oxides Prepared via Co-Precipitation for Lithium Battery Cathode Applications. *ECS Transactions* **2015,** *66* (9), 111-120.

249. Shi, Y.; Zhang, J.; Bruck, A. M.; Zhang, Y.; Li, J.; Stach, E. A.; Takeuchi, K. J.; Marschilok, A. C.; Takeuchi, E. S.; Yu, G., A Tunable 3D Nanostructured Conductive Gel Framework Electrode for High-Performance Lithium Ion Batteries. *Adv. Mater.* **2017,** *29* (22), 1603922.

250. Nitta, N.; Wu, F. X.; Lee, J. T.; Yushin, G., Li-ion battery materials: present and future. *Materials Today* **2015,** *18* (5), 252-264.

251. Lee, K. T.; Jeong, S.; Cho, J., Roles of Surface Chemistry on Safety and Electrochemistry in Lithium Ion Batteries. *Accounts Chem Res* **2013,** *46* (5), 1161-1170.

252. Luo, L.; Yang, H.; Yan, P.; Travis, J. J.; Lee, Y.; Liu, N.; Molina Piper, D.; Lee, S.-H.; Zhao, P.; George, S. M.; Zhang, J.-G.; Cui, Y.; Zhang, S.; Ban, C.; Wang, C.-M., Surface-Coating Regulated Lithiation Kinetics and Degradation in Silicon Nanowires for Lithium Ion Battery. *ACS Nano* **2015,** *9* (5), 5559-5566.

253. Wang, D.; Xu, T.; Li, Y.; Pan, D.; Lu, X.; Hu, Y.-S.; Dai, S.; Bai, Y., Integrated Surface Functionalization of Li-Rich Cathode Materials for Li-Ion Batteries. *Acs Appl Mater Inter* **2018,** *10* (48), 41802-41813.

254. Dannehl, N.; Steinmüller, S. O.; Szabó, D. V.; Pein, M.; Sigel, F.; Esmezjan, L.; Hasenkox, U.; Schwarz, B.; Indris, S.; Ehrenberg, H., High-Resolution Surface Analysis on Aluminum Oxide-Coated Li1.2Mn0.55Ni0.15Co0.1O2 with Improved Capacity Retention. *Acs Appl Mater Inter* **2018,** *10* (49), 43131-43143.

255. Cho, J.; Kim, Y.-W.; Kim, B.; Lee, J.-G.; Park, B., A Breakthrough in the Safety of Lithium Secondary Batteries by Coating the Cathode Material with AlPO4 Nanoparticles. *Angewandte Chemie International Edition* **2003,** *42* (14), 1618-1621.

256. Cho, J.; Kim, Y. J.; Kim, T. J.; Park, B., Zero-strain intercalation cathode for rechargeable Li-ion cell. *Angew Chem Int Edit* **2001,** *40* (18), 3367.

257. Cho, J.; Kim, Y. J.; Park, B., Novel LiCoO2 cathode material with Al2O3 coating for a Li ion cell. *Chemistry of Materials* **2000,** *12* (12), 3788-3791.

258. Peng, L.; Fang, Z.; Li, J.; Wang, L.; Bruck, A. M.; Zhu, Y.; Zhang, Y.; Takeuchi, K. J.; Marschilok, A. C.; Stach, E. A.; Takeuchi, E. S.; Yu, G., Two-Dimensional Holey Nanoarchitectures Created by Confined Self-Assembly of Nanoparticles via Block Copolymers: From Synthesis to Energy Storage Property. *ACS Nano* **2018,** *12* (1), 820-828.

259. Bock, D. C.; Pelliccione, C. J.; Zhang, W.; Wang, J.; Knehr, K. W.; Wang, J.; Wang, F.; West, A. C.; Marschilok, A. C.; Takeuchi, K. J.; Takeuchi, E. S., Dispersion of Nanocrystalline Fe3O4 within Composite Electrodes: Insights on Battery-Related Electrochemistry. *ACS Appl Mater Interfaces* **2016,** *8* (18), 11418-30.

260. Wang, L.; Zhang, Y. M.; McBean, C. L.; Scofield, M. E.; Yin, J. F.; Marschilok, A. C.; Takeuchi, K. J.; Takeuchi, E. S.; Wong, S. S., Understanding the Effect of Preparative Approaches in the Formation of "Flower-like" Li4Ti5O12-Multiwalled Carbon Nanotube CompositeMotifs with Performance as High-Rate Anode Materials for Li-Ion Battery Applications. *Journal of the Electrochemical Society* **2017,** *164* (2), A524-A534.

261. Wang, L.; Li, Y. R.; Li, J.; Zou, S.; Stach, E. A.; Takeuchi, K. J.; Takeuchi, E. S.; Marschilok, A. C.; Wong, S. S., Correlating Preparative Approaches with Electrochemical Performance of Fe3O4-MWNT Composites Used as Anodes in Li-Ion Batteries. *ECS Journal of Solid State Science and Technology* **2017,** *6* (6), M3122-M3131.

262. Wang, L. Y., S. Y.; Zhang, Q.; Zhang, Y. M.; Li, Y. R.; Lewis, C. S.; Takeuchi, K. J.; Marschilok, A. C.; Takeuchi, E. S.; Wong, S. S., Morphological and Chemical Tuning of High-Energy-Density Metal Oxides for Lithium Ion Battery Electrode Applications. *ACS Energy Lett.* **2017,** *2*, 1465-1478.

263. Gribanova, E. V., Kuchek, A. E., Larionov, M. I., Factors influencing the contact angle value. The contact angle, as a characteristic of the properties of solid surfaces. *Izv. Akad. Nauk. Seriya Khimicheskaya* **2016,** *1*, 1-13.

264. Xu, W. X., J.; Zhang, J.; Wang, D.; Zhang, J.-G., Optimization of nonaqueous electrolytes for primary lithium / air batteries operated in ambient environment *J. Electrochem. Soc.* **2009,** *156*, A773-A779.

265. Wang, F. L., X., Effects of the Electrode Wettability on the Deep Discharge Capacity of Li-O2 Batteries. *ACS Omega* **2018,** *3*, 6006-6012.

266. Wang, L.; Housel, L. M.; Bock, D. C.; Abraham, A.; Dunkin, M. R.; McCarthy, A. H.; Wu, Q.; Kiss, A.; Thieme, J.; Takeuchi, E. S.; Marschilok, A. C.; Takeuchi, K. J., Deliberate Modification of Fe3O4 Anode Surface Chemistry: Impact on Electrochemistry. *ACS Appl Mater Interfaces* **2019,** *11* (22), 19920-19932.

267. Cortés, M.; Gómez, E.; Sadler, J.; Vallés, E., Adsorption of organic layers over electrodeposited magnetite (Fe3O4) thin films. *Electrochimica Acta* **2011,** *56* (11), 4087-4091.

268. Pan, H., Shao, Y., Yan, P., Cheng, Y., Han, K. S., Nie, Z., Wang, C., Yang, J., Li, X., Bhattacharya, P., Mueller, K. T., Liu, J. , Reversible aqueous zinc/manganese oxide energy storage from conversion reactions. *Nat Energy* **2016,** *1*, 16039.

269. Xu, C., Li, B., Du, H., Kang, F. , Energetic Zinc Ion Chemistry: The Rechargeable Zinc Ion Battery. *Angewandte Chemie International Edition* **2012,** *51*, 933.

270. Ko, J. S., Sassin, M. B., Parker, J. F., Rolison, D. R., Long, J. W., Combining battery-like and pseudocapacitive charge storage in 3D MnOx@carbon electrode architectures for zinc-ion cells. *Sustainable Energy & Fuels* **2018,** *2*, 626-636.

271. Fang, G., Zhu, C., Chen, M., Zhou, J., Tang, B., Cao, X., Zheng, X., Pan, A., Liang, S. , Suppressing Manganese Dissolution in Potassium Manganate with Rich Oxygen Defects Engaged High-Energy-Density and Durable Aqueous Zinc-Ion Battery. *Advanced Functional Materials* **2019,** *29*, 1808375.

272. Fang, G., Zhou, J., Pan, A., Liang, S., Recent Advances in Aqueous Zinc-Ion Batteries *ACS Energy Lett.* **2018,** *3*, 2480-2501.

273. Huang, J., Poyraz, A. S., Lee, S.-Y., Wu, L., Zhu, Y., Marschilok, A. C., Takeuchi, K. J., Takeuchi, E. S., Silver-Containing α-MnO2 Nanorods: Electrochemistry in Na-Based Battery Systems. *ACS Appl Mater Interfaces* **2017,** *9* (5), 4333.

274. Sun, W., Wang, F., Hou, S., Yang, C., Fan, X., Ma, Z., Gao, T., Han, F., Hu, R., Zhu, M., Wang, C., Zn/MnO2 Battery Chemistry With H+ and Zn2+ Coinsertion. *J. Am. Chem. Soc.* **2017,** *139*, 9775.

275. Li, Y., Wang, S., Salvador, J. R., Wu, J., Liu, B., Yang, W., Yang, J., Zhang, W., Liu, J., Yang, J., Reaction Mechanisms for Long-Life Rechargeable Zn/MnO2 Batteries. *Chem. Mater.* **2019,** *31* (6), 2036-2047.

276. Kirshenbaum, K., Bock, D. C., Lee, C.-Y., Zhong, Z., Takeuchi, K. J., Marschilok, A. C., Takeuchi, E. S., In situ visualization of Li/Ag2VP2O8 batteries revealing rate-dependent discharge mechanism. *Science* **2015,** *347* (6218), 149-154.

277. Alfaruqi, M. H., Gim, J., Kim, S., Song, J., Pham, D. T., Jo, J., Xiu, Z., Mathew, V., Kim, J., A layered δ-MnO2 nanoflake cathode with high zinc-storage capacities for eco-friendly battery applications. *Electrochem. Commun.* **2015,** *60*, 121-125.

278. Huang, J., Poyraz, A. S., Lee, S.-Y., Wu, L., Zhu, Y., Marschilok, A. C., Takeuchi, K. J., Takeuchi, E. S., *ACS Appl Mater Interfaces* **2017,** *9*, 4333.

279. Zhang, N., Cheng, F., Liu, J., Wang, L., Long, X., Liu, X., Li, F., Chen, J., Rechargeable aqueous zinc-manganese dioxide batteries with high energy and power densities. *Nat. Commun.* **2017,** *8*, 405.

280. Kondrashev, Y. D., Zaslavskii, A. I., The structure of the modifications of manganese oxide. *Izvestiya Akademii Nauk SSSR* **1951,** (15), 179-186.

281. Housel, L. M., Wang, L., Abraham, A., Huang, J., Renderos, G. D., Quilty, C. D., Brady, A. B., Marschilok, A. C., Takeuchi, K. J., Takeuchi, E. S., Investigation of α-MnO2 Tunneled Structures as Model Cation Hosts for Energy Storage. *Acc. Chem. Res.* **2018,** *51* (3), 575-582.

282. Lee, B., Yoon, C. S., Lee, H. R., Chung, K. Y., Cho, B. W., Oh, S. H., Electrochemically-induced reversible transition from the tunneled to layered polymorphs of manganese dioxide. *Sci Rep* **2014,** *4*, 6066.

283. Takeuchi, K. J., Yau, S. Z., Subramanian, A., Marschilok, A. C., Takeuchi, E. S., The electrochemistry of silver hollandite nanorods, AgxMn8O16: enhancement of electrochemical battery performance via dimensional and compositional control. *J. Electrochem. Soc.* **2013,** *160* (5), A3090-A3094.

284. Brady, A. B., Huang, J., Durham, J. L., Smith, P. F., Bai, J., Takeuchi, E. S., Marschilok, A. C., Takeuchi, K. J., The Effect of Silver Ion Occupancy on Hollandite Lattice Structure. *MRS Adv.* **2018,** *3* (10), 547-552.

285. Takeuchi, E. S., Marschilok, A. C., Tanzil, K., Kozarsky, E. S., Zhu, S., Takeuchi, K. J., Electrochemical Reduction of Silver Vanadium Phosphorus Oxide, Ag2VO2PO4: The Formation of Electrically Conductive Metallic Silver Nanoparticles. *Chem. Mater.* **2009,** *21* (20), 4934-4939.

286. Xu, F., Wu, L., Meng, Q., Kaltak, M., Huang, J., Durham, J. L., Fenandez-Serra, M., Sun, L., Marschilok, A. C., Takeuchi, E. S., Takeuchi, K. J., Hybertsen, M., S., Zhu, Y., Visualization of lithium-ion transport and phase evolution within and between manganese oxide nanorods. *Nat. Commun.* **2017,** *8*, 15400.

287. Shan, L., Yang, Y., Zhang, W., Chen, H., Fang, G., Zhou, J., Liang, S., Observation of combination displacement/intercalation reaction in aqueous zinc-ion battery. *Enery Storage Mater.* **2019,** *18*, 10-14.

288. Shan, L., Zhou, J., Han, M., Fang, G., Cao, X., Wu, X., Liang, S. , Reversible Zn-driven reduction displacement reaction in aqueous zinc-ion battery. *J. Mater. Chem. A* **2019,** *7*, 7355-7359.

289. Liu, F., Chen, Z., Fang, G., Wang, Z., Cai, Y., Tang, B., Zhou, J., Liang, S., V2O5 Nanospheres with Mixed Vanadium Valences as High Electrochemically Active Aqueous Zinc-Ion Battery Cathode. *Nano-Micro Letters* **2019,** *11* (1), 25.

290. Takeuchi, K. J., Yau, S. Z., Menard, M. C., Marschilok, A. C., Takeuchi, E. S. , Synthetic control of composition and crystallite size of silver hollandite, Ag(x)Mn8O16: impact on electrochemistry. *ACS Appl Mater Interfaces* **2012,** *4* (10), 5547-5554.

291. Wang, L.; Wu, Q.; Abraham, A.; West, P. J.; Housel, L. M.; Singh, G.; Sadique, N.; Quilty, C. D.; Wu, D.; Takeuchi, E. S.; Marschilok, A. C.; Takeuchi, K. J., Silver-Containing α-MnO2 Nanorods: Electrochemistry in Rechargeable Aqueous Zn-MnO2 Batteries. *Journal of The Electrochemical Society* **2019,** *166* (15), A3575-A3584.

292. Simões, A., Battocchi, D., Tallman, D., Bierwagen, G., Assessment of the corrosion protection of aluminium substrates by a Mg-rich primer: EIS, SVET and SECM study. *Progress in Organic Coatings* **2008,** *63* (3), 260-266.

293. Williams, G., McMurray, H. N., Localized Corrosion of Magnesium in Chloride-Containing Electrolyte Studied by a Scanning Vibrating Electrode Technique. *J. Electrochem. Soc.* **2008,** *155* (7), C340-C349.

294. Deshpande, K. B., Effect of aluminium spacer on galvanic corrosion between magnesium and mild steel using numerical model and SVET experiments. *Corros. Sci.* **2012,** *62*, 184-191.

295. Jaffe, L. F., Nuccitelli, R., An Ultrasensitive Vibrating Probe for Measuring Steady Extracellular Currents. *J Cell Biol* **1974,** *63* (2), 614-628.

296. Chang, F. M., Jansen, M., Ag1.8Mn8O16: Square Planar Coordinated Ag⊕ Ions in the Channels of a Novel Hollandite Variant. *Angew. Chem. Int. Ed.* **1984,** *23* (11), 906-907.

297. Huang, J., Housel, L. M., Quilty, C. D., Brady, A. B., Smith, P. F., Abraham, A., Dunkin, M. R., Lutz, D. M., Zhang, B., Takeuchi, E. S., Marschilok, A. C., Takeuchi, K. J., Capacity Retention for (De)lithiation of Silver Containing α-MnO2: Impact of Structural Distortion and Transition Metal Dissolution. *J. Electrochem. Soc.* **2018,** *165* (11), A2849-A2858.

298. Chen, J., Tang, X., Liu, J., Zhan, E., Li, J., Huang, X., Shen, W., Synthesis and Characterization of Ag−Hollandite Nanofibers and Its Catalytic Application in Ethanol Oxidation. *Chem. Mater.* **2007,** *19* (17), 4292-4299.

299. Tanaka, Y., Tsuji, M., Tamaura, Y., ESCA and thermodynamic studies of alkali metal ion exchange reactions on an α-MnO2 phase with the tunnel structure. *Phys. Chem. Chem. Phys.* **2000,** *2*, 1473-1479.

300. Huang, J., Meng, Y., Labonte, A., Dobley, A., Suib, S. L., Large-Scale Synthesis of Silver Manganese Oxide Nanofibers and Their Oxygen Reduction Properties. *J. Phys. Chem. C* **2013,** *117* (48), 25352-25359.

301. Kirshenbaum, K. C., Bock, D. C., Zhong, Z., Marschilok, A. C., Takeuchi, K. J., Takeuchi, E. S., Electrochemical reduction of Ag2VP2O8 composite electrodes visualized via in situ energy dispersive X-ray diffraction (EDXRD): unexpected conductive additive effects. *J. Mater. Chem. A* **2015,** *3*, 180-18035.

302. Williams, G., Coleman, A. J., McMurray, H. N., Inhibition of Aluminium Alloy AA2024-T3 pitting corrosion by copper complexing compounds. *Electrochim. Acta* **2010,** *55* (20), 5947-5958.

303. Coelho, L. B., Mouanga, M., Druart, M. E., Recloux, I., Cossement, D., Oliver, M. G., A SVET study of the inhibitive effects of benzotriazole and cerium chloride solely and combined on an aluminium/copper galvanic coupling model. *Corros. Sci.* **2016,** *110*, 143-156.

304. Weberski, M. P.; McLauchlan, C. C., Synthesis, reactivity, and X-ray structural characterization of a vanadium(III) oxidation pre-catalyst, (CpPOEtCo)VCl2(DMF). *Inorganic Chemistry Communications* **2007,** *10* (8), 906-909.

305. McLauchlan, C. C.; Weberski, M. P.; Greiner, B. A., Synthesis, catalytic activity, phosphatase inhibition activity, and X-ray structural characterization of vanadium scorpionate complexes, (Tpms)VCl2(DMF) and (Tpms)VOCl(DMF). *Inorganica Chimica Acta* **2009,** *362* (8), 2662-2666.

306. McLauchlan, C. C.; Peters, B. J.; Willsky, G. R.; Crans, D. C., Vanadium-phosphatase complexes: Phosphatase inhibitors favor the trigonal bipyramidal transition state geometries. *Coordination Chemistry Reviews* **2015,** *301*, 163-199.

307. Tracey, A. S.; Willsky, G. R.; Takeuchi, E. S., *Vanadium: Chemistry, Biochemistry, Pharmacology and Practical Applications*. CRC Press: Boca Raton, Florida, USA, 2007.

308. Doucette, K. A.; Hassell, K. N.; Crans, D. C., Selective speciation improves efficacy and lowers toxicity of platinum anticancer and vanadium antidiabetic drugs. *Journal of Inorganic Biochemistry* **2016,** *165*, 56-70.

309. Krzystek, J.; Ozarowski, A.; Telser, J.; Crans, D. C., High-frequency and -field electron paramagnetic resonance of vanadium(IV, III, and II) complexes. *Coordination Chemistry Reviews* **2015,** *301*, 123-133.

310. Crans, D. C.; Tarlton, M. L.; McLauchlan, C. C., Trigonal Bipyramidal or Square Pyramidal Coordination Geometry? Investigating the Most Potent Geometry for Vanadium Phosphatase Inhibitors. *European Journal of Inorganic Chemistry* **2014,** (27), 4450-4468.

311. Morin, F. J., Oxides that show a metal-to-insulator transition at the Neel temperature. *Phys. Rev. Lett.* **1959,** *3*, 34-6.

312. Goodenough, J. B., The two components of the crystallographic transition in VO2. *Journal of Solid State Chemistry* **1971,** *3* (4), 490-500.

313. Cao, J.; Fan, W.; Chen, K.; Tamura, N.; Kunz, M.; Eyert, V.; Wu, J., Constant threshold resistivity in the metal-insulator transition ofVO2. *Physical Review B* **2010,** *82* (24).

314. Yang, Z.; Ko, C.; Ramanathan, S., Metal-insulator transition characteristics of VO2 thin films grown on Ge(100) single crystals. *Journal of Applied Physics* **2010,** *108* (7), 073708.

315. Cao, J.; Ertekin, E.; Srinivasan, V.; Fan, W.; Huang, S.; Zheng, H.; Yim, J. W. L.; Khanal, D. R.; Ogletree, D. F.; Grossman, J. C.; Wu, J., Strain engineering and one-dimensional organization of metal-insulator domains in single-crystal vanadium dioxide beams. *Nat Nano* **2009,** *4* (11), 732-737.

316. Yang, M.; Yang, Y.; Bin, H.; Wang, L.; Hu, K.; Dong, Y.; Xu, H.; Huang, H.; Zhao, J.; Chen, H.; Song, L.; Ju, H.; Zhu, J.; Bao, J.; Li, X.; Gu, Y.; Yang, T.; Gao, X.; Luo, Z.; Gao, C., Suppression of Structural Phase Transition in VO2 by Epitaxial Strain in Vicinity of Metal-insulator Transition. *Scientific Reports* **2016,** *6*, 23119.

317. Stefanovich, G.; Pergament, A.; Stefanovich, D., Electrical switching and Mott transition in VO 2. *Journal of Physics: Condensed Matter* **2000,** *12* (41), 8837.

318. Cavalleri, A.; Tóth, C.; Siders, C. W.; Squier, J. A.; Ráksi, F.; Forget, P.; Kieffer, J. C., Femtosecond Structural Dynamics in VO2 during an Ultrafast Solid-Solid Phase Transition. *Physical Review Letters* **2001,** *87* (23), 237401.

319. Whittaker, L.; Patridge, C. J.; Banerjee, S., Microscopic and Nanoscale Perspective of the Metal−Insulator Phase Transitions of VO2: Some New Twists to an Old Tale. *The Journal of Physical Chemistry Letters* **2011,** *2* (7), 745-758.

320. Gao, Y.; Luo, H.; Zhang, Z.; Kang, L.; Chen, Z.; Du, J.; Kanehira, M.; Cao, C., Nanoceramic VO2 thermochromic smart glass: A review on progress in solution processing. *Nano Energy* **2012,** *1* (2), 221-246.

321. Stone, K. H.; Schelhas, L. T.; Garten, L. M.; Shyam, B.; Mehta, A.; Ndione, P. F.; Ginley, D. S.; Toney, M. F., Influence of amorphous structure on polymorphism in vanadia. *APL Materials* **2016,** *4* (7), 076103.

322. Asayesh-Ardakani, H.; Nie, A.; Marley, P. M.; Zhu, Y.; Phillips, P. J.; Singh, S.; Mashayek, F.; Sambandamurthy, G.; Low, K.-b.; Klie, R. F.; Banerjee, S.; Odegard, G. M.; Shahbazian-Yassar, R., Atomic Origins of Monoclinic-Tetragonal (Rutile) Phase Transition in Doped VO2 Nanowires. *Nano Letters* **2015,** *15* (11), 7179-7188.

323. Asayesh-Ardakani, H.; Nie, A.; Zhu, Y.; Phillips, P. J.; Klie, R. F.; Banerjee, S.; Odegard, G. M.; Shahbazian-Yassar, R., Atomic Resolution Studies of W Dopants Effect on the Phase Transformation of VO2. *Microscopy and Microanalysis* **2016,** *22* (S3), 884-885.

324. Wu, Y.; Fan, L.; Liu, Q.; Chen, S.; Huang, W.; Chen, F.; Liao, G.; Zou, C.; Wu, Z., Decoupling the Lattice Distortion and Charge Doping Effects on the Phase Transition Behavior of VO2 by Titanium (Ti4+) Doping. *Scientific Reports* **2015,** *5*, 9328.

325. Fan, L. L.; Chen, S.; Luo, Z. L.; Liu, Q. H.; Wu, Y. F.; Song, L.; Ji, D. X.; Wang, P.; Chu, W. S.; Gao, C.; Zou, C. W.; Wu, Z. Y., Strain dynamics of ultrathin VO(2) film grown on TiO(2) (001) and the associated phase transition modulation. *Nano Lett* **2014,** *14* (7), 4036-43.

326. Muraoka, Y.; Hiroi, Z., Metal–insulator transition of VO2 thin films grown on TiO2 (001) and (110) substrates. *Applied Physics Letters* **2002,** *80* (4), 583-585.

327. Yoon, J.; Kim, H.; Chen, X.; Tamura, N.; Mun, B. S.; Park, C.; Ju, H., Controlling the Temperature and Speed of the Phase Transition of VO2 Microcrystals. *ACS Appl Mater Interfaces* **2016,** *8* (3), 2280-6.

328. Whittaker, L.; Jaye, C.; Fu, Z.; Fischer, D. A.; Banerjee, S., Depressed Phase Transition in Solution-Grown VO2 Nanostructures. *Journal of the American Chemical Society* **2009,** *131* (25), 8884-8894.

329. Morrison, V. R.; Chatelain, R. P.; Tiwari, K. L.; Hendaoui, A.; Bruhács, A.; Chaker, M.; Siwick, B. J., A photoinduced metal-like phase of monoclinic VO₂ revealed by ultrafast electron diffraction. *Science* **2014,** *346* (6208), 445-448.

330. Cavalleri, A.; Rini, M.; Chong, H. H.; Fourmaux, S.; Glover, T. E.; Heimann, P. A.; Kieffer, J. C.; Schoenlein, R. W., Band-selective measurements of electron dynamics in VO2 using femtosecond near-edge x-ray absorption. *Phys Rev Lett* **2005,** *95* (6), 067405.

331. Qazilbash, M. M.; Brehm, M.; Chae, B.-G.; Ho, P.-C.; Andreev, G. O.; Kim, B.-J.; Yun, S. J.; Balatsky, A. V.; Maple, M. B.; Keilmann, F.; Kim, H.-T.; Basov, D. N., Mott Transition in VO2 Revealed by Infrared Spectroscopy and Nano-Imaging. *Science* **2007,** *318* (5857), 1750-1753.

332. Donges, S. A.; Khatib, O.; O'Callahan, B. T.; Atkin, J. M.; Park, J. H.; Cobden, D.; Raschke, M. B., Ultrafast Nanoimaging of the Photoinduced Phase Transition Dynamics in VO2. *Nano Lett* **2016,** *16* (5), 3029-35.

333. Marschilok, A. C.; Schaffer, C. P.; Takeuchi, K. J.; Takeuchi, E. S., Carbon nanotube–metal oxide composite electrodes for secondary lithium-based batteries. *Journal of Composite Materials* **2012,** *47* (1), 41-49.

334. Rahman, M. M.; Wang, J.-Z.; Idris, N. H.; Chen, Z.; Liu, H., Enhanced lithium storage in a VO2(B)-multiwall carbon nanotube microsheet composite prepared via an in situ hydrothermal process. *Electrochimica Acta* **2010,** *56* (2), 693-699.

335. Ganganagappa, N.; Siddaramanna, A., One step synthesis of monoclinic VO2 (B) bundles of nanorods: Cathode for Li ion battery. *Materials Characterization* **2012,** *68*, 58-62.

336. Popuri, S. R.; Artemenko, A.; Decourt, R.; Josse, M.; Chung, U. C.; Michau, D.; Maglione, M.; Villesuzanne, A.; Pollet, M., Structurally Restricted Phase Transitions in VO2(B) and Their Impact on Transport Properties. *The Journal of Physical Chemistry C* **2015,** *119* (44), 25085-25092.

337. Xiao, X.; Li, S.; Wei, H.; Sun, D.; Wu, Y.; Jin, G.; Wang, F.; Zou, Y., Synthesis and characterization of VO2(B)/graphene nanocomposite for supercapacitors. *Journal of Materials Science: Materials in Electronics* **2015,** *26* (6), 4226-4233.

338. Tsang, C.; Manthiram, A., Synthesis of nanocrystalline VO2 and its electrochemical behavior in lithium batteries. *J. Electrochem. Soc.* **1997,** *144* (2), 520-524.

339. Muñoz-Rojas, D.; Baudrin, E., Synthesis and electroactivity of hydrated and monoclinic rutile-type nanosized VO2. *Solid State Ionics* **2007,** *178* (21–22), 1268-1273.

340. Ni, J.; Jiang, W.; Yu, K.; Sun, F.; Zhu, Z., Electrochemical performance of B and M phases VO2 nanoflowers. *Cryst. Res. Technol.* **2011,** *46* (5), 507-510.

341. Song, H. J.; Park, S.; Lee, C. W.; Hong, S.-H.; Choi, M.; Kim, J.-C.; Kim, D.-W.; Kim, B.-K., Enhanced Lithium Storage in Reduced Graphene Oxide-supported M-phase Vanadium(IV) Dioxide Nanoparticles. *Sci Rep* **2016,** *6*, 30202.

342. Kulish, V. V.; Koch, D.; Manzhos, S., Ab initio study of Li, Mg and Al insertion into rutile VO2: fast diffusion and enhanced voltages for multivalent batteries. *Phys. Chem. Chem. Phys.* **2017,** *19* (33), 22538-22545.

343. Housel, L. M.; Quilty, C. D.; Abraham, A.; Tang, C. R.; McCarthy, A. H.; Renderos, G. D.; Liu, P.; Takeuchi, E. S.; Marschilok, A. C.; Takeuchi, K. J., Investigation of Conductivity and Ionic Transport of VO2(M) and VO2(R) via Electrochemical Study. *Chemistry of Materials* **2018,** *30* (21), 7535-7544.

344. Li, G.; Chao, K.; Peng, H.; Chen, K.; Zhang, Z., Low-Valent Vanadium Oxide Nanostructures with Controlled Crystal Structures and Morphologies. *Inorganic Chemistry* **2007,** *46* (14), 5787-5790.

345. Andersson, G., Vanadium oxides. II. The crystal structure of vanadium dioxide. *Acta Chem. Scand.* **1956,** *10*, 623-8.

346. Galy, J.; Miehe, G., Ab initio structures of (M2) and (M3) VO2 high pressure phases. *Solid State Sciences* **1999,** *1* (6), 433-448.

347. Hoekstra, H. R.; Siegel, S.; Gallagher, F. X., Reaction of Platinum Dioxide with Some Metal Oxides. In *Platinum Group Metals and Compounds*, AMERICAN CHEMICAL SOCIETY: 1971; Vol. 98, pp 39-53.

348. Rogers, K. D., An X-ray diffraction study of semiconductor and metallic vanadium dioxide. *Powder Diffraction* **1993,** *8* (4), 240-244.

349. Kim, B.-J.; Lee, Y. W.; Chae, B.-G.; Yun, S. J.; Oh, S.-Y.; Kim, H.-T.; Lim, Y.-S., Temperature dependence of the first-order metal-insulator transition in VO2 and programmable critical temperature sensor. *Appl. Phys. Lett.* **2007,** *90* (2), 023515/1-023515/3.

350. Born, M., Oppenheimer, J. R., Quantum Theory of the Molecules. *Annalen der Physik* **1927,** *84*, 457-484.

351. Hafner, J., Ab-Initio Simulations of Materials Using VASP: Density-Functional Theory and Beyond. *J. Comput. Chem.* **2008,** *29*, 2044-2078.

352. Blöchl, P. E., Projector Augmented-wave Method. *Phys. Rev. B: Condens. Matter Mater. Phys.* **1994,** (50), 17953-17979.

353. Kohn, W., Sham., L. J., Self-consistent equations including exchange and correlation effects. *Phys. Rev.* **1965,** *140*, A1133-1138.

354. Langreth, D. C., Perdew, J. P., Theory of nonuniform electronic systems I. Analysis of gradient approximation and a generalization that works. *Phys. Rev. B: Condens. Matter Mater. Phys.* **1980,** *21*, 5469-5493.

355. Perdew, J. P., Chevary, J. A., Vosko, S. H., Jackson, K. A., Pederson, M. R., SIngh, D. J., Fiolhais, C., Atoms, molecules, solids, and surfaces: Applications of the generatlized gradient approximation for exchange and correlation. *Phys. Rev. B. Condens. Matter* **1992,** *46* (11), 6671-6687.

356. Argaman, N., Makov, G., Density Functional Theory: An Introduction *Am. J. Phys.* **2000,** *68*, 69-79.

357. Sugantha, M., Ramakrishnan, P. A., Hermann, A. M., Warmsingh, C. P., Ginley, D. S., Nanostructred MnO2 for Li batteries. *International Journal of Hydrogen Energy* **2003,** *28*, 597-600.

358. Tumurugoti, P., Betal, S., Sundaram, S. K., Hollandites' crystal chemistry, properties, and processing: a review. *International Materials Reviews* **2020,** *DOI: 10.1080/09506608.2020.1743592*.

359. Joseph, J., Nerkar, J., Tang, C., Du, A., O'Mullane, A. P., Ostrikov, K., Reversible Intercalation of Multivalent Al3+ Ions into Potassium-Rich Cryptomelane Nanowires for Aqueous Rechargeable Al-Ion Batteries. *ChemSusChem* **2019,** *12*, 3753-3760.

360. Cui, J., Wu, X., Yang, S., Li, C., Tang, F., Chen, J. Chen, Y., Xiang, Y., Wu, X., He, Z., Cryptomelane-type KMn8O16 as potential cathode material - for aqueous zinc ion battery. *Frontiers in Chemistry* **2018,** *6*, DOI:10.3389/fchem.2018.00352.

361. Rasul, S., Suzuki, S., Yamaguchi, S., Miyayama, M., Synthesis and electrochemical behavior of hollandite MnO2/acetylene black composite cathode for secondary Mg-ion batteries. *Solid State Ionics* **2012,** *225*, 542-546.

362. Kaltak, M., Fernańdez-Serra, M., Hybertsen, M. S., Charge Localization and Ordering in A2Mn8O16 Hollandite Group Oxides: Impact of Density Functional Theory Approaches. **2017,** *1*, 075401.

363. Kijima, N., Ikeda, T., Oikawa, K., Izumi, F., Yoshimura, Y., Crystal structure of an open-tunnel oxide α-MnO2 analyzed by Rietveld refinements and MEM-based pattern fitting. *J. Solid State Chem.* **2004,** *177*, 1258.

364. Yang, Z. T., L.; Ren, Y.; Chan, M. K. Y.; Lin, C.; Okasinski, J.; Thackeray, M. M., In Situ High-Energy Synchrotron X- ray Diffraction Studies and First Principles Modeling of α-MnO2 Electrodes in Li−O2 and Li-Ion Coin Cells. *J. Mater. Chem. A* **2015,** *3*, 7389-7398.

365. Yuan, Y. N., A.; Odegard, G. M.; Xu, R.; Zhou, D.; Santhanagopalan, S.; He, K.; Asayesh-Ardakani, H.; Meng, D. D.; Klie, R. F.; et al., Asynchronous Crystal Cell Expansion during Lithiation of K+-Stabilized α-MnO2. . *Nano Lett.* **2015,** *15*, 2998-3007.

366. Yuan, Y., Wood, S. M., He, K., Yao, W., Tompsett, D., Lu, J., Nie, A., Islam, M. S., Shahbazian-Yassar, R., Atomistic Insights into the Oriented Attachment of Tunnel-Based Oxide Nanostructures. *ACS Nano* **2016,** *10*, 539-548.

367. Julien, C. M., A., Nanostructured MnO2 as Electrode Materials for Energy Storage. *Nanomaterials* **2017,** *7*, 396.

368. Huang, J. H., L. M.; Quilty, C. D.; Brady, A. B.; Smith, P. F.; Abraham, A.; Dunkin, M. R.; Lutz, D. M.; Zhang, B.; Takeuchi, E. S.; et al. , Capacity Retention for (De)lithiation of Silver Containing α- MnO2: Impact of Structural Distortion and Transition Metal Dissolution. *J. Electrochem. Soc.* **2018,** *165* (165), A2849-A2858.

369. Perdew, J. P., Burke, K., Erzenhof, M., Generalized Gradient Approximation Made Simple. *Phys. Rev. Lett.* **1996,** *77* (18), 3865-3868.

370. Klimeš, J., Bowler, D. R., Michaelides, A., Chemical accuracy for the van der waals density functional. *J. Phys.: Condens. Matt.* **2010,** *22*, 02201.

371. Anisimov, V. I., Zaanen, J., Andersen, O. K., Band theory and Mott insulators: Hubbard U instead of Stoner I. *Phys. Rev. B* **1991,** *44*, 943.

372. Anisimov, V. I., Aryasetiawan, F., Lichtenstein, A. I., First-principles calculations of the electronic structure and spectra of strongly correlated systems: The LDA + U method. *J. Phys.: Condens. Matt.* **1997,** *9*, 767.

373. Tompsett, D. A., Islam, M. S., Electrochemistry of Hollandite α-MnO2: Li-ion and Na-ion Insertion and Li2O Incorporation. *Chem. Mater.* **2013,** *25*, 2515-2526.

374. Ling, C., Mizuno, F., Capture Lithium in αMnO2: Insights from First Principles. *Chem. Mater.* **2012,** *24*, 3943-3951.

375. Cockayne, E., Li, L., First-Principles DFT + U Studies of the Atomic, Electronic, and Magnetic Structure of α-MnO2 (Cryptomelane). *Chem. Phys. Lett.* **2012,** *544*, 53-58.

376. Trahey, L., Karan, N., Chan, M. K. Y., Lu, J., Ren, Y., Greeley, J., Balasubramanian, M., Burrell, A. K., Curtiss, L. A., Thackeray, M. M., Synthesis, Characterization, and Structural Modeling of High-Capacity, Dual Functioning MnO2 Electrode/Electrocatalysts for Li-O2 Cells. *Adv. Energy Mater.* **2013,** *3*, 75-84.

377. Brady, A. B.; Tallman, K. R.; Takeuchi, E. S.; Marschilok, A. C.; Takeuchi, K. J.; Liu, P., Transition Metal Substitution of Hollandite α-MnO2: Enhanced Potential and Structural Stability on Lithiation from First-Principles Calculation. *The Journal of Physical Chemistry C* **2019,** *123* (41), 25042-25051.

378. Guo, H.; Marschilok, A. C.; Takeuchi, K. J.; Takeuchi, E. S.; Liu, P., Essential Role of Spinel ZnFe2O4 Surfaces during Lithiation. *ACS Appl Mater Interfaces* **2018,** *10* (41), 35623-35630.

379. Guo, H., Marschilok, A. C., Takeuchi, K. J., Takeuchi, E. S., Liu, P., Essential Role of Spinel ZnFe2O4 Surfaces during Lithiation *ACS Appl. Mater. Interfaces* **2018,** *10*, 35623-35630.

380. Zhang, Y. P., C. J.; Brady, A. B.; Guo, H.; Smith, P. F.; Liu, P.; Marschilok, A. C.; Takeuchi, K. J.; Takeuchi, E. S., Probing the Li Insertion Mechanism of ZnFe2O4 in Li-Ion Batteries: A Combined X-Ray Diffraction, Extended X-Ray Absorption Fine Structure, and Density Functional Theory Study. . *Chem. Mater.* **2017,** *29*, 4282− 4292.

381. Guo, H. Z., Y.; Marschilok, A. C.; Takeuchi, K. J.; Takeuchi, E. S.; Liu, P. , A First Principles Study of Spinel ZnFe2O4 for Electrode Materials in Lithium-ion Batteries. . *Phys. Chem. Chem. Phys.* **2017,** *19*, 26322−26329.

382. Sharma, Y. S., N.; Rao, G. V. S.; Chowdari, B. V. R. , Li- storage and Cyclability of Urea Combustion Derived ZnFe2O4 as Anode for Li-ion Batteries. . *Electrochim. Acta* **2008,** *53*, 2380−2385.

383. Zhong, X.-B. J., B.; Yang, Z.-Z.; Wang, C.; Wang, H.-Y. , Facile Shape Design and Fabrication of ZnFe2O4 as an Anode Material for Li-ion Batteries. *RSC Adv.* **2014,** *4*, 55173−55178.

384. Bresser, D. P., E.; Kloepsch, R.; Krueger, S.; Fiedler, M.; Schmitz, R.; Baither, D.; Winter, M.; Passerini, S., Carbon Coated ZnFe2O4 Nanoparticles for Advanced Lithium-Ion Anodes. . *Adv. Energy Mater.* **2013,** *3*, 513−523.

385. Rai, A. K. K., S.; Gim, J.; Alfaruqi, M. H.; Mathew, V.; Kim, J. , Electrochemical Lithium Storage of a ZnFe2O4/graphene Nano- composite as an Anode Material for Rechargeable Lithium Ion Batteries. *RSC Adv.* **2014,** *4*, 47087−47095.

386. Song, H. Z., L.; Li, Y.; Lou, Z.; Xiao, M.; Ye, Z. , Preparation of ZnFe2O4 Nanostructures and Highly Efficient Visible-light-driven Hydrogen Generation with the Assistance of Nanoheterostructures *J. Mater. Chem. A* **2015,** *3*, 8353−8360.

387. Lv, H. M., L.; Zeng, P.; Ke, D.; Peng, T. , Synthesis of Floriated ZnFe2O4 with Porous Nanorod Structures and its Photocatalytic Hydrogen Production Under Visible Light. *J. Mater. Chem.* **2010,** *20*, 3665-3672.

388. Qian, G.-X. M., R. M.; Chadi, D. J. , First-principles study of the atomic reconstructions and energies of Ga- and As-stabilized GaAs(100) surfaces 38. *Phys. Rev. B: Condens. Matter Mater. Phys.* **1988,** *38*, 7649−7663.

389. Kim, S. A., M.; Wolverton, C. , Surface Phase Diagram and Stability of (001) and (111) LiMn2O4 Spinel Oxides. *Phys. Rev. B: Condens. Matter Mater. Phys.* **2015,** *92*, 115411.

390. Warburton, R. E. I., H.; Curtiss, L. A.; Greeley, J. , Thermodynamic Stability of Low- and High-Index Spinel LiMn2O4 Surface Terminations. *ACS Appl. Mater. Interfaces* **2016,** *8*, 11108-11121.

391. Pentcheva, R. W., F.; Meyerheim, H. L.; Moritz, W.; Jedrecy, N.; Scheffler, M. , Jahn-Teller Stabilization of a "Polar" Metal Oxide Surface: Fe3O4(001). *Phys. Rev. Lett.* **2005,** *94*, 126101.

392. Chen, Z.; Li, G.; Zheng, H.; Shu, X.; Zou, J.; Peng, P., Mechanism of surface effect and selective catalytic performance of MnO 2 nanorod: DFT+U study. *Applied Surface Science* **2017,** *420*, 205-213.

393. Tompsett, D. A.; Parker, S. C.; Islam, M. S., Surface properties of α-MnO2: relevance to catalytic and supercapacitor behaviour. *J. Mater. Chem. A* **2014,** *2* (37), 15509-15518.

394. Kresse, G., Furthmüller, J., Efficient iterative schemes for ab initio total-energy calculations using a plane-wave basis set. *Phys. Rev. B: Condens. Matter Mater. Phys.* **1996,** *54*, 11169-11186.

395. Morgan, B. J., Watson, G. W., A Density Functional Theory + U Study of Oxygen Vacancy Formation at the (110), (100), (101), and (001) Surfaces of Rutile TiO2. *J. Phys. Chem. C* **2009,** *113* (17), 7322-7328.

396. Madsen, G. K. H., Novak, P., Charge order in magnetite. An LDA+U study. *Europhys. Lett.* **2005,** *69* (5), 777.

397. Schwarz, K., Blaha, P., Solid state calculations using WIEN2k. *Comput. Mater. Sci* **2003,** *28* (2), 259-273.

398. Franchini, C., Podloucky, R., Pair, J., Marsman, M., Kresse, G., Ground-state properties of multivalent manganese oxides: Density functional and hybrid density functional calculations. *Phys. Rev. B: Condens. Matter Mater. Phys.* **2007,** *75* (19), 195128.

399. Zhang, X., Sun, X., Zhang, H., Ma, Y., Microwave-assisted reflux rapid synthesis of MnO2 nanostructures and their application in supercapacitors. *Electrochim. Acta* **2013,** *87* (1), 637-644.

400. Guo, H.; Marschilok, A. C.; Takeuchi, K. J.; Takeuchi, E. S.; Liu, P., Rationalization of Diversity in Spinel MgFe2O4 Surfaces. *Advanced Materials Interfaces* **2019,** *6* (22).

401. Kresse, G. F. l., J. , Efficiency of ab-initio total energy calculations for metals and semiconductors using a plane-wave basis set. *Comput. Mater. Sci.* **1996,** *6*, 15-50.

402. Smith, P. F. W., L.; Bock, D. C.; Brady, A. B.; Lutz, D. M.; Yang, S.; Hu, X.; Wu, L.; Zhu, Y.; Marschilok, A. C.; Takeuchi, E. S.; Takeuchi, K. J., Vanadium-Substituted Tunnel Structured Silver Hollandite (Ag1.2VxMn8-xO16): Impact on Morphology and Electrochemistry. *Revision under review* **2019**.